Solar wind turbulence studies from 0.3 to 1 AU : HELIOS and WIND observations

Vamsee Krishna Jagarlamudi

Centre Val de Loire UNIVERSITÉ
Spirit of the Loire Valley

UNIVERSITE D'ORLEANS

ÉCOLE DOCTORALE : ÉNERGIE, MATÉRIAUX, SCIENCES DE LA TERRE ET DE L'UNIVERS

Laboratoire de Physique et Chimie de l'Environnement et l'Espace (LPC2E)

Thèse présentée par :

Vamsee Krishna JAGARLAMUDI

soutenue le : **27 septembre 2019**

pour obtenir le grade de : **Docteur de l'Université d'Orléans**

Discipline/ Spécialité : **Sciences de l'Univers**

Turbulence du vent solaire de 0.3 à 1 UA : Observations de HELIOS et de WIND

Thèse dirigée par :

Dudok de Wit Thierry	Professeur à l'Université d'Orléans, LPC2E/OSUC, Orléans
Maksimovic Milan	DR CNRS, LESIA/Observatoire de Paris, Paris

RAPPORTEURS :

Robert Wicks	Professeur associé à l'University College London, UCL, London
Oleksiy Agapitov	Professeur associé à l'University of California, SSL, Berkeley

---

JURY :

Oleksiy AGAPITOV	Professeur associé à l'University of California, SSL, Berkeley
Olga ALEXANDROVA	CR CNRS, LESIA/Observatoire de Paris, Paris
Thierry DUDOK DE WIT	Professeur à l'Université d'Orléans, LPC2E/OSUC, Orléans
Vladimir KRASNOSELSKIKH	DR CNRS, LPC2E/OSUC, Orléans - Président du jury -
Milan MAKSIMOVIĆ	DR CNRS, LESIA/Observatoire de Paris, Paris
Robert WICKS	Professeur associé à l'University College London, UCL, London

"We shall not cease from exploration, and the end of all our exploring will be to arrive where we started and know the place for the first time."

T. S. Eliot

Abstract

by Vamsee KRISHNA JAGARLAMUDI

One of the key issues in solar wind studies is the understanding of the evolution of turbulence, both across spatial scales, and radially, when moving away from the Sun. We use magnetic field observations from the *WIND* and *HELIOS* missions to address this issue.

First, using long records from *WIND* we identify the initiation of the non-linear turbulent cascade in the slow solar wind. From the quasi-invariance of the ratio between non-linear time and Alfvén time we conclude that the similar evolution of turbulence in fast and slow winds is primarily governed by the constant $\frac{\langle B \rangle}{\delta B}$ ratio.

Second, we show how one single parametric expression can describe the power spectral density at kinetic scales at all positions in the inner heliosphere (between 0.3 and 1 AU). We also reveal the presence of narrow-band whistler waves in the inner heliosphere and using the halo anisotropy values show how the slow wind provides the proper conditions for the prevalence of whistlers.

Finally, we reveal how non-stationarity is inherent to solar wind turbulence in the inertial range, which questions the use of autocorrelation functions to estimate characteristic scales.

Résumé

Un des enjeux majeurs dans l'étude du vent solaire est la compréhension fine de l'évolution de la turbulence entre échelles spatiales d'une part mais aussi radialement, en fonction de la distance du Soleil. Nous abordons ces questions à l'aide des observations de champ magnétique effectuées par les missions *WIND* et *HELIOS*.

D'abord, à partir de longues séries temporelles de *WIND* nous identifions le début de la cascade non linéaire dans le vent solaire lent. De la quasi-invariance du rapport entre le temps non linéaire et le temps d'Alfvén, nous déduisons que l'évolution similaire de la turbulence observée dans les vents lents et rapides peut s'expliquer par la constance du rapport $\frac{\langle B \rangle}{\delta B}$.

Ensuite, nous montrons comment une seule expression paramétrique permet de décrire la densité spectrale de puissance aux échelles cinétiques en tout lieu de l'héliosphère interne (entre 0.3 et 1 UA). Nous révélons également la présence dans l'héliosphère interne d'ondes de sifflement quasi-monochromatiques et montrons comment le vent lent offre les conditions propices pour la présence préférentielle de ces ondes via le mécanisme d'anisotropie du halo.

Enfin, nous montrons comment la non-stationnarité est inhérente à la turbulence du vent solaire dans le régime inertiel. Ceci remet en question l'utilisation fréquente de la fonction d'autocorrélation comme outil pour estimer les échelles caractéristiques.

Acknowledgements

This whole journey of the PhD thesis has been a wonderful ride. I have learned a lot, gained invaluable experience and knowledge. This journey would not have been possible without the support and guidance that I have received from many people throughout these 3 years.

First of all, I would like to thank my supervisor, Prof. Thierry Dudok de Wit, for his invaluable guidance, support, and constant encouragement, throughout these three years. He was always keen to help me, either it was academic or a personal issue right from the beginning of the thesis to date. He has been the best mentor I could have asked for. He had shown me how critical one had to be with his own work for the research to head in the right direction.

I would like to extend my sincere thanks to my other supervisor, Dr. Milan Maksimovic, for the support, guidance, and encouragement he has offered me during my thesis. He was always clear in pointing out my mistakes and also in appreciating my achievements, he has always tried to make me a better researcher.

I would also like to thank my co-supervisors, Dr. Olga Alexandrova and Dr. Vladimir Krasnoselskikh for their valuable suggestions and insights for my work. They have always tried to clear my queries. I feel extremely lucky to have such a wonderful group of people as my supervisors and co-supervisors.

I gratefully acknowledge the funding I have received from CNES and the Région Centre-Val de Loire for my PhD.

I convey my thanks to the colleagues and staff at LESIA and LPC2E who have helped me with the french language and the numerous administrative issues. I am thankful to my friends Andrea, Anna, Laura, Luca, Matthieu, Mélody, Minna, Nini, Nicolas, Rajkumar and other good friends for being a part of my journey and making this 3 year ride a joyous and a memorable one.

Last but most importantly, I would like to thank my parents who have always encouraged me to pursue whatever I have dreamt of, without their encouragement and support I would not have been here.

I would like to dedicate this thesis to my parents and my late grandmother who has always loved me with her whole heart and who would have been the happiest person with my success.

Contents

Abstract iii

Acknowledgements v

1 Introduction 1
- 1.1 The solar wind . . . 1
  - 1.1.1 Magnetic field . . . 3
  - 1.1.2 Turbulence in the solar wind magnetic field . . . 4
  - 1.1.3 Solar wind electrons . . . 5
  - 1.1.4 Solar wind protons . . . 7
- 1.2 Outline of this thesis . . . 8
- 1.3 Résumé en français: Introduction . . . 12

2 The HELIOS mission 13
- 2.1 Introduction . . . 13
- 2.2 The HELIOS Mission . . . 13
  - 2.2.1 Objective . . . 13
- 2.3 Coordinate systems . . . 14
- 2.4 Magnetometers . . . 16
  - 2.4.1 Fluxgate magnetometer onboard HELIOS . . . 16
  - 2.4.2 Search coil magnetometer onboard HELIOS . . . 18
- 2.5 Résumé en français: La mission HELIOS . . . 23

3 Turbulence from the injection scale to the dissipation scale 25
- 3.1 Introduction . . . 25
- 3.2 Data . . . 27
- 3.3 f^{-1} in the slow wind . . . 28
  - 3.3.1 Slow wind at 1 AU . . . 29
  - 3.3.2 Slow wind in the inner-heliosphere . . . 37
  - 3.3.3 Non-linear time estimations and the connection between the spectral break in the fast and slow solar wind . . . 38
- 3.4 Kinetic scale turbulence in the inner heliosphere . . . 45
- 3.5 Evolution of turbulence from the f^{-1} range to the dissipation range in the inner heliosphere . . . 55
- 3.6 Conclusion . . . 57
- 3.7 Résumé en français: La turbulence des échelles d'injection aux échelles dissipatives . . . 58

4 Non-stationarity in solar wind 61
- 4.1 Introduction . . . 61
- 4.2 Data . . . 63
- 4.3 Results . . . 64
  - 4.3.1 Autocorrelation function (ACF) Analysis . . . 64

4.3.2 Relating the ACF observations to the power spectral density . . 68
4.3.3 Synthetic data analysis 70
4.4 Discussion 72
4.5 Conclusion 73
4.6 Résumé en français: Non-stationnarité dans le vent solaire 74

5 Whistler waves in the inner heliosphere **77**
5.1 Introduction 77
5.2 Data used for the whistler wave analysis 81
5.3 Whistler wave identification and their confirmation 85
5.3.1 Identification 85
5.3.2 Method of conformation of the whistler waves 86
5.4 Whistler wave properties 93
5.4.1 Velocity of the observed whistler waves 94
5.4.2 Radial distribution of the observed whistler waves 95
5.4.3 Thermal pressure of the observed whistler waves 97
5.4.4 Halo electron anisotropy ($\frac{T_{\perp h}}{T_{\parallel h}}$) values corresponding to the observed whistler waves 99
5.4.5 Amplitude of the fluctuation of the observed whistler waves . . 100
Summary of the important whistler properties 102
5.5 Discussions on the observed whistler properties in the inner heliosphere 104
5.5.1 Why are whistler waves predominantly observed in the slow solar wind but not in the fast wind ? 104
Is it related to generation mechanism ? 106
Reasons for the observed halo anisotropy trends 110
A feedback mechanism 111
5.6 Conclusion 115
5.7 Résumé en français: Ondes de type siffleur dans le vent solaire 116

6 Conclusion **117**
6.1 Questions answered 117
6.2 Unanswered questions and future projects 118
6.3 Résumé en français: Conclusion 120

References **123**

Chapter 1

Introduction

1.1 The solar wind

The solar wind is a stream of highly ionized gas that is originating from the Sun and fills the whole interplanetary space (Meyer-Vernet, 2012). This unsteady plasma stream primarily consists of protons and electrons, with alpha particles and heavier ions in smaller amounts. This plasma stream exists as a consequence of the supersonic expansion of the Sun's outer atmosphere, which is called the solar corona. On average, the Sun loses 10^9 kg/s of plasma. Although this may seem a large amount, it only represents a tiny fraction, 10^{-4} of the solar mass over a time period of 10^9 years.

Typical values of some of the main solar wind parameters near the equatorial plane and at 1 astronomical unit (AU) are shown in Figure 1.1. The solar wind is a highly dynamic medium that exhibits temporal variations on time scales ranging from years and beyond to microseconds and below. Likewise, the spatial structure of the solar wind is highly complex and is affected by different types of transients (shocks, coronal mass ejections, magnetic boundaries, discontinuities, ...) and different types of plasma waves. While some of these spatial structures such as coronal magnetic loops remain attached to the Sun, most are convected with the solar wind or are propagating through it.

The temporal variations and spatial structure of the solar wind have a direct impact on planetary environments, which are continuously buffeted by the varying solar wind flow (Spohn, Breuer, and Johnson, 2014). Indeed, variations in the solar wind parameters such as the magnetic field, density or velocity impact planetary magnetic fields in different ways. One typical manifestation is the generation of auroras on planets that have a magnetosphere, e.g. (Prangé et al., 2004). An important motivation for studying and understanding variations of the solar wind is related to their role in space weather, with growing awareness for its societal impacts (Lilensten and Bornarel, 2005; Lilensten et al., 2014).

The solar wind is above all a fascinating natural plasma laboratory (Bruno and Carbone, 2013a) that offers a precious connection between laboratory and astrophysical plasmas. Indeed, many fundamental processes such as reconnection can be studied *in situ* in the solar wind by means of satellites (Gosling et al., 2005; Phan et al., 2006; Gosling, 2012). The same processes can be studied only by remote sensing in astrophysical plasmas, or occur in laboratory plasmas on temporal/spatial scales that are often too small to be studied in a non-perturbative way (Zweibel and Yamada, 2009).

There are many open questions in solar physics studies, two of the outstanding ones are, the coronal heating problem and the sources of the solar wind. The former refers to the striking difference between the temperature at the surface of the Sun (approximately 5800 K) and in the solar corona (millions of degrees). The

Parameter	Mean	STD	Most Probable	Median	5–95% Range
n (cm^{-3})	8.7	6.6	5.0	6.9	3.0–20.0
V_{sw} (km/s)	468	116	375	442	320–710
B (nT)	6.2	2.9	5.1	5.6	2.2–9.9
A(He)	0.047	0.019	0.048	0.047	0.017–0.078
T_p ($\times 10^5$ K)	1.2	0.9	0.5	0.95	0.1–3.0
T_e ($\times 10^5$ K)	1.4	0.4	1.2	1.33	0.9–2.0
T_α ($\times 10^5$ K)	5.8	5.0	1.2	4.5	0.6–15.5
T_e/T_p	1.9	1.6	0.7	1.5	0.37–5.0
T_α/T_p	4.9	1.8	4.8	4.7	2.3–7.5
nV_{sw} ($\times 10^8$/cm^2 s)	3.8	2.4	2.6	3.1	1.5–7.8
C_s (km/s)	63	15	59	61	41–91
C_A (km/s)	50	24	50	46	30–100

FIGURE 1.1: Main solar wind parameter with their typical values at 1 AU, where the quantites are, proton number density (n), flow speed (V_{sw}), magnetic field strength (**B**), alpha particle abundance with respect to protons (A(He)), proton temperature (T_p), electron temperature (T_e), the alpha particle temperature (T_a), ratio of the electron and proton temperatures (T_e/T_p), ratio of alpha particle and proton temperatures (T_a/T_p), number flux (nV_{sw}), sound speed (C_s), and Alfvén speed (C_A) respectively taken from (Spohn, Breuer, and Johnson, 2014).

same difference is also observed in most stars, and so is truly an astrophysical rather than a solar problem. Most of the explanations that have been proposed involve the conversion of magnetic to kinetic energy and therefore particular attention has been given so far to the magnetic field (Velli et al., 2015; Sakurai, 2017).

Another major puzzle in astrophysics is the source of solar and stellar winds. The solar wind appears in two states that are historically named after their low (typically $200 < v < 400$ km/s) or high (typically $500 < v < 800$ km/s) velocity. The fast wind mainly emanates from regions of the solar surface (known as coronal holes) where the magnetic field lines directly open up into space. By contrast, the slow wind mainly originates near the equator of the Sun from so-called streamer belt regions where the magnetic field lines are mostly closed. The differences between the two states of the solar wind extend far beyond their speeds only: the slow wind is typically hotter and denser than the fast wind, and also has a somewhat different composition. The sources of the slow wind and the nature of the physical processes that can heat and accelerate the plasma so efficiently are not yet clearly understood. Incidentally, these open questions have motivated the launch in 2018 of the Parker Solar Probe mission, which is the first to probe the solar wind in the solar corona, going as close as 0.042 AU to the surface of the Sun.

The conditions and spatial properties of the solar wind are strongly modulated by the solar cycle. This activity cycle is characterized by a quasi-periodic reversal of the solar dipolar magnetic field occurring approximately every 11 years. Between these reversals, the large scale magnetic field evolves from a relatively simple dipolar field to a highly braided magnetic field whose complex topology strongly affects the motion of charged particles and therefore the solar wind (Balogh et al., 2014; Hathaway, 2015).

During periods of low solar activity (called solar minimum) the slow wind mostly emanate from streamers that are located near the equator of the Sun. Fast winds

originate at higher latitudes. At solar maximum, when solar activity peaks and the configuration of the large scale magnetic field is more complex, slow winds are generated at higher latitudes as well (McComas et al., 2008). These differences are well illustrated in Figure 1.2, which summarizes the latitudinal dependence of the solar wind speed with solar cycle. These data are from the *ULYSSES* spacecraft that made nearly 3 orbits around the Sun covering one pole to a another. The red coloured lines represent the inward interplanetary magnetic field (IMF) and the blue coloured lines represent the outward IMF. Between orbit 1 and orbit 3 we observe a reversal of the magnetic field (polarity) which corresponds to a new solar cycle.

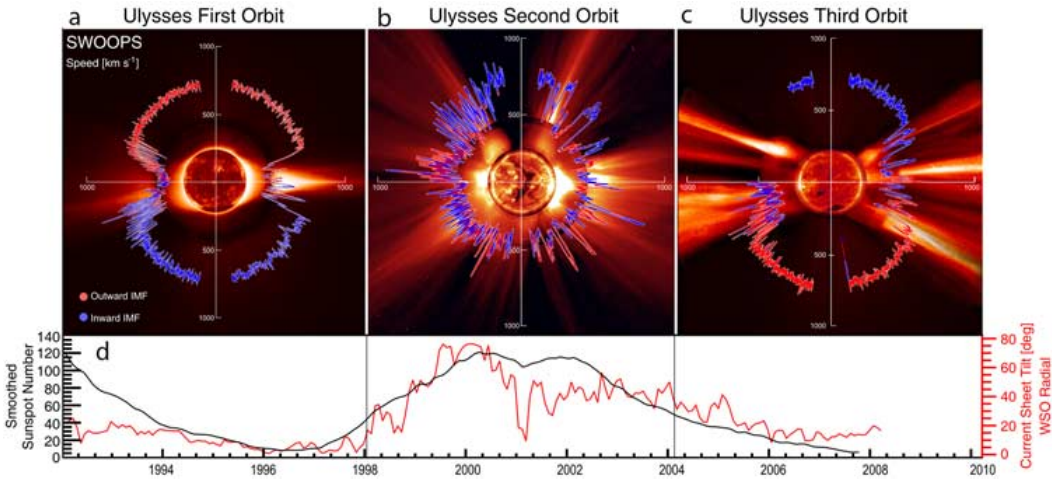

FIGURE 1.2: Polar plots of solar wind speed with respect to the heliolatitude for the three orbits of *ULYSSES* in panel (a), (b), and (c). The first orbit occurred mainly during solar minimum, while the second orbit spanned solar maximum and the third one a minimum. The solar wind speed is plotted over characteristic solar images for the solar minimum for cycle 22 (8/17/96), the solar maximum for cycle 23 (12/07/00), and the solar minimum for cycle 23 (03/28/06). The red and blue lines correspond to the outward and inward interplanetary magnetic field. The figure is a blend between images from the Solar and Heliospheric Observatory (SOHO) extreme ultraviolet imaging telescope (Fe XII at 1950 nm), the Mauna Loa K coronameter (700–950 nm), and the SOHO C2 white-light coronagraph. In panel (d) we can observe the sunspot number and the current sheet tilt as a function of the year, which corresponds to the conditions during the solar minima and maxima. Figure taken from McComas et al. (2008).

In this thesis we will address our research problem based on *in situ* measurements of the magnetic field. Let us therefore briefly present the main properties of the solar wind magnetic field, the particle population and their radial variations in the inner heliosphere.

1.1.1 Magnetic field

The magnetic field that permeates the inner heliosphere is generated by the solar dynamo that converts convective motion and differential rotation within the Sun into electric and magnetic energy. This magnetic field then extends through the solar

corona and eventually through the heliosphere (Russell, 2001). Since the solar corona and the solar wind are both excellent electrical conductors, the magnetic field is essentially frozen in the moving plasma (Spohn, Breuer, and Johnson, 2014). For the solar wind, this means that the magnetic field is carried by the outward flowing plasma. This motion, together with the rotation of the Sun (with an average period of 27 days) generates in the equatorial plane large scale Archimedean spirals that have been named after Eugene Parker, the scientist who laid the foundations of modern solar wind science (Parker, 1958).

While the solar wind magnetic field has a regular spiral topology at large scales, at smaller scales (typically less than 0.1 AU) it becomes highly complex and is continuously evolving. These complex dynamics are generated either by interplanetary perturbations that emanate from the Sun and then propagate outwards (often with speeds superior to that of the solar wind) such as coronal mass ejections or to the interplay between physical processes that can lead to shocks, waves or turbulent cascades. During more quiescent periods when there are no such transients, the solar wind mostly consists of entangled and meandering magnetic flux tubes that are remnants of structures that are anchored deep in the corona (Borovsky, 2008).

On large scales, the radial component of the magnetic field should vary as $B_r \propto R^{-2}$, whereas the tangential component (B_t) is expected to vary as R^{-1}. Recent studies in the fast wind in the inner-heliosphere (0.3 to 1 AU) have indeed shown that the radial variation of the radial and tangential components is respectively $B_r \propto R^{-1.81}$ and $B_t \propto R^{-1.21}$ (Perrone et al., 2019).

In our work we have used the magnetic field measurements from the HELIOS-1 spacecraft (Musmann, Neubauer, and Lammers, 1977; Neubauer et al., 1977) and also from the WIND spacecraft (Lepping et al., 1995) for our analysis.

1.1.2 Turbulence in the solar wind magnetic field

One particular aspect of the solar wind magnetic field that has received considerable attention is the omnipresence of turbulence with universal properties that are reminiscent of what is found in laboratory and in astrophysical plasmas, and also in neutral fluids (Goldstein, Roberts, and Matthaeus, 1995; Bruno, 2019). The large interest devoted to solar wind turbulence is motivated by its connections with other astrophysical phenomena such as cosmic ray propagation, galaxy formation, stellar winds, and accretion.

Turbulence can be described as a complex and nonlinear motion of the plasma that involves a broad range of temporal and spatial scales and leads to energy cascades across scales, enhanced transport, mixing, and eventually to dissipation (Frisch, 1995). Turbulence is involved in the origin of the solar magnetic field and also plays a key role in the heating and acceleration of the solar wind (Breech et al., 2009; Cranmer et al., 2015). From the initial evidence of active turbulence in solar wind (Coleman, 1968), it is understood that the solar wind provides with a fascinating laboratory for studying *in situ* the evolution of plasma turbulence over a wide range of scales from the energy injection to the dissipation (Bruno and Carbone, 2013a).

To sustain turbulence a persistent source of kinetic energy is required. In the solar wind, this source is rooted in the solar atmosphere although large-scale structures such as shocks can also contribute. Both mainly act on large scales that typically correspond to characteristic times of days and beyond in spacecraft measurements. This kinetic energy is then converted into viscous shear stress and leads to the formation of self-similar eddies with smaller scales. Such eddies are loosely defined as coherent patterns of velocity, density or magnetic field, with no specific shape. The

heuristic picture is that of an energy cascade that generates these eddies (Bruno and Carbone, 2016); the range of spatial scales over which this cascade occurs is called the inertial range. At large scales, the turbulent cascade is dominated by the presence of large coherent structures that emanate from the solar atmosphere. That range of non fully developed turbulence is commonly known as the f^{-1} range because its power spectral density scales as $P(f) \propto f^{-1}$ (Matthaeus and Goldstein, 1986; Bruno and Carbone, 2013b; Matteini et al., 2018). At the other side of the inertial range, when the time scale becomes comparable to that of the characteristic times of the particles (e.g. ion gyrofrequency, electron gyrofrequency), the fluid-like description of the plasma breaks down. This is where we leave the MHD description of plasma turbulence for a kinetic description, in which particles play a leading role. The energy continues to cascade to smaller scales until the dissipation of energy dominates.

In the solar wind, the spectral energy cascades from large to small spatial scales not from long to short time scales. However, most measurements are carried out by single spacecraft. Therefore, the spectral features are best resolved in the frequency domain, and not in wavenumbers. However, a direct connection between the two exists thanks to the *Taylor hypothesis* (Taylor, 1938; Treumann, Baumjohann, and Narita, 2019), which states that when turbulent eddies are frozen in the solar wind, they can be considered as being static during the period when they are advected past the spacecraft. For a spatial Fourier mode with wave-vector $\mathbf{k}$, the relation between the observed frequency ω_{sc} in the spacecraft frame to the wave frequency ω in the plasma frame, for a solar wind velocity $\mathbf{v}_{sw}$ is

$$\omega_{sc} = \omega + \mathbf{k} \cdot \mathbf{v}_{sw}. \tag{1.1}$$

The Taylor hypothesis holds when the wind velocity is considerably larger than the phase velocity of the waves

$$|\omega| \ll |\mathbf{k} \cdot \mathbf{v}_{sw}| \tag{1.2}$$

so that the frozen in condition can be assumed, and therefore

$$\omega_{sc} \approx \mathbf{k} \cdot \mathbf{v}_{sw}. \tag{1.3}$$

Using this Eq.1.3 in our work we transform from temporal scales to spatial scales. However, when Eq.1.2 does not hold, then the convenient correspondence between wavenumber and frequency breaks down. In the solar wind, such conditions typically arise with dispersive waves, in slow flows (Klein, Howes, and TenBarge, 2014) or deep in the corona, inside the Alfvén critical point (Bourouaine and Perez, 2018). Therefore, while the Taylor hypothesis safely holds for the f^{-1} and inertial ranges, it breaks down in the kinetic range, especially when moving closer to the Sun, where the characteristic frequencies of waves are higher.

1.1.3 Solar wind electrons

In the highly conducting solar wind, electrons play a major role in the dissipation of energy by interacting with waves and dissipating energy at small scales. Because of their light mass electrons carry a major share of the heat flux and play a crucial role in explaining the flow of thermal energy (Feldman et al., 1975).

A typical cut of an electron distribution function in the solar wind is shown in Figure 1.3, where we can observe that the maximum of the phase space density is present around the origin of (V_x, V_y) coordinate system. We can also observe that the electron distribution function is anisotropic.

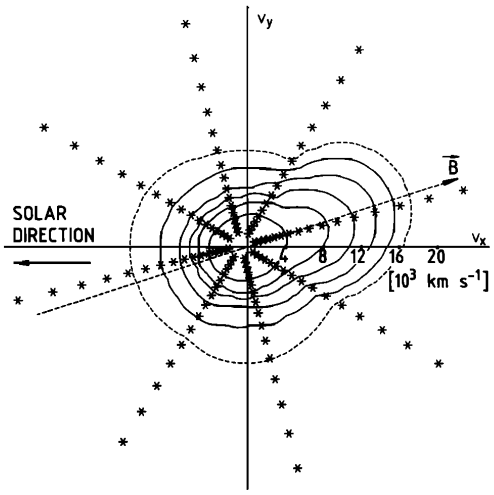

FIGURE 1.3: A cut through the observed electron velocity distribution function along the plane of measurement (along the ecliptic plane) using data from *HELIOS*. The contour lines represent the phase space density that is logarithmically spaced and the stars represent the centers for the channels of measurement. The dashed line indicates the projection of magnetic field direction onto the ecliptic plane, along which the measurements are made. Figure taken from Pilipp et al. (1987).

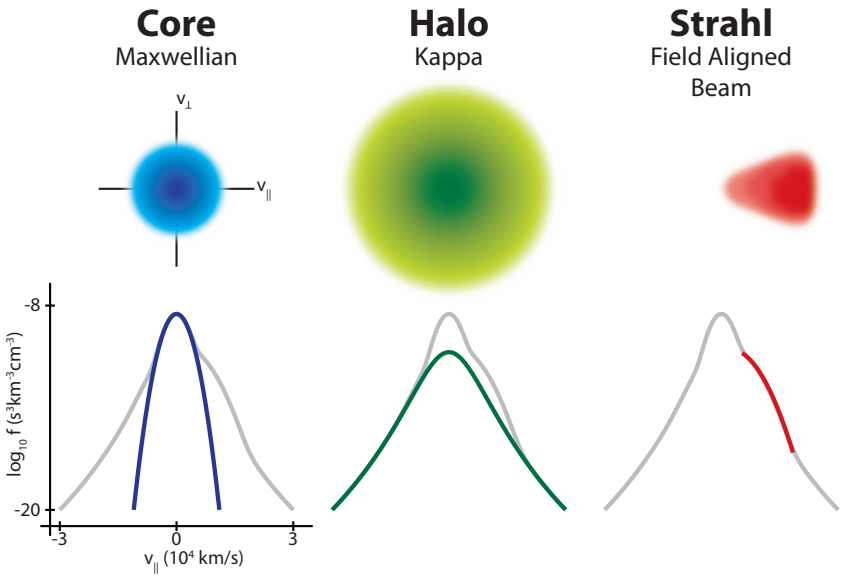

FIGURE 1.4: Schematic of different components of solar wind electron velocity distribution. Here we show a symmetric Core with a Maxwellian function, a high energy Halo with a kappa function and also show the magnetic field aligned beam like population termed as Strahl, courtesy of Marc Pulupa

The anisotropic electron distribution in the solar wind can be separated into three main populations that are illustrated in Figure 1.4.

- Core: this part represents the bulk of the total population (typically 96%) and is essentially Maxwellian.
- Halo: this non-Maxwellian distribution is sparsely populated and has higher temperatures. This populations tends to follows a kappa distribution (Maksimovic et al., 2005).
- Strahl: this very sparsely populated population represents a narrow beam that is aligned with the magnetic field direction, away from the Sun. Together, halo and Strahl make up nearly the remaining 4 % of the electron population.

In Figure 1.5 we present how the main parameters associated with solar wind electrons, such as number density (n_e), temperatures ($T, T_\perp, T_\parallel$) and heat flux ($q, q_\perp, q_\parallel$) are varying with radial distance in the slow and fast winds, in the inner heliosphere. In our studies $\parallel$ and $\perp$ are always with respect to the mean magnetic field (**B**).

The radial evolution of the number density in the slow solar wind scales as $n \propto r^{-2.03}$, which corresponds to nearly theoretical radial expansion. In the fast wind, however, a slower decrease is observed $n \propto r^{-1.83}$ because of a plasma compression in the decelerated radial expansion (Stverák, Trávníček, and Hellinger, 2015). A detailed discussion on the reasons behind the different radial variations of the temperature and the heat flux values can be found in (Pilipp et al., 1990; Stverák, Trávníček, and Hellinger, 2015).

In our work we have worked with the electron data from the HELIOS 1 mission, the electron moments such as density and temperature taken from the work of Štverák et al. (2009).

1.1.4 Solar wind protons

Solar wind protons represent on average 92 % of the mass in the solar wind, while the remaining 8 % mostly consist of alpha particles and also heavier ions in minute concentrations. Protons therefore are important for determining the bulk velocity of the solar wind; their velocity is usually considered for separating fast and slow winds (Meyer-Vernet, 2012).

The proton population in the solar wind is generally less anisotropic than that of the electrons. Most of the proton population is Maxwellian, with a small field-aligned beam of protons whose speed is of the order of the local Alfvén speed (Marsch et al., 1982). An example of proton distributions in the inner-heliosphere is shown in the Figure 1.6. A strong deviation from a Maxwellian occur closer to the Sun, with large anisotropies in the perpendicular direction to the mean magnetic field (dashed line) and also proton beams along the field (Marsch, 2010).

Figure 1.7 shows how the solar wind proton properties such as density and temperature vary in different types of solar wind separated on the basis of velocity with the radial distance (0.3 to 1 AU). As for the electrons, in the slow wind the number density of protons decreases faster than expected from mass conservation ($n \propto r^{-2.07}$ instead of $n \propto r^{-2}$) while in the fast wind the decrease is slower. The reason is that the slow solar wind is expected to be accelerating, while the fast solar wind is decelerating between 0.3 AU and 1 AU (Stansby et al., 2018). Solar wind protons are highly non-adiabatic as their temperature drops more slowly with the radial distance from the Sun (Marsch et al., 1983) than the $T_p \propto R^{-4/3}$ scaling one would expect for an adiabatic process (Chew, Goldberger, and Low, 1956). For further discussions on these properties, see Marsch et al. (1982) and Stansby et al. (2018).

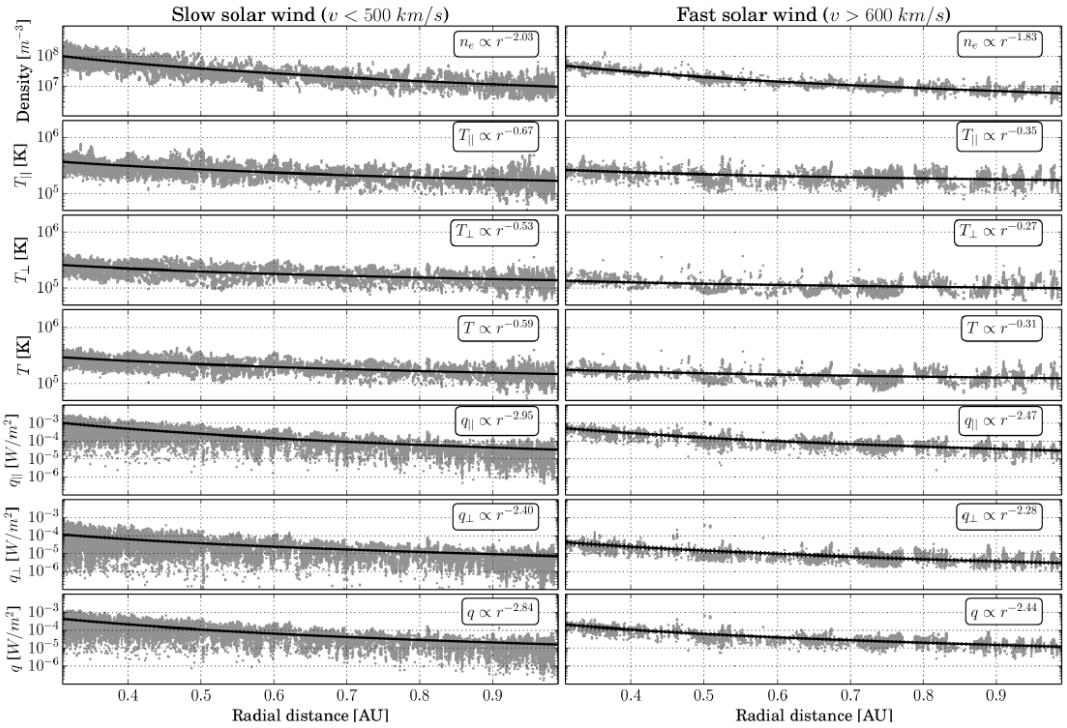

FIGURE 1.5: Radial variation of different electron properties from 0.3 to 1 AU using *HELIOS* data. Panels from top to bottom correspond to electron density, parallel temperature, perpendicular temperature, total temperature, parallel heat flux, perpendicular heat flux and total heat flux respectively. Figure taken from Stverák, Trávníček, and Hellinger (2015)

In our work we have worked with the proton moments such as density, velocity and temperature from the HELIOS 1 (Schwenn, Rosenbauer, and Miggenrieder, 1975) and WIND (Lin et al., 1995) missions.

1.2 Outline of this thesis

This thesis can be summarized as a contribution to a few general problems in the solar wind, such as understanding the nature of solar wind magnetic field turbulence, inherent behavior of non-stationarity and the presence of whistler waves.

The overall context of this thesis is the solar wind in the inner heliosphere, with focus on the properties of the magnetic field, based on data from the *WIND* (1994–) and *HELIOS* (1974–1985) spacecraft, in preparation for the exploitation of the data from the Parker Solar Probe and Solar Orbiter missions. Here we give a brief description of problems tackled and the questions raised. These questions and the terminology used here will be explained in detail in the next chapters.

- Evolution of solar wind turbulence from injection to the dissipation scale and also the radial evolution of turbulence in the inner heliosphere.

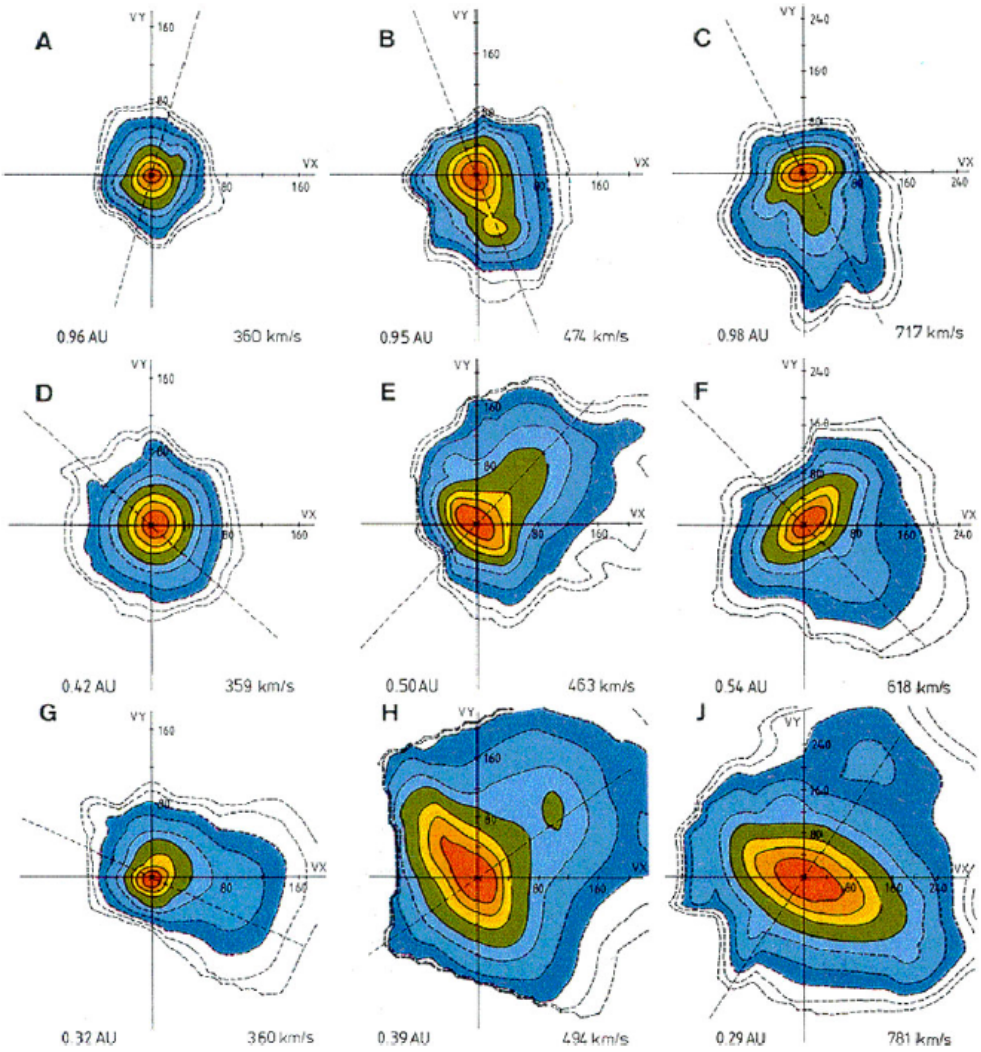

FIGURE 1.6: The isocontours shown are the cuts through the proton velocity distribution functions in the ecliptic plane for different solar wind velocities at different distances from the Sun, with the dashed line giving the magnetic field projection, courtesy of Marsch (2010).

- Is there evidence for a f^{-1} frequency dependence in the power spectral density of magnetic field fluctuations in the non-Alfvénic slow solar wind? If there is one, how do the non-Alfvénic slow wind non-linear times compare with the fast wind non-linear times?
- Is there anything common between the turbulence evolution in the fast and slow winds?
- How do the turbulence spectra behave at kinetic scales?
- How is the turbulence evolving radially at different scales in the inner heliosphere?
- Is there a general picture for the turbulence evolution from the point of energy injection to the dissipation?

There are different reasons behind choosing the above-mentioned questions in turbulence studies. The idea to look into the low-frequency scales of slow wind

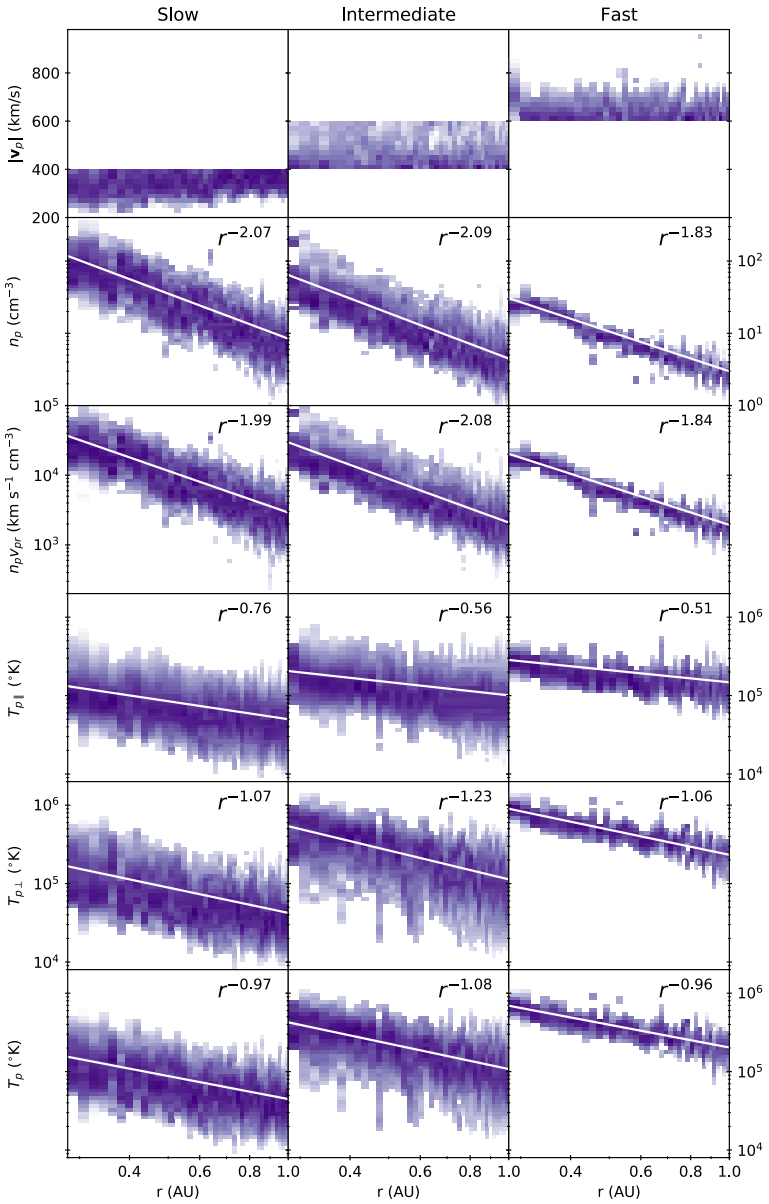

FIGURE 1.7: Radial variation of proton core population properties from 0.3 to 1 AU for different types of solar wind based on the proton velocity using the *HELIOS* data. From top to bottom the panels represent, velocity of the protons, density of the protons, radial flux, parallel proton temperature, perpendicular proton temperature and the total proton temperature respectively. Figure taken from Stansby et al. (2018)

came with the curiosity to know whether we can probe the initiation of Kolmogorov like spectra in the slow wind which was not identified before. This study is important as we can identify the initiation of the non-linear cascade in the slow wind so that we can study the differences and similarities in the turbulence evolution of slow and fast wind.

Studies on the scaling of spectra in the inertial range are widely studied at

different radial distances, however, the kinetic scale spectra have not been analyzed in the solar wind beyond the dissipation scale except at 1 AU. We probe how the turbulence spectra in the kinetic scale behave in the solar wind at different radial distances. This gives us the information on whether there is some generalized behavior of the spectra from the injection to the dissipation all the distances.

- Understanding the inherent behavior of non-stationarity in the solar wind.
  - Are the measurements of the magnetic field in solar wind stationary? If not, at what scales does non-stationarity become dominant? and; How does this relate to the analysis of properties of plasma fluctuations in the turbulent cascade?

  Our studies of non-stationarity have important consequences in the solar wind turbulence analysis, the stationarity sensitive statistical tool such as auto-correlation function which is generally used in the solar wind analysis is highly affected if the considered measurements are not stationary.

- Identification of the whistler waves, studying different properties of the observed whistler waves in the inner-heliosphere and relating the observed whistler properties to their generation mechanisms.
  - How are whistler waves distributed in the inner heliosphere and how does their presence change with solar wind velocity?
  - Are the observed whistler properties related to the conditions of whistler wave generation?

The study of the whistler waves in the inner heliosphere is very important as they are thought to provide a significant contribution to the control of global solar wind thermodynamics and energy transport.

This manuscript has six chapters, including the present introduction. In Chapter 2 we describe the *HELIOS* mission whose data we used to address most of the questions listed above. We explain the mission objectives and describe the fluxgate and the search-coil magnetometers that make magnetic field measurements.

Chapter 3 is dedicated to solar wind turbulence in the inner heliosphere, based on *HELIOS* 1 magnetic field data for the inner heliosphere and *WIND* data at 1 AU. We show the presence of a f^{-1} scaling of the power spectral density at very large scales in the non-Alfvénic slow solar wind for the first time. From this, and using estimates of the non-linear times at the injection scale we discuss the similarities and differences in the nature of the slow and fast winds. In the second part of that chapter, we turn to small scales beyond the dissipation scale and discuss the universality of the shape of the power spectral density for different distances from the Sun.

Chapter 4 addresses the problem of non-stationarity in the solar wind through a large statistical study of magnetic field data from the *WIND* spacecraft. Using the properties of the autocorrelation function we show that the solar wind is inherently non-stationary in the inertial regime and at larger scales. Most of the material presented in Chapter 4 is taken from Krishna Jagarlamudi et al. (2019).

In Chapter 5 we investigate the presence of whistlers in the inner heliosphere and study their properties. We then make a connection between their observed properties in slow and fast winds at different radial distances from the Sun and relate these

to a possible generation mechanism by considering the ratio between perpendicular and parallel temperature of the halo electrons $T_{\perp h}/T_{\parallel h}$.

Finally, in Chapter 6 we conclude and present some outlooks.

1.3 Résumé en français: Introduction

Ce premier chapitre pose le cadre de cette étude, à savoir l'étude du vent solaire et de son évolution radiale entre le Soleil et la Terre. Le vent solaire est un flux de particules chargées qui sont émises par le soleil et se propagent dans le milieu interstellaire à une vitesse supersonique. Ce plasma non collisionnel mais très dynamique subit des fluctuations à toutes les échelles de temps.

Le vent solaire est souvent considéré comme le laboratoire par excellence de la turbulence plasma. En effet, grâce aux satellites il est possible d'étudier ses propriétés sans le perturber. En ce sens, le vent solaire permet d'étudier de manière *in situ* des mécanismes physiques fondamentaux qu'on retrouve à des échelles spatiales et temporelles bien plus petites dans les plasmas de laboratoire, ou au contraire, à des échelles considérablement plus grandes (et sans la possibilité de faire des mesures in situ) dans les plasmas astrophysiques.

Pour étudier le vent solaire nous disposons de divers satellites sont la plupart se situent à proximité de la Terre, c'est-à-dire à 1 unité astronomique (UA). Or les propriétés du vent solaire évoluent entre leur source (la couronne solaire) et le milieu interplanétaire. Il est donc particulièrement intéressant de pouvoir étudier le vent solaire à différentes distances du Soleil. La mission HELIOS (1974-1985) est une des rares à l'avoir fait avant le lancement de Parker Solar Probe en 2018. Dans ce travail nous nous concentrerons plus particulièrement sur le champ magnétique. En effet cette quantité est relativement facile à mesurer et joue un role-clé dans la dynamique du vent solaire.

Le chapitre 2 de la thèse est consacré à la description de la mission HELIOS et de ses divers instruments.

Le coeur du travail se situe dans dans les chapitres 3 à 5, dans lesquels nous abordons différentes questions. Bien qu'indépendantes de prime abord, toutes ces questions sont liées aux propriétés fondamentales du vent solaire.

Dans le chapitre 3: l'évolution radiale de la turbulence dans l'héliosphère interne. Qu'est-ce qui détermine le démarrage du régime inertiel dans le vent solaire ? Existe-t-il un régime universel de la turbulence aux échelles cinétiques ?

Dans le chapitre 4: le rôle des ondes de type whistler. Comment ces ondes sont-elles réparties dans l'héliosphère interne et que peut-on en déduire sur leurs conditions de génération ?

Dans le chapitre 5: la questions de la stationnarité dans le vent solaire. Le vent solaire est-il stationnaire ? Si non, à quelles échelles l'est-il ?

Chapter 2

The HELIOS mission

2.1 Introduction

This thesis entirely relies on plasma data collected by two spacecraft: *HELIOS* 1 and *WIND*. However, while a large amount of easily accessible literature has been devoted to the instruments of *WIND*, the instruments of *HELIOS* 1 have been far less well documented. This is particularly so for its search-coil magnetometer data, which is one of the main instruments of interest in this thesis.

In this chapter, we shall focus on the *HELIOS* 1 mission and mainly address the working and the data outputs from its two magnetic sensors: the fluxgate and the search-coil magnetometer. Information regarding the *WIND* mission and its instruments will be provided directly in the subsequent chapters, where appropriate.

2.2 The HELIOS Mission

HELIOS was the first mission to penetrate deep into the inner heliosphere, going as close as 0.3 AU from the Sun (Porsche, 1981). This distance is comparable to the distance of Mercury to the Sun when the planet is at perihelion. The mission consisted of two spacecraft, *HELIOS* 1 and *HELIOS* 2. *HELIOS* 1 which was launched on 10 Dec 1974 had its closest perihelion distance of 0.309 AU while *HELIOS* 2 which was launched a year later on 15 Jan 1976 and had its closest perihelion distance of 0.290 AU. Both orbits are in the ecliptic plane with an eccentricity of respectively 0.5218 and 0.5456, and orbital periods of 190 and 187 days. The *HELIOS* 1 probe is illustrated in Figure 2.1 and a schematic of the orbits is shown in Figure 2.2.

After providing the first of its kind in-situ measurements in the inner heliosphere, the *HELIOS* 1 and 2 got deactivated on February 18, 1985, and December 23, 1979, respectively. The *HELIOS* 2 held the record of the fastest man-made object for over 4 decades until the *Parker Solar Probe* surpassed it in October of 2018.

2.2.1 Objective

The main objective of the *HELIOS* mission was to investigate the interplanetary fields and matter prevailing in the inner-heliosphere down to 0.3 AU using the in-situ measurements, especially the ion-composition, dynamics and the dynamics of the fields (Porsche, 1981).

Each one of the *HELIOS* probes had ten scientific instruments onboard. They are:

- Plasma Experiment: To measure the distribution functions of different particles such as electrons, protons, and alpha particles in solar wind plasma.
- Fluxgate Magnetometers (two): To measure the magnetic field vectors up to 4 Hz.

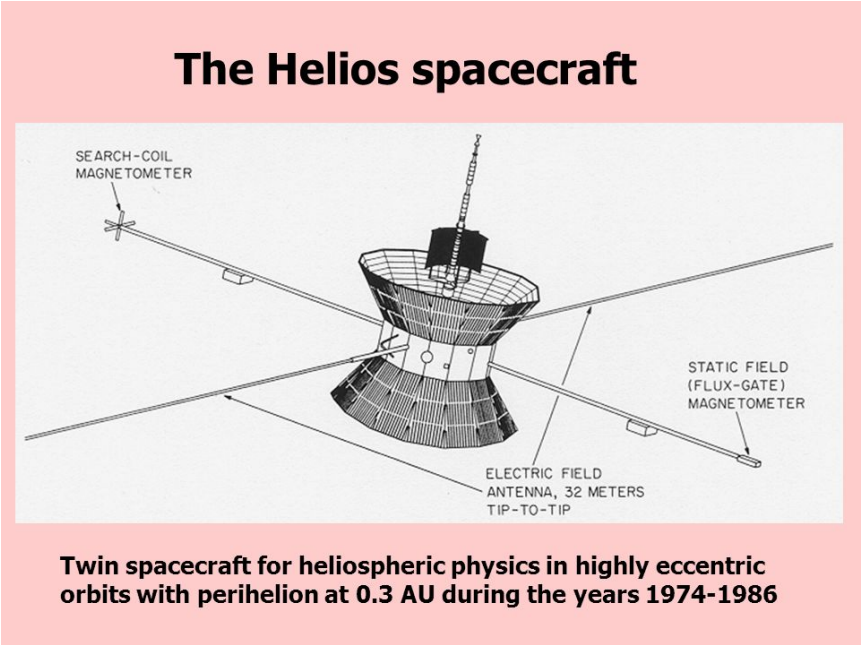

FIGURE 2.1: Helios probe with FGM and SCM. Courtesy of Eckart Marsch.

- Search-Coil magnetometer: To measure the rapidly varying magnetic field fluctuations up to 2200 Hz.
- Plasma wave experiment: To measure the electric component of plasma waves.
- Cosmic Radiation experiments (two): To measure the high-energy charged particles of solar, planetary and galactic origin in the inner heliosphere.
- Low-energy electron and ion spectrometer: To investigate the higher energy region between the solar wind particles and the cosmic rays.
- Zodiacal light photometer: To measure the intensity of the zodiacal light at different angles to the ecliptic and in different wavelength ranges.
- Micrometeoroid Analyser: To investigate the mass, charge, velocity, composition and also the direction of interplanetary dust particles.

In what follows we shall mostly focus on magnetic field fluctuations, for which we use data from two instruments: the fluxgate magnetometer and the search-coil magnetometer. We will also be using the output parameters of the plasma experiment for our analysis. This instrument measures the distribution of different solar wind particles and gives us access to the bulk velocity, the proton density, and temperatures of the electrons and protons, which will all be used in our analysis.

Let us first address the coordinate system used by the spacecraft before dwelling on these different instruments.

2.3 Coordinate systems

In *HELIOS* the value of the magnetic field is measured in the spacecraft so that a coordinate transformation is necessary to express them in a physically more relevant

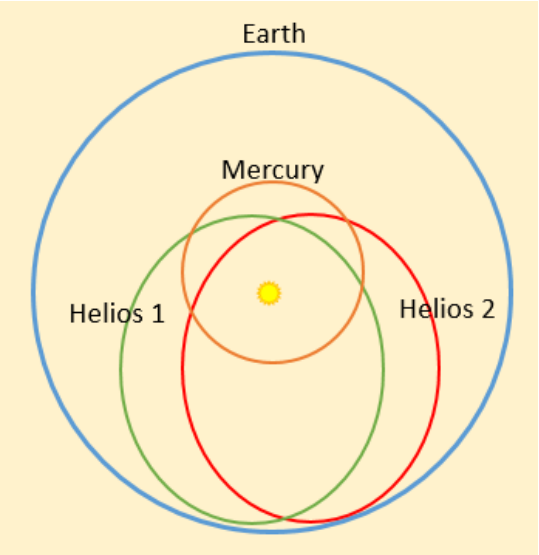

FIGURE 2.2: Illustration of the *HELIOS*-1 and *HELIOS*-2 trajectories

frame. *HELIOS* uses the Solar Ecliptic Coordinate System (SE), which is a heliocentric coordinate system with the Z-axis being normal and pointing northwards with respect to the ecliptic plane, the X-axis is pointing towards the Sun and the Y-axis in the ecliptic plane with its orientation opposite to the orbital motion (Hapgood, 1992). The reference system is shown in Figure 2.3. This is the reference frame that we shall use throughout.

Some of the data from *HELIOS* have also been registered in the RTN coordinate system. In this system, the R axis is along the radial direction, but the positive is from the Sun to the spacecraft, the T=$\frac{\Omega \times R}{|\Omega \times R|}$, where Ω is sun's spin axis and N ($R \times T$) completes the right-handed triad. The RTN system is illustrated in Figure 2.3. The conversion from RTN to SE is simple, R $\sim$ -X, T $\sim$ -Y, and N $\sim$ Z.

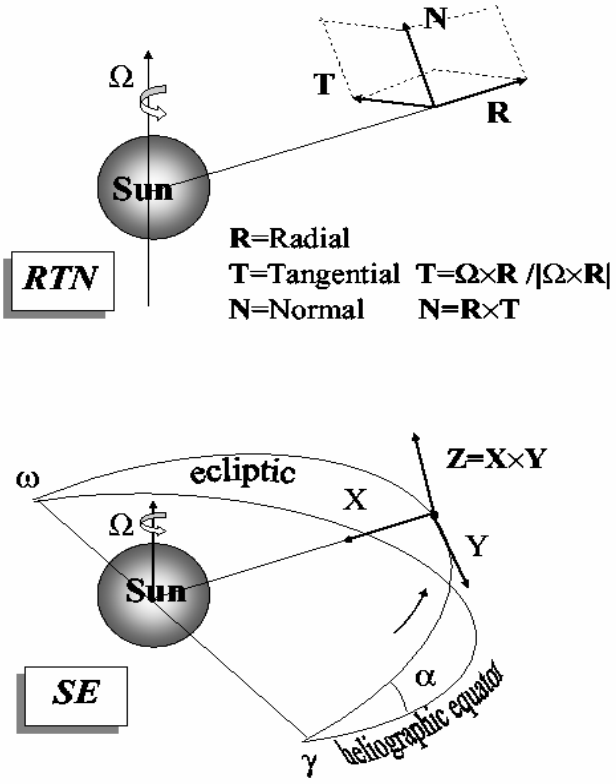

FIGURE 2.3: Schematic of RTN and SE coordinated system. Figure taken from Bruno and Carbone (2013b)

2.4 Magnetometers

Both *HELIOS* spacecraft are equipped with fluxgate magnetometers that can measure DC magnetic fields and a search-coil magnetometer for measuring AC magnetic field fluctuations. Both instruments are located on booms to reduce the impact of interference noise coming from the spacecraft, see Figure 2.1.

2.4.1 Fluxgate magnetometer onboard HELIOS

The flux-gate magnetometer (FGM) can be found onboard most missions in the solar wind and provides access to the in situ vector magnetic field. The instrument measures variations in the relative permeability of a periodically saturating ferromagnetic core (Miles et al., 2018). By placing three sensors orthogonally to each other we have a full set of vector magnetic field measurements. FGM cannot be used for the study of very high-frequency magnetic field fluctuations, due to the limitations on the input frequency of the current and also the material property. For a detailed description see Ness (1970) and Acuña (2002).

There are two fluxgate magnetometers (E2 & E3) onboard *HELIOS* 1 & 2: E2 has been developed by the University of Braunschweig (Germany) and E3 by the University of Rome and NASA (Goddard Space Flight Center). In our study, we

shall only use data from the E2 instrument because these has been better preserved and allow for comparisons with the search-coil magnetometer onboard the same spacecraft.

The FGM of *HELIOS* 1 is made up of tri-axial, orthogonal flux-gate sensors, which are mounted on a boom of 2m. The distance between the sensors and the center of the spacecraft is nearly 2.75m (Musmann et al., 1975; Musmann, Neubauer, and Lammers, 1977). There are four measuring ranges with automatic switching with a sensitivity range of $\pm$100 nT and $\pm$400 nT and the highest resolution is $\pm$0.2 nT (Musmann, Neubauer, and Lammers, 1977).

The value of the magnetic field are measured spin-synchronously, where the spin frequency of the spacecraft was 1 Hz with the spin axis parallel to the Z-axis in the case of *HELIOS* 1 and it was anti-parallel to the Z-axis for the *HELIOS* 2. The sampling rate went up to 4 Hz, which was achieved for many long time-intervals during the initial mission period. We use this high-resolution magnetic field data for our analysis. Therefore, the maximum Nyquist frequency was 2 Hz. Frequencies around 1 and 2 Hz are affected by the strong spin tones of the spacecraft and therefore should be analyzed with great care.

While working with the magnetic field measurements made using the FGM on board the *HELIOS* 1, we learned that the FGM had a saturation issue. Indeed, the magnitude of the magnetic field never exceeds 50 nT, see Figure 2.4. The problem hinders the analysis of magnetic field data near perihelion and during fast solar wind streams, as in Figure 2.4. However, this saturation has no impact at other distances.

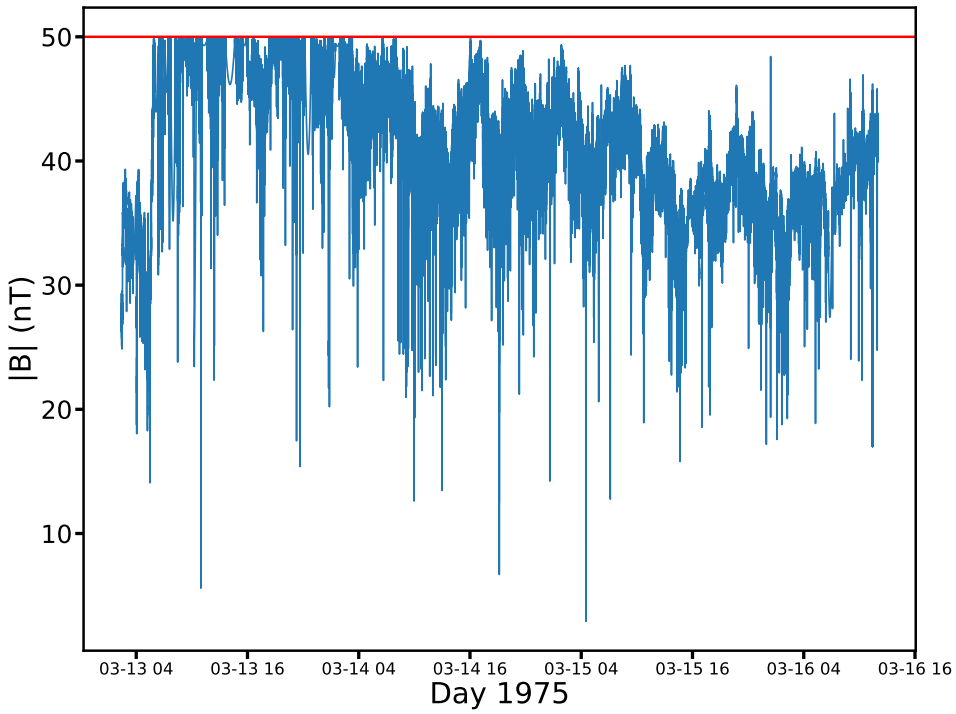

FIGURE 2.4: Magnitude of magnetic field at the first perihelion of *HELIOS* 1. The horizontal red line indicates the saturation amplitude of 50 nT

2.4.2 Search coil magnetometer onboard HELIOS

The working principle of the search coil magnetometer is based on the Faraday's law of magnetic induction, which states that any variations in the magnetic field (**B**) environment of a coil of wire will generate an electric field (**E**) (Hospodarsky, 2016)

$$\nabla \times \mathbf{E} = -\frac{\partial \mathbf{B}}{\partial t}, \tag{2.1}$$

where **E** is the electric field vector and **B** is the magnetic field vector. The integrated electric field gives the voltage (**V**),

$$V = \int E \cdot ds \propto \frac{\partial \mathbf{B}}{\partial t} \tag{2.2}$$

We can understand from the above equation that the search coil magnetometer does not respond to the steady magnetic field and is insensitive to slowly varying magnetic fields. For example, if the magnetic field is varying sinusoidally with frequency ω, then

$$V \propto \omega B. \tag{2.3}$$

From equation 2.3 we can observe that the sensitivity is a linear function of frequency, which explains why the search coil magnetometers are used to measuring

the fluctuating field and very rarely for the steady fields. For a detailed description of the working of SCM, we refer to Ness (1970) and Hospodarsky (2016).

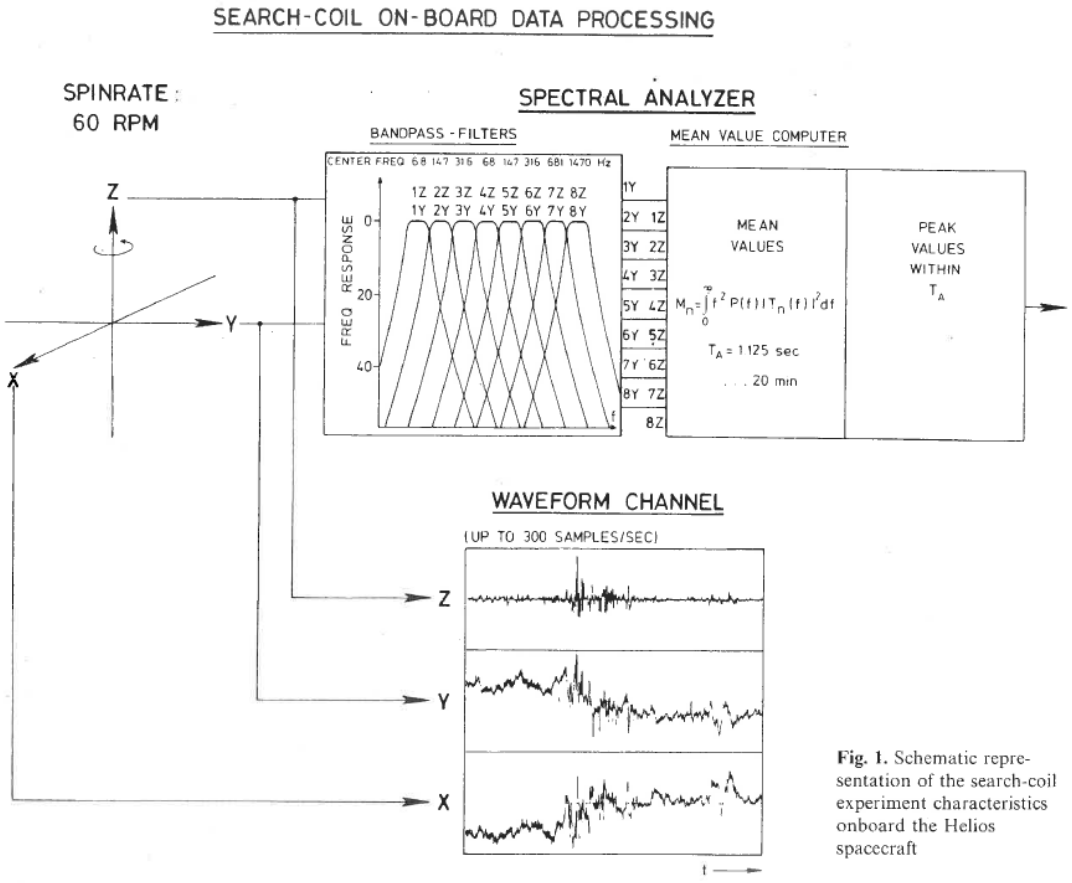

Fig. 1. Schematic representation of the search-coil experiment characteristics onboard the Helios spacecraft

FIGURE 2.5: Schematic of the search-coil experiment onboard of the *HELIOS* spacecraft. It gives out two different forms of output, one is direct waveform data and another is the spectral density values (mean and peak) processed onboard the spectrum analyzer. In the spectrum analyzer, the waveform signal along the Z and X/Y is the first band passed on 8 different logarithmically spaced frequency channels and then a mean value computer onboard calculates the mean value for each spectral band over time T_A and the peak value is also measured in the time interval T_A.Figure taken from Neubauer et al. (1977).

The Search-coil magnetometer onboard *HELIOS* was developed by the University of Braunschweig, Germany (Dehmel et al., 1975). The instrument consists of 3 orthogonal search-coil sensors to measure the three components of the magnetic field, the X and Y axis are in the equatorial plane and the Z-axis is parallel to the spin-axis (Neubauer et al. (1977)). The onboard data processing system is illustrated in Figure 2.5. Unfortunately, the waveform data from the SCM were completely lost, as were a large fraction of the spectral densities. The latter play an important role in our analysis.

Frequency-range (Hz)	Central-frequency (Hz)	Channels
4.7-10	6.8	X1/Y1, Z1
10-22	14.7	X2/Y2, Z2
22-47	31.6	X3/Y3, Z3
47-100	68	X4/Y4, Z4
100-220	147	X5/Y5, Z5
220-470	316	X6/Y6, Z6
470-1000	681	X7/Y7, Z7
1000-2200	1470	X8/Y8, Z8

TABLE 2.1: The frequency range and the central frequencies of the 8 logarithmically spaced band pass filters for the three components X, Y, Z.

The spectrum analyzer processes the Z-component and one of the X and Y components. Spectrum analyzer consists of 8 logarithmically spaced bandpass filters in frequency. The frequency range and the central frequencies of the bandpass filters are shown in Table 2.1. The output from the filters is squared and a digital mean value computer onboard averages the squared values over successive time intervals of length T_A (Neubauer et al., 1977). The peak values from the same interval T_A along with the mean square values are transmitted to earth.

The relation between the mean square values(M_n) computed using the spectral analyzer and the power spectral density $P(f)$ of an individual magnetic field component is

$$M_n = \int_0^\infty |T_n(f)|^2 f^2 P(f) df, \tag{2.4}$$

where $T_n(f)$ is the complex transfer function of channel n and $T_n(f)$ is such that, at central frequency (f_{cn}), $T_n(f_{cn}) = 1$ and quickly tends to 0 beyond the 3dB-points for each filter.

Hence, the power spectral densities $\overline{P}_n$ are assigned to the central frequency (f_{cn}) and are given by

$$\overline{P}_n = \frac{M_n}{\Delta f_n f_{cn}^2} = \int_0^\infty |T_n(f)|^2 (f/f_{cn})^2 P(f) \frac{df}{\Delta f_n} \tag{2.5}$$

or

$$\overline{P}_n(f_{cn}) \approx \int_{f_{ln}}^{f_{un}} P(f)(f/f_{cn})^2 \frac{df}{\Delta f_n} \tag{2.6}$$

Where, f_{ln} and f_{un} are the lower and upper frequency limits (3 dB-points) of the respective channel n, and $\Delta f_n = f_{un} - f_{ln}$ is the bandwidth of the channel n.

The noise level of the *HELIOS* 1 SCM for the Y and Z components of *HELIOS* 1 is shown in the Figure 2.6, along with the noise levels of other contemporary instruments. For the Y component, the pre-flight and in-flight measurements of the noise level were found to be very much similar, but the Z-component was observed to be affected by the stray magnetic fields (Neubauer, Musmann, and Dehmel, 1977), which can be seen in the Figure 2.6 as a bump.

We have also verified the validity of the background noise level (BGN) mentioned in the studies of Neubauer, Musmann, and Dehmel (1977). For this purpose we have followed a similar analysis as suggested by them, i.e. looking into periods when the Sun was quiet and comparing the PSD values with the suggested BGN

Frequency-range (Hz)	Central-frequency (Hz)	BGN (nT^2/Hz)	Channels
4.7-10	6.8	$5.4 \cdot 10^{-7}$	Y1
10-22	14.7	$6.1 \cdot 10^{-8}$	Y2
22-47	31.6	$1.5 \cdot 10^{-8}$	Y3
47-100	68	$3.7 \cdot 10^{-9}$	Y4
100-220	147	$2.4 \cdot 10^{-9}$	Y5
220-470	316	$7.6 \cdot 10^{-10}$	Y6
470-1000	681	$5 \cdot 10^{-10}$	Y7
1000-2200	1470	$4 \cdot 10^{-10}$	Y8

TABLE 2.2: Background noise values for each frequency channel, the values are taken from the studies of Neubauer, Musmann, and Dehmel (1977).

values. For all the cases we have analyzed we found a good agreement with the BGN values suggested by Neubauer, Musmann, and Dehmel (1977).

In Table 2.2 we show the values of background noise for each channel in the y component of *HELIOS* 1.

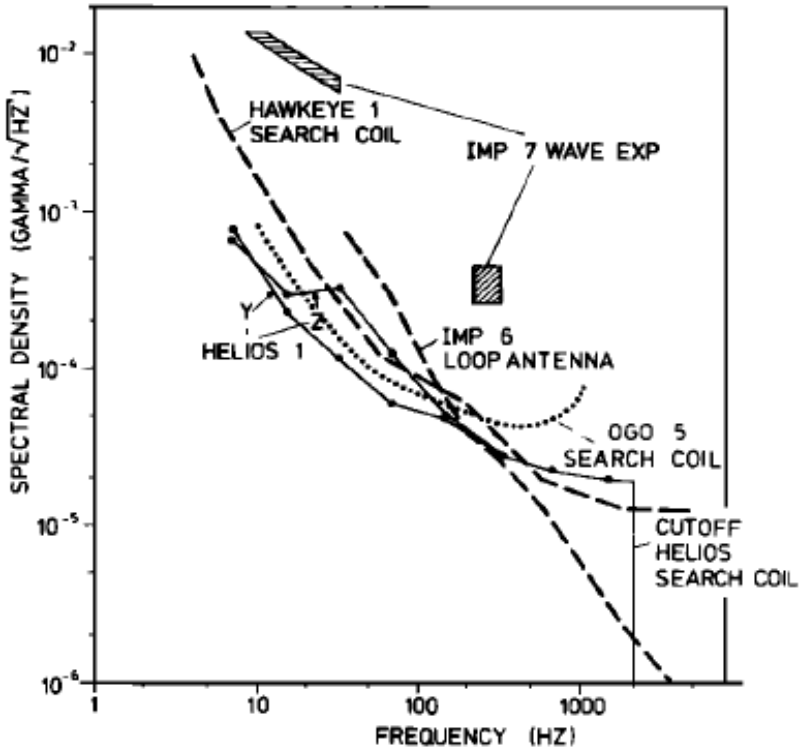

FIGURE 2.6: Helios-1 SCM Y and Z component background noise in comparison with different search coils on different missions. Figure taken from Neubauer, Musmann, and Dehmel (1977).

As we go closer to the Sun the temperatures increases, therefore it is important to know whether the instruments on board *HELIOS* were affected by the increasing temperatures. It has been suggested that all the channels of SCM showed healthy conditions till the end of 1977 in both the *HELIOS* missions (**Private communication Neubauer**).

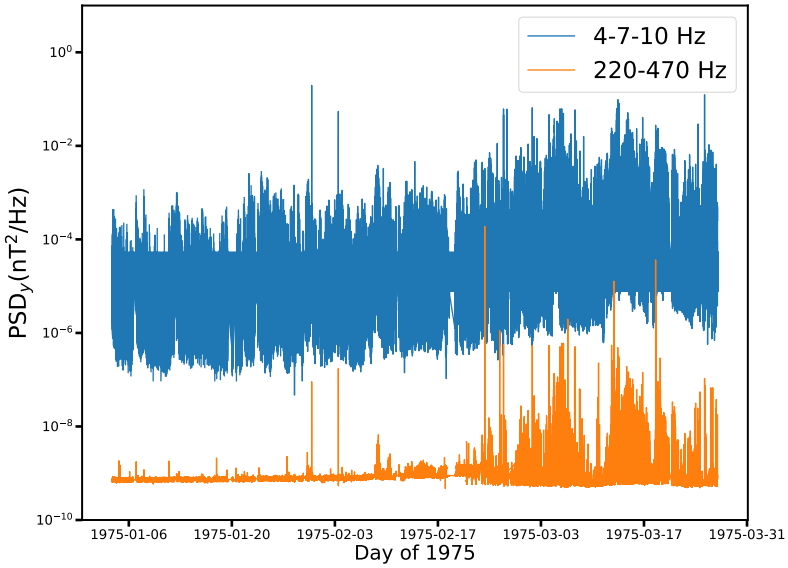

FIGURE 2.7: Mean PSD of the B_y component of the magnetic field from the SCM for two different frequency bands during the initial 3 months of 1975.

Depending on the operational mode of the spacecraft telemetry system, the time intervals in which the filtered outputs are squared and averaged by the onboard digital mean value computer are 1.125, 2.25, 4.5, 18, 36, 72, 144, 288, 576, 1152 seconds. For the same time interval, the peak value from each filter output is transmitted in addition to the mean value.

The mean and peak values are compressed to 8-sec averages when the average intervals used are less than 4.5 seconds. Most of the data available are of 8-sec averages. However, there are no clear indicators in the data files on the size of the averaging done, we cannot be sure whether the averaging has been done using the large intervals or if the data are missing. In our analysis, we consider the data to be missing when the gap between the data points is more than 8 sec.

The Mean and Peak power spectral density (PSD) values of two different frequency bands for the initial 3 months are shown in the Figure 2.7 and 2.8. At the start of the year *HELIOS* 1 was around 0.9 AU and by the mid-march, it was around 0.3 AU, we can observe the increase in the PSD values as we move closer to the Sun. Peak PSD values often showed the effect of saturation in all the bands, especially when *HELIOS* was approaching closer to the Sun, interestingly not in the pure fast wind, but in the slow wind. This might be due to the presence of some very high amplitude whistlers which exceeds the highest possible measuring capability of the instrument. As the presence of these large-amplitude whistlers in the fast wind is rare, which we will show in Chapter 5, we did not observe the problem of saturation in the fast wind.

While working with the *HELIOS* SCM data we have to be cautious, as there are few artefacts in the data, such as sudden non-physical dips in the mean, saturation of the peak values. Most of the nonphysical dips in the mean values were observed

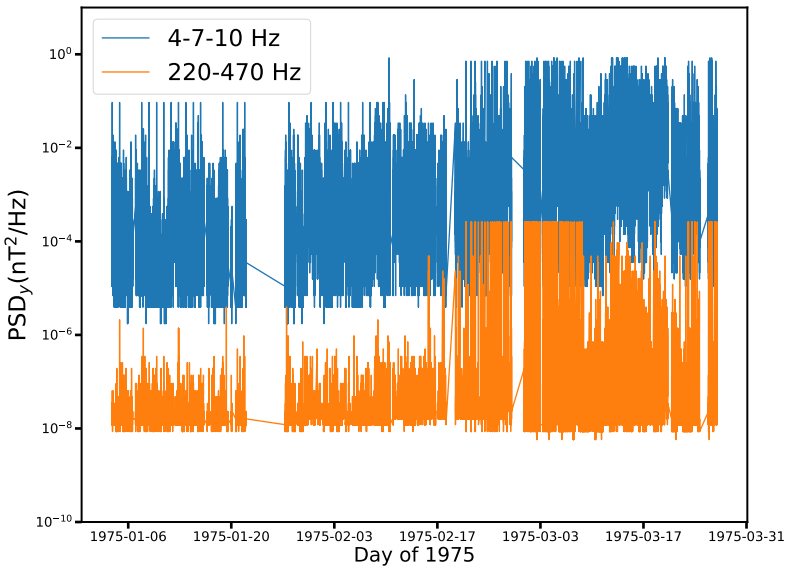

FIGURE 2.8: Peak PSD of the B_y component of the magnetic field from the SCM for two different frequency bands during the initial 3 months of 1975.

when the peak values were absent, these dips are well below the noise level of instrument. The reasons for the presence of the dips are not clear, but the saturation in the peak values might be mainly due to the limitations on the measuring range of each band. To remove some of the non-physical data, we have kept a constraint that we will work only with the data for which both the mean and peak spectral density values are available.

For our main analysis, we have always used mean spectral density values. We have not worked with the data which are a part of sudden dips (below the noise level). For the case of kinetic scale turbulence spectra analysis, we have not considered any mean spectral density intervals which showed saturation in peak values.

2.5 Résumé en français: La mission HELIOS

Ce travail s'appuie fortement sur les données de la mission HELIOS (1974-1985), qui fut la première à aller explorer l'héliosphère interne. Les deux satellites HELIOS 1 et 2 furent lancés respectivement le 10 décembre 1974 et le 15 janvier 1976. Leurs orbites différentes; en revanche, les deux satellites se sont approchés du Soleil jusqu'à une distance voisine de 0.29–0.3 u.a.

Chaque satellite HELIOS était équipé de divers instruments dont un magnétomètre de type fluxgate. HELIOS 1 était en outre équipé d'un magnétomètre de type search-coil. Dans ce chapitre nous décrivons succinctement le principe de fonctionnement de chacun des instruments. Le fluxgate mesure les trois composantes du champ magnétique avec une cadence maximale de 4 Hz. Il permet donc d'étudier le régime inertiel de la turbulence du vent solaire ainsi que les structures de plus grande échelle. Le search-coil de HELIOS 1 ne mesure que deux composantes (B_x et B_z ou B_y et B_z) des fluctuations du champ magnétique. Contrairement au capteur

fluxgate, qui fournit de séries temporelles, il délivre toutes les 8 secondes la densité de puissance spectrale dans 9 bandes spectrales: 4.7–10 Hz, 10–22 Hz, 22–47 Hz, 47–100 Hz, 100–220 Hz, 220–470 Hz, 470–1000 Hz et 1000–2200 Hz.

Les données des deux capteurs magnétiques sont hélas fragmentaires car une partie des archives a été perdue. Nous nous intéressons ici à celles de HELIOS 1 ont été mieux préservées. Les données du search-coil couvrent moins d'une année, ce qui équivaut à une orbite et demi. Celles du fluxgate couvrent plusieurs années et sont plus complètes. Notre connaissance de la dynamique du champ magnétique reste donc parcellaire. Néanmoins les observations de HELIOS 1 sont un témoin unique de l'héliosphère interne jusqu'à ce. Il aura fallu attendre 2018 avec le lancement de Parker Solar Probe pour détrôner HELIOS.

Un des aspects importants à prendre en compte avec ces instruments est leur niveau de bruit. Pour le magnétomètre de type fluxgate, les fluctuations observées dans le vent solaire sont généralement supérieures au seuil de bruit si bien qu'aucune précaution particulière n'est à prendre. En revanche, pour le magnétomètre de type search-coil, ce seuil est atteint vers 200 Hz. Au-delà de cette fréquence l'instrument ne peut plus mesurer correctement l'amplitude des fluctuations, sauf dans l'héliosphère interne, où elles sont plus grandes. Cependant, le search-coil délivre simultanément le spectre moyen et le spectre maximal; ce dernier apporte donc un complément d'information utile pour sonder les plus hautes fréquences.

Chapter 3

Turbulence from the injection scale to the dissipation scale

3.1 Introduction

The solar wind is an exceptional natural plasma laboratory for studying turbulence thanks to the possibility to measure *in situ* all key plasma parameters such as particle distributions, electromagnetic fields, temperatures, etc. (Bruno and Carbone, 2013b). Turbulence in neutral and in ionized fluids is generally considered as a disordered motion whose kinetic energy overcomes the damping that is caused by viscosity. This motion is inherently multi-scale in nature. In most situations the energy is injected into the system at large scales; from there a non-linear energy cascade occurs to smaller scales through the interaction of neighboring eddies until viscous forces prevail over inertial forces. Solar wind turbulence stands out by the ubiquitous presence of electromagnetic field fluctuations along with velocity fluctuations and its mostly non-collisional nature. The basic building blocks other than eddies or vortices are plasma waves, wave packets, and transients such as shocks.

The presence of a prevalent magnetic field breaks the isotropy that is usually observed in neutral fluid turbulence. In addition, the presence of a large number of characteristic scales, each of which can act as a channel for non-viscous dissipation, can strongly alter the microscopic and macroscopic properties of the turbulent wavefield (Alexandrova et al., 2012; Bruno and Carbone, 2013b; Verscharen, Klein, and Maruca, 2019). The large interest devoted to solar wind turbulence stems from its complex nature, and the role it plays in mediating the acceleration and heating in the solar wind (Tu and Marsch, 1997).

Since turbulence is inherently random in nature a statistical description is appropriate (Lumley, 1970; Frisch, 1995). Classical tools for investigating the properties of solar wind turbulence involve second and higher order moments such as structure functions. Additional insight into characteristic scales and their interplay is generally provided by spectral quantities such as the power spectral density (PSD) and higher order spectra. In this chapter, we shall focus on the PSD only, i.e. on second order moments. In doing so we will not be able to address quantities such as the rate of the turbulent energy cascade or phase couplings, which require the analysis of higher order moments that are much more demanding in terms of volume of data.

A detailed understanding of the evolution of turbulence in the solar wind requires the analysis of PSD of both the magnetic field and the velocity as these quantities contribute in different ways to the turbulent wavefield. In the following, however, we shall primarily focus on the PSD of magnetic field of the HELIOS mission between 0.3 and 1.0 AU and WIND mission at 1 AU. Therefore we will be missing information on the kinetic energy contribution. The main reason for focusing on the magnetic field only is the sparsity of velocity data from the HELIOS mission

and its low resolution. Magnetic field observations come with several additional advantages: independence with respect to the reference frame, availability of continuous measurements over a wide range of temporal scales (spanning from DC up to several tens of Hz) and relatively better immunity to spacecraft-generated noise (Borovsky et al., 1997).

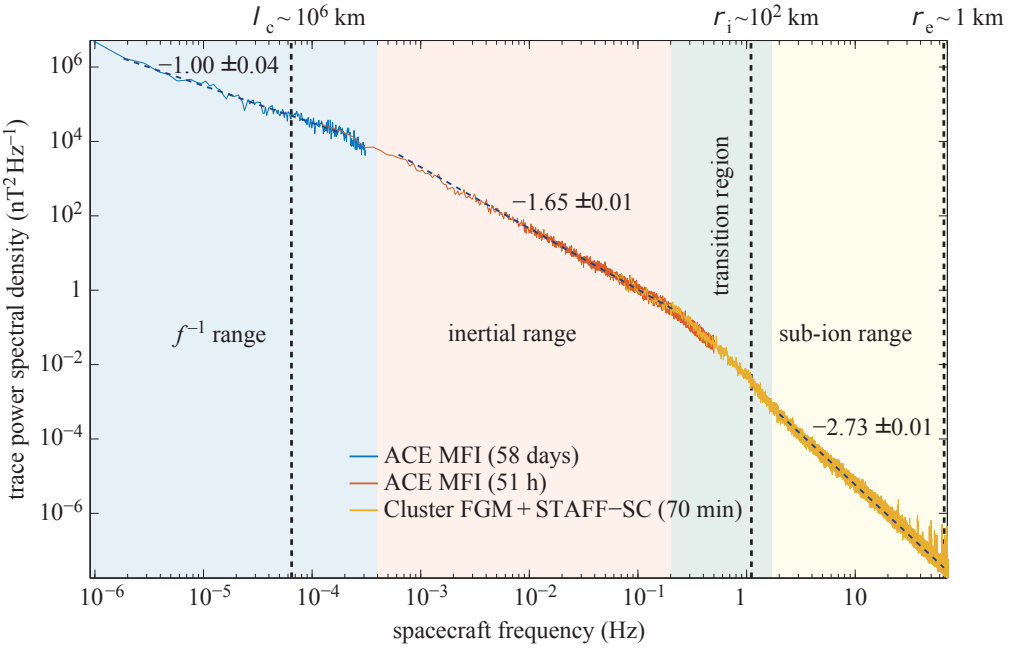

FIGURE 3.1: Power spectral density (trace of the spectral matrix) of the solar wind magnetic field measured at 1 AU by different spacecraft, taken from Kiyani, Osman, and Chapman (2015). This power spectral density covers a mix of slow and fast wind regimes.

Figure 3.1, which is taken from Kiyani, Osman, and Chapman (2015), presents the PSD of the solar wind magnetic field at 1 AU with a range of frequencies that span almost 8 decades. The log-log representation reveals the presence of several power laws, the slope and cutoff frequencies associated with these power laws carry the signature of the underlying physical processes. At large scales or low frequencies the PSD tends to follow a power-law with $PSD(f) \propto f^{\alpha}$ whose spectral index α approaches -1. The origin of this scaling is still unclear. Possible explanations involve uncorrelated coronal structures (Klein et al., 1992), Alfvénic fluctuations (Horbury, Forman, and Oughton, 2005) or the impact of compressibility (Matteini et al., 2018). This f^{-1} scaling can be considered as a reservoir on which the turbulent cascade then feeds on. Although the exact spectral index may somewhat deviate from -1, this regime is traditionally named f^{-1}

For solar wind turbulence at 1 AU, after the f^{-1} scaling, typically above 10^{-3} Hz we observe the presence of nearly $f^{-5/3}$ scaling that is also known as the inertial or Kolomogorov range, in which an MHD approximation may be used. This is the range in which energy cascades from large scales to smaller scales without any dissipation until the ion scales are encountered near 1 Hz. Kolmogorov-like spectra are commonly observed in the hydrodynamic turbulence; their appearance in highly non-collisional solar wind suggests that there is some universal property in the turbulent cascade.

In classical hydrodynamic turbulence, the $f^{-5/3}$ scaling occurs until collisional effects set in; the presence of dissipation then changes the spectral shape to a decaying exponential. In plasma turbulence, the presence of multiple characteristic time scales associated with ions and electrons alters this simple picture and introduces additional regimes. The associated frequency range is better known as the kinetic range. At these scales, the motion of each individual plasma particle becomes important, such as ion and electron gyroradius. There is a transition region from inertial to kinetic range, which is identified with a spectral break (Bourouaine et al., 2012; Bruno and Trenchi, 2014; Woodham et al., 2018). There is debate on what the spectral shape actually is in that range. Spectra are observed to steepen with a spectral index between -4 and -2 (Leamon et al., 1998; Smith et al., 2006; Chen et al., 2012; Roberts, Li, and Li, 2013). Among the reasons for this are the role of dissipation and the presence of the coherent structures (Smith, Vasquez, and Hollweg, 2012; Lion, Alexandrova, and Zaslavsky, 2016). The kinetic range starts with the sub-ion range, in which ions play a leading role. As we move towards higher frequencies electron effects start to dominate and another transition region sets in, which typically starts around electron Larmor frequency (Alexandrova et al., 2012; Sahraoui et al., 2013). In this range, the PSD departs from a power law and tends to follow an exponential shape (Alexandrova et al., 2009; Alexandrova et al., 2012) although the exact shape is still hotly debated (Sahraoui et al., 2013). In this particular range, whistler waves are routinely observed (Lacombe et al., 2014), which complicates the identification of the shape of the PSD. These whistler waves will be addressed in Chapter 5.

In the following, we shall address few important issues regarding the evolution of solar wind turbulence through the lens of the PSD of the magnetic field. First, we shall concentrate on large scales and determine whether we can observe the initiation of a non-linear cascade in the non-Alfvénic slow solar wind which was thought to be non-existent. For this, we investigate the presence of f^{-1} range, which gives us the evidence for the initiation of non-linear turbulence cascade. Next, we study the ratio of non-linear time to Alfvén time for both fast and slow solar wind at different scales and try to connect this ratio to the onset of the turbulence cascade, which should give insight into the physics of evolution of turbulence in the slow and fast winds.

After large scales, we move to the other end of the spectrum and consider the kinetic range. There are still many open questions regarding the nature of the dissipation mechanisms that operate in that range. We address this issue by investigating the possible spectral shape and the radial properties of the PSD in the kinetic range at 0.3 and 0.9 AU. Finally, we provide a complete picture of turbulence evolution from f^{-1} to the dissipation scale in the inner heliosphere at 0.3 and 0.9 AU for the fast solar wind case.

3.2 Data

To properly estimate the power spectral density (PSD) of the solar wind magnetic field we need long uninterrupted observations of the magnetic field. We start by considering scales in f^{-1} regime with frequencies that range between 10^{-5} and 10^{-4} Hz; these correspond to periods of days to several hours. To reduce the variance of the PSD estimates we need continuous measurements that are several times longer than the longest periods of interest (Press et al., 2002). For that reason, we seek continuous periods of several days. These are best found in observations made by satellites such as *WIND* at 1 AU. Note that continuity is not mandatory since the PSD

can also be estimated from irregularly sampled data. In the following, however, we shall not consider such methods.

WIND is a NASA science spacecraft that was launched in November 1994 and has been positioned in a halo orbit around the L1 Lagrange point since 2004. The spacecraft has been constantly observing the solar wind in the ecliptic plane, at a constant distance of 1 AU from the Sun and therefore provides unprecedented long and uninterrupted records of the solar wind. We consider the period from 2004 to 2016 with magnetic field measurements made by the fluxgate magnetometer (Lepping et al., 1995) and proton densities made by the solar wind experiment (Ogilvie et al., 1995).

HELIOS 1 does not offer such long records of the magnetic field. However, it allows us to investigate the radial evolution between 0.3 and 1 AU. We use waveforms of the magnetic field as measured by the fluxgate magnetometer (Musmann et al., 1975) and PSDs of the AC magnetic field fluctuations from the search-coil (Dehmel et al., 1975). Most of these measurements were made in 1975 with a sampling period of 0.25 seconds for the fluxgate magnetometer and 8 seconds for the search-coil. The working principle of these instruments is explained in the Chapter 2.

The fluxgate magnetometers of *WIND* and *HELIOS* measure three components of the magnetic field so that we can estimate the total PSD or trace of the spectral matrix, which is the sum of the PSDs of all three components. The search-coil of *HELIOS* 1 directly produces spectral densities in 8 logarithmically-spaced frequency bins, see Chapter 2. Although this instrument simultaneously measures up to two components of the magnetic field, we concentrate on the B_y component only because it is less affected by stray magnetic fields (Neubauer, Musmann, and Dehmel, 1977). As in (Alexandrova et al., 2012) we distinguish physically meaningful values from instrument noise by selecting PSDs whose values exceed by three times the background noise level that is provided by Neubauer, Musmann, and Dehmel (1977). With this restriction, we guarantee that the observed values are not significantly affected by instrument noise.

Note that all records have occasional data gaps that rarely last for more than a few seconds but still disrupt the continuity. We linearly interpolated these gaps, following the recommendation by Munteanu et al. (2016), who has shown that this has a limited impact on the PSD, especially at low frequencies.

In what follows we shall routinely divide the solar wind into two types: slow ($v < 400$ km/s) and fast ($v > 600$ km/s) wind and analyze separately the magnetic field.

3.3 f^{-1} in the slow wind

Early evidence for the presence of a power-law with a f^{-1} scaling in the PSD of magnetic field fluctuations can be found in Mariner 2, Mariner 4, and OGO 5 data at 1 AU (Russell, 1972). Denskat and Neubauer (1982) later found a similar scaling in magnetic field data from *HELIOS* 1. In particular, they observed this scaling much closer to the Sun, at 0.3 AU. Bavassano et al. (1982) improved that study by considering only fast wind streams. Matthaeus and Goldstein (1986) arguably were the first to have investigated in detail the nature and origin of this $1/f$ scaling. However, they considered long records that spanned hundreds of days and therefore mixed slow and fast winds. Such mixtures cannot give us a complete picture because the properties of turbulence are different for slow and fast winds, as are the sources of solar wind fluctuations.

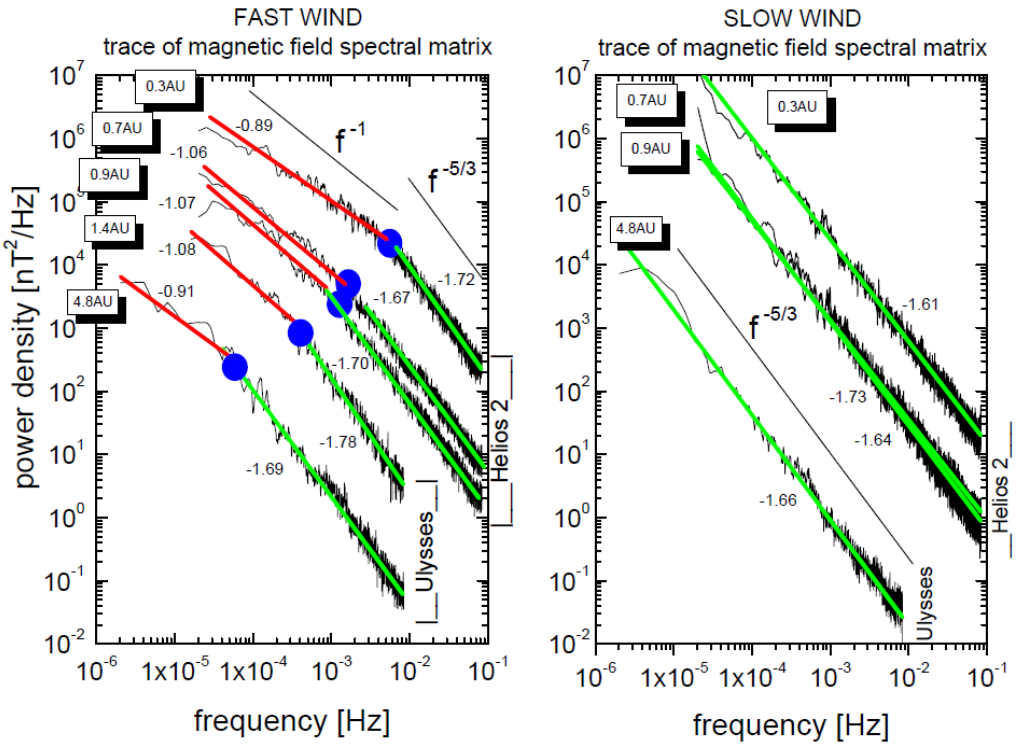

FIGURE 3.2: Low frequency spectra of the magnetic field observed in the slow and fast solar wind from 0.3 to 4.8 AU. Figure taken from Bruno and Carbone (2013b).

Until recently, it was widely believed that the f^{-1} regime could be observed only in the fast solar wind (with solar wind velocities $v > 600$ km/s) or slow alfvénic winds but not in non-Alfvénic slow winds ($v < 400$ km/s). This current understanding is illustrated in the Figure 3.2 by Bruno and Carbone (2013b). In this Figure, the authors show the presence of a gradual transition between inertial and f^{-1} regime for the fast wind only.

Why is it so important to locate the onset of the f^{-1} regime as we move from the inertial range towards lower frequencies? This transition tells us at what characteristic time scale the non-linear energy cascade of the inertial range is actually beginning. Therefore, a radial scan of this time scale should then give us valuable information on the physical processes at play and an opportunity to understand the basic differences in the evolution of turbulence in the slow and fast wind if there are any.

Motivated by this conspicuous absence of an f^{-1} regime in the non-Alfvénic slow wind, let us now investigate in more detail the slow non-Alfvénic wind.

3.3.1 Slow wind at 1 AU

Below 1 AU, the solar wind rarely remains slow or fast for more than a few days in a row, which severely limits the lowest frequency that one can access in the PSD. Indeed, in standard Fourier analysis, the lowest nonzero frequency is given by $f_{min} = 1/T$, where T is the duration of the interval. Parametric PSD estimators could potentially give access to lower frequencies (Priestley, 1988) but have not yet

been tested for such data. In this context, the long and uninterrupted observations made by WIND at 1 AU are a boon as it becomes technically possible to investigate frequencies as low as a few 10^{-6} Hz.

Our recent study on stationarity in the solar wind (Krishna Jagarlamudi et al., 2019) probably was the first to reveal near 10^{-4} Hz in the slow wind a transition to what could be interpreted as f^{-1} regime. However, more recently, and independently, Bruno, R. et al. (2019) has carried out a detailed analysis of this transition, showing the presence of f^{-1} in the slow non-Alfvénic wind.

Let us now focus on the existence of this transition in non-Alfvénic slow wind intervals and therefore concentrate on time intervals whose dimensionless cross helicity is low. We define the dimensionless cross helicity as (Wicks et al., 2013)

$$\sigma_c = \frac{2\delta\mathbf{b}\cdot\delta\mathbf{v}}{|\delta\mathbf{b}|^2 + |\delta\mathbf{v}|^2} \tag{3.1}$$

Here, $\delta\mathbf{b}$ stands for the Alfvén normalized magnetic field fluctuation and is defined as

$$\delta\mathbf{b} = \frac{\delta\mathbf{B}}{\sqrt{\mu_0\rho_0}} \tag{3.2}$$

and $\delta\mathbf{v}$ stands for the velocity fluctuation. $\delta\mathbf{B} = \mathbf{B} - \langle\mathbf{B}\rangle$, $\delta\mathbf{V} = \mathbf{V} - \langle\mathbf{V}\rangle$. Fluctuations are considered as non-Alfvénic when σ_c is small. In the following we look for values $\sigma_c < 0.5$.

In the data from WIND We found 11 intervals of slow solar wind that have velocities < 400 km/s and are at least 11 days long. Although these 11 intervals are devoid of large interplanetary shocks and stream interaction regions, they still should be considered as a mix of the slow solar wind with some large-scale structures. We calculate the dimensionless cross helicity σ_c for each of these intervals in the following way: first, we decimate the magnetic field measurements to the 60 s cadence of the velocity. We then compute the value of σ_c over 4-hour windows and subsequently calculate the absolute average of all values obtained for the continuous interval of interest to obtain the cross helicity. The dispersion of these values gives us an indication of the uncertainty on this average.

Out of our 11 intervals we find 9 whose normalized cross helicity satisfies the criterion $\sigma_c \leq 0.5$, see Table 3.1. These are the ones we label in the following as non-Alfvénic slow solar wind even though the large uncertainties on σ_c prohibit us from separating the regimes in a more decisive way.

One example of an interval with non-Alfvénic slow solar wind is shown in Figure 3.3 with its different plasma parameters. For each of these intervals, we have estimated the PSD of the three components of the magnetic field by using Welch's periodogram method (Press et al., 2002). This remains the most commonly used method for estimating PSDs although the discrete wavelet transform has been shown to provide better estimates of spectral indices when the fluctuations are self-similar, i.e. when the PSD follows a power-law over a given frequency range (Abry, Goncalves, and Flandrin, 1995). In Welch's method, the records are first divided into N different segments that overlap by 50%; we then apply to each of them a Hanning window, compute the Fourier transform, and average the squared magnitude of the latter.

	n_p (cm^{-3})	V_{SW} (km/s)	**B** (nT)	σ_c	$\approx T_{exp}(hr)$
1	8.0 ± 2.5	321 ± 23	3.3 ± 1.2	0.35 ± 0.21	129.5
2	7.4 ± 2.0	325 ± 29	4.2 ± 1.2	0.47 ± 0.23	128
3*	6.3 ± 2.6	324 ± 23	3.8 ± 1.3	0.53 ± 0.23	128
4	7.6 ± 5.9	324 ± 21	3.7 ± 1.8	0.39 ± 0.21	128
5	7.8 ± 4.1	322 ± 34	4.1 ± 2.3	0.30 ± 0.19	129
6	7.6 ± 4.2	341 ± 18	5.8 ± 2.2	0.43 ± 0.22	122
7*	5.6 ± 3.9	329 ± 29	4.1 ± 1.2	0.63 ± 0.17	126
8	7.5 ± 3.1	323 ± 22	4.2 ± 1.3	0.42 ± 0.24	129
9	6.0 ± 3.7	315 ± 26	4.6 ± 1.8	0.48 ± 0.26	132
10	8.9 ± 4.1	326 ± 21	5.5 ± 2.1	0.43 ± 0.22	127.5
11	7.8 ± 3.9	330 ± 19	4.4 ± 1.7	0.45 ± 0.22	126

TABLE 3.1: Key plasma parameters with the proton number density (n_p), the bulk flow velocity (V_{SW}), the total magnetic field (**B**), the normalized cross helicity (σ_c) and the expansion time (T_{exp}) related to the non-Alfvénic slow wind intervals analyzed. The quantities shown are averages of the whole time interval, with their dispersion. The two intervals that do not meet our criterion for non-alfvénicity are indicated with a *.

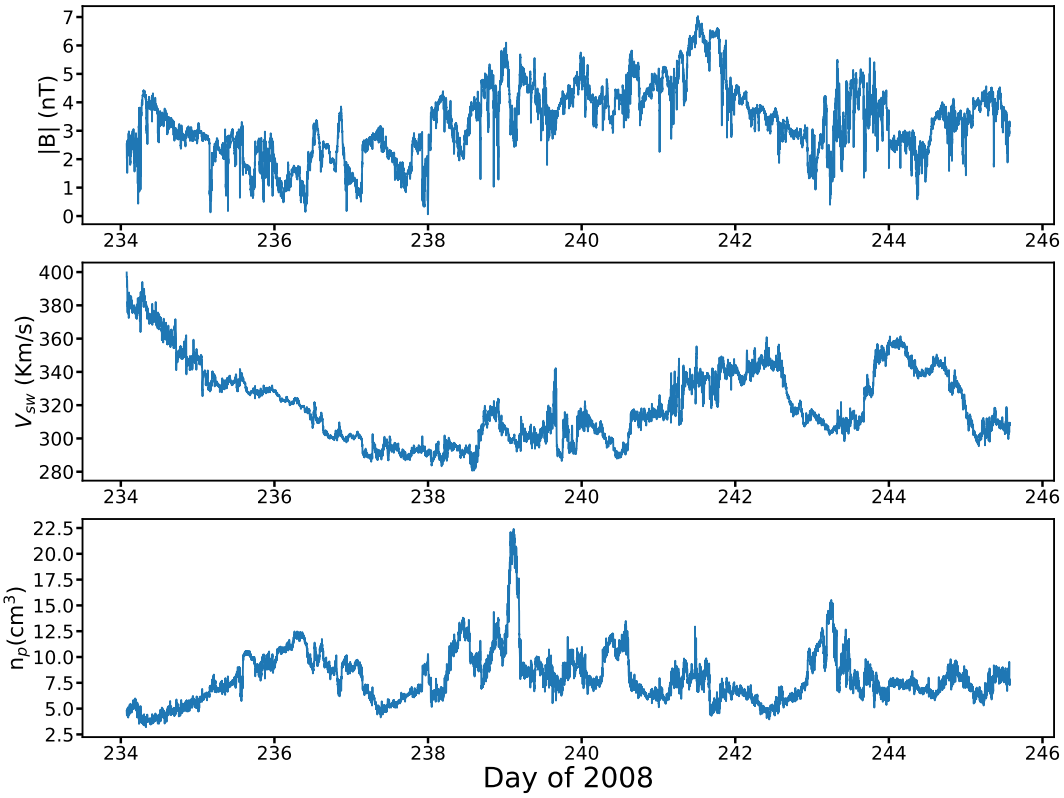

FIGURE 3.3: Total magnetic field, speed and proton density for a non-Alfvénic slow wind interval in 2008 (at solar minimum).

Interestingly, all intervals show evidence for a flattening of the PSD at low frequencies. To identify at what frequency the spectral index changes we use compensated spectra (Matthaeus and Goldstein, 1986; Dudok de Wit et al., 2013), where

	α $(1/f^{\alpha})$	β $(1/f^{\beta})$	f_b(Hz)
1	1.06 ± 0.28	1.76 ± 0.04	$10^{-4} \pm 20\%$
2	1.26 ± 0.33	1.73 ± 0.04	$10^{-4} \pm 20\%$
3	0.94 ± 0.36	1.71 ± 0.04	$10^{-4} \pm 20\%$
4	1.03 ± 0.28	1.77 ± 0.07	$10^{-4} \pm 20\%$
5	NA	1.77 ± 0.05	NA
6	1.31 ± 0.15	1.73 ± 0.03	$8 \times 10^{-5} \pm 20\%$
7	1.23 ± 0.26	1.72 ± 0.06	$2 \times 10^{-4} \pm 20\%$
8	1.25 ± 0.28	1.73 ± 0.07	$1.5 \times 10^{-4} \pm 20\%$
9	1.20 ± 0.26	1.73 ± 0.06	$8 \times 10^{-5} \pm 20\%$
10	NA	1.77 ± 0.06	NA
11	1.26 ± 0.21	1.71 ± 0.05	$10^{-4} \pm 20\%$

TABLE 3.2: Spectral index values for the power law spectral fits made and frequency of spectral break (f_b) for the non-Alfvénic slow wind intervals analyzed. Intervals for which the break frequency cannot be meaningfully estimated are indicated as NA.

we multiply the observed spectrum by the inverse of the expected law: if the spectrum follows a $PSD(f) \propto f^{-1}$ power-law then the compensation by f^{+1} function leads to a constant PSD in the f^{-1} range. From this, we can identify more easily the break frequencies by locating the frequencies at which the PSD starts departing from this constant value. This recipe provides us with a simple means for guessing the uncertainties associated with these break frequencies. A proper assessment of the different uncertainties is much more involving (e.g. Clauset, Rohilla Shalizi, and Newman, 2009), which explains why most studies completely ignore that crucial aspect of inference.

An illustration of the spectral break identification is given in Figure 3.4. In practice, we rarely observe a clear transition from inertial to f^{-1} regime. In most cases, the flattening of the PSD is gradual with a spectral index approaching -1 at the lowermost frequencies. For that reason, we compensate the PSD with different scalings that range from $f^{0.8}$ to $f^{1.3}$. If we do not find evidence for a power law to cover a least one decade then we disqualify the record. If, on the other hand, the compensation leads to a satisfactory result, then we refine the estimation of the break frequency and the spectral index. The latter is estimated by non-linear curve fitting.

Two examples of PSDs with a break are shown in Figures 3.5 and 3.6 respectively for solar minimum and for solar maximum conditions. The blue line is the averaged PSD calculated over different windows in the interval and the black line represents the best fit. In place of the uncertainty of the PSD we consider the dispersion of the PSDs from different windows. That is, we consider the standard deviation of the PSDs estimated from the same time-interval as an approximation of its uncertainty.

Finally, in Table 3.2 we present the spectral indices estimated for the f^{-1} range and for the inertial range. Also shown is the break frequency f_b (when meaningful). The value of the spectral index in the inertial range is well constrained by the easy identification of the latter and is compatible with the -5/3 value that is routinely found at 1 AU. Note that the two intervals for which we are unable to detect a f^{-1} range (numbers 5 and 11) are not the ones that have relatively higher alfvénicity in Table 3.1 (number 3 and 7).

For comparison we also show PSDs obtained in the fast wind and in a highly Alfvénic slow wind, see respectively Figures 3.7 and 3.8. Notice that the spectral

break in the fast wind is nearly 1 decade away from the one observed in the non-Alfvénic slow wind; the spectral break of the Alfvénic slow wind is located between the non-Alfvénic slow wind and the fast wind. We observe the same behaviour in the majority of the analyzed intervals.

At this stage, we can already conclude that the spectral break between inertial and f^{-1} regimes is not just a function of the solar wind expansion (i.e. velocity) or cross helicity. If there were a dependence only on the expansion time (T_{exp}) then we would expect the spectral break of the Alfvénic slow and non-Alfvénic slow wind to be co-located in frequency. However, this conclusion might not be fully true as for the expansion time (T_{exp}) calculations we have not considered the lateral effects, so we do not know how much over or under expanded the stream is. If the cross helicity were the leading factor then the spectral break should be the same for highly Alfvénic slow wind and fast wind. Therefore, we have to consider other factors.

First of all to meaningfully compare different observations we need to guarantee that the conditions of the solar wind are similar. For that reason, we decompose our intervals into those observed near solar maximum (when Alfvénic slow winds are more frequent) and near solar minimum. Figure 3.9 compares the PSDs estimated for some of these intervals. Notice that above a frequency of approximately $5 \cdot 10^{-3}$ Hz, the PSDs associated with different conditions are well separated. Fast winds show higher amplitudes than slow Alfvénic winds, and Alfvénic slow winds show higher amplitudes than non-Alfvénic slow winds. In some other cases (not shown here) the amplitudes are comparable for the Alfvénic and non-Alfvénic slow winds.

However, as we proceed to lower frequencies we find that the amplitude of slow wind fluctuations could be nearly equal to that of fast wind fluctuations, see Figure 3.9. This result shows that as expected the amplitudes of fast wind fluctuations are larger than the slow wind fluctuations in the usually analyzed scales ($< 10^{-5}$ Hz) in the solar wind at 1 AU. However, from our analysis, we also understood that as we reach the large scale fluctuations, the amplitude of slow wind fluctuations could be nearly equal to the fast wind fluctuations and some times higher. This contradicts the standard belief that fast wind fluctuations should always be larger than slow wind fluctuations. However, this trend was not always observed at 1 AU and when we are closer to the Sun ($\approx$ 0.3 AU), the slow and fast wind intervals are clearly separated, which we will see in the coming section.

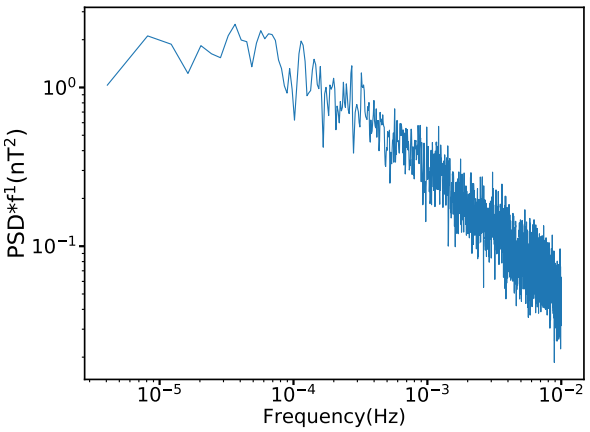

FIGURE 3.4: PSD$\times f^1$ as a function of the frequency of the magnetic field for a non-Alfvénic slow wind interval in 2008 (at solar minimum), days 234-245.

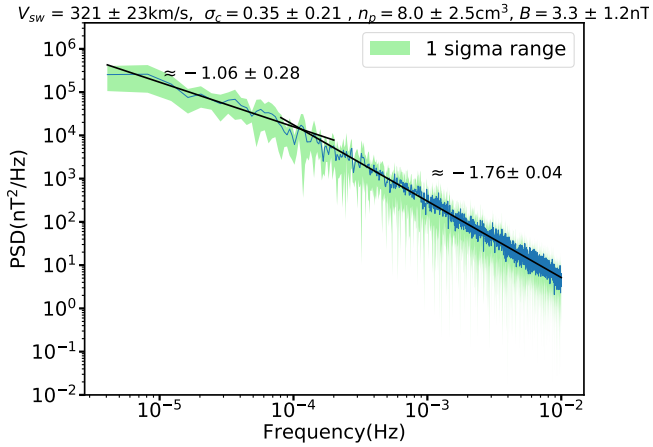

FIGURE 3.5: PSD of the magnetic field for a non-Alfvénic slow wind interval in 2008 (at solar minimum), days 234-245. The trace of the spectral matrix is shown. The mean values of the plasma conditions of the whole analyzed interval are presented at the top of the Figure.

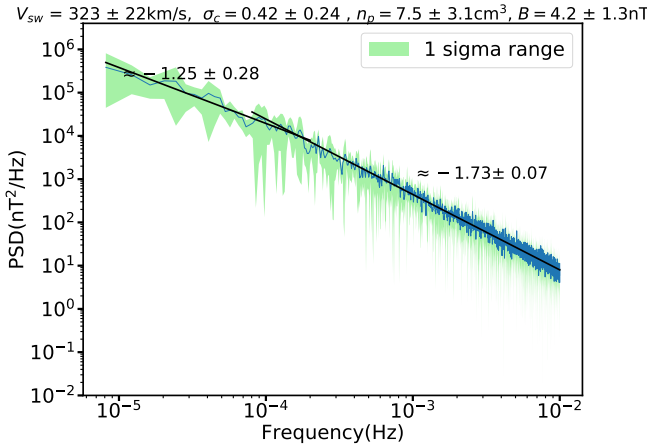

FIGURE 3.6: PSD of the magnetic field for non-Alfvénic slow wind interval from the year 2013 (Solar Maximum), first 11 days of the year. The trace of the spectral matrix is shown. The mean values of the plasma conditions of the whole analyzed interval are presented at the top of the Figure.

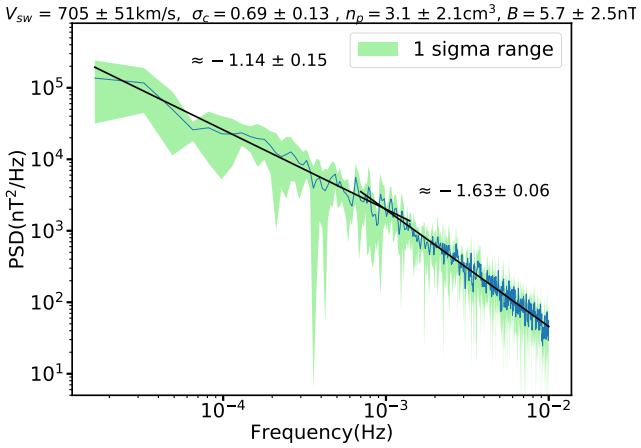

FIGURE 3.7: PSD of the magnetic field for fast wind interval from the year 2015 (Solar Maximum), days 280-282. The trace of the spectral matrix is shown. The mean values of the plasma conditions of the whole analyzed interval are presented at the top of the Figure.

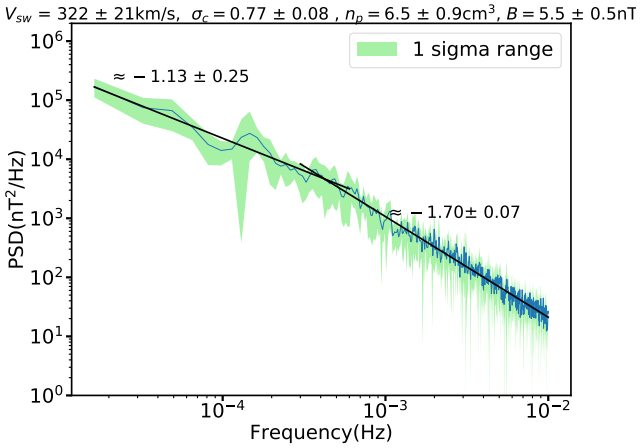

FIGURE 3.8: PSD of the magnetic field for Alfvénic slow wind interval from the year 2015 (Solar Maxima), day 16-19. The trace of the spectral matrix is shown. The mean values of the plasma conditions of the whole analyzed interval are presented at the top of the Figure.

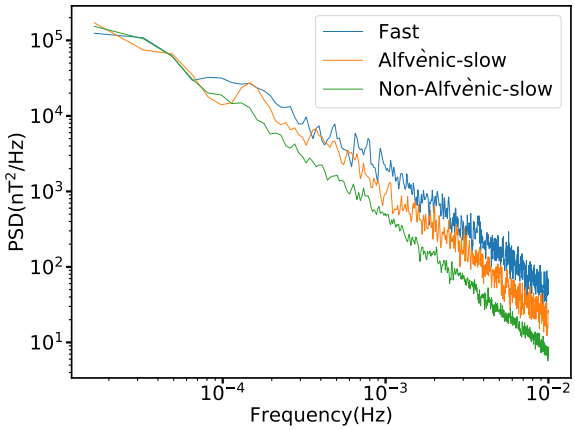

FIGURE 3.9: PSD of the magnetic field in fast, Alfvénic slow and non-Alfvénic slow wind intervals. The trace of the spectral matrix is shown. The mean values of the plasma conditions of the whole analyzed interval are presented at the top of the Figure.

At this stage we can summarize our main findings as such:

- The existence of a f^{-1} regime in 8 of the 11 analyzed intervals with pure slow solar wind;
- The spectral break between inertial and f^{-1} regimes is located at $7 \cdot 10^{-5} - 10^{-4}$ Hz for most of the non-Alfvénic slow wind intervals;
- There is at least 1-decade difference between the spectral break observed in fast and in slow solar winds;
- The location of the spectral break for slow, fast and Alfvénic slow winds is not controlled by the expansion time only;

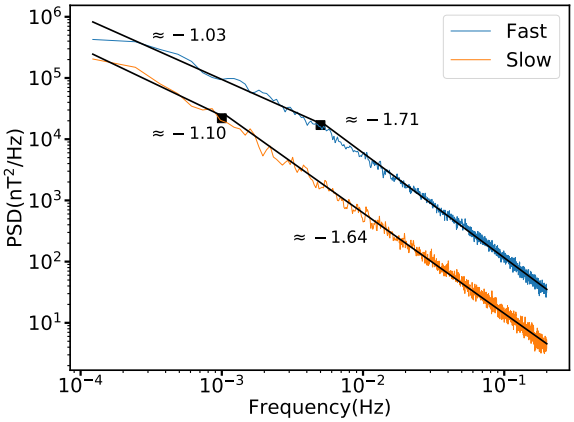

FIGURE 3.10: PSD of the magnetic field in a slow (Days 66.4-67.6) and fast (Days 72.1-74.5) solar wind at 0.3 AU. The trace of the spectral matrix is shown and the numbers refer to the spectral indices.

- The fluctuation level is higher in the fast solar wind, except at very low frequencies ($< 10^{-4}$ Hz), where slow wind fluctuations can some times be comparable.

Let us now investigate how these results evolve as we move inside the heliosphere.

3.3.2 Slow wind in the inner-heliosphere

As mentioned before, the *HELIOS* mission provides a unique opportunity to study the radial evolution of turbulence in the inner heliosphere, from 0.3 to 1 AU. Unfortunately, the time series of the magnetic field from *HELIOS* 1 suffers from many data gaps. These are mainly caused by lost or by corrupted data. In addition, the transition between solar wind regimes occurs at a faster pace when moving closer to the Sun. For that reason, it is much more difficult to collect long uninterrupted intervals of pure slow or fast solar wind in the inner heliosphere than at 1 AU.

In spite of these limitations, we did find some examples that exhibit a spectral break, both in the fast and in the slow solar wind, see Figure 3.10. These observations were made near perihelion, i.e. at a radial distance of 0.3 AU. Even though the slow wind interval is found to be highly Alfvénic ($\sigma_c \approx 0.8$) and thus comparable to a fast wind interval, this is arguably the first direct evidence for a f^{-1} regime in the slow wind at 0.3 AU. Notice that there is nearly one decade difference between the spectral breaks and that the fluctuation level is lower in the slow than in the fast wind.

Let us now investigate whether there is some common physical parameter that governs the f^{-1} spectral breaks observed in different solar wind conditions. Answering this question begins with the determination of the non-linear time that marks the onset of the turbulent cascade.

3.3.3 Non-linear time estimations and the connection between the spectral break in the fast and slow solar wind

The non-linear time or eddy turnover time (T_{nl}) is an important quantity in turbulence as it characterizes the energy injection process. One may consider it as the time it takes for the energy transfer to happen from a large scale to a smaller scale without significant energy dissipation. This quantity does not have a unique value but rather a continuum spectrum of values depending on the size of the turbulent eddies. We shall start by estimating the non-linear time at different scales and then compare it to the observed spectral break.

In hydrodynamic turbulence, the non-linear time is routinely defined as $T_{nl} = \lambda/\delta v$, where λ is the size of the eddy and δv is the velocity fluctuation of the corresponding eddy (Frisch, 1995). However, in the solar wind, the presence of magnetic field fluctuations enter and alters this picture. One may reasonably assume the MHD approximation to hold in the inertial range of the solar wind. In this case, studies by Zhou, Matthaeus, and Dmitruk (2004) and Matthaeus et al. (2014) shows that the extension of T_{nl} from hydrodynamic to MHD gives

$$T_{nl} = \lambda/Z, \tag{3.3}$$

where the velocity fluctuation is replaced by Z; $Z^2 = \delta u^2 + \delta b^2$ is the total energy per unit mass. Here, δu and δb are the rms fluctuations levels of the velocity and magnetic fields. The latter is expressed in Alfvénic speed units

$$\delta b = \frac{\delta B}{\sqrt{\mu_0 \rho_0}}. \tag{3.4}$$

The eddy size λ can be estimated by knowing the solar wind velocity (V_{sw}) and the frequency (f) of the scale we are interested in, $\lambda = V_{sw}/f$.

We estimate RMS fluctuations of the velocity and magnetic fields from the power spectral density (PSD) values at that same frequency. In practice, we first convert the time series of the magnetic field into Alfvénic units by using Equation 3.4 and then estimate the PSD. If $E_b(f)$ is the PSD of the magnetic field at frequency f (or, equivalently, at wave-number k), then $\delta b^2 = E_b(f) * f$ or $\delta b^2 = E_b(k) * k$ (Tu and Marsch, 1995a; Zhou, Matthaeus, and Dmitruk, 2004).

A general assumption in most studies to date is that RMS fluctuations in velocity and magnetic field are comparable (Zhou, Matthaeus, and Dmitruk, 2004; Matthaeus et al., 2014). Another motivation for this assumption is the frequent lack of velocity data or the unavailability of high-resolution velocity data. Let us therefore assume too that $E_v = E_b$ and proceed further. If E_b is the PSD at a certain frequency in the inertial range, then

$$Z = \sqrt{2 f E_b(f)}. \tag{3.5}$$

Now the non-linear time is given by

$$T_{nl} = V_{sw}/f\sqrt{2 f E_b(f)} \tag{3.6}$$

Equation 3.6 provides a approximate non-linear time, assuming an isotropic MHD scenario. However, we caution the reader that this is just a rough estimate and stress that the results of this analysis should be considered with care. The isotropic MHD case is a valid assumption for the large scales (lower frequencies) which are close to and below the spectral break frequency which we are interested in. The reason is

	$f_b(Hz)$	$\frac{\delta B}{B}$ @ f_b	T_{nl} (h)	T_A (h)	T_{nl}/T_A
1	$10^{-4} \pm 20\%$	0.40 ± 0.04	61.6 ± 18.4	34.6 ± 7.1	1.77 ± 0.25
2	$10^{-4} \pm 20\%$	0.33 ± 0.03	57.1 ± 17.5	26.8 ± 5.4	2.13 ± 0.30
3	$10^{-4} \pm 20\%$	0.38 ± 0.03	51.6 ± 15.4	27.4 ± 5.3	1.88 ± 0.28
4	$10^{-4} \pm 20\%$	0.41 ± 0.04	54.2 ± 16.1	31.2 ± 6.2	1.74 ± 0.26
5	NA	NA	NA	NA	NA
6	$8 \times 10^{-5} \pm 20\%$	0.32 ± 0.04	56.0 ± 21.0	26 ± 6.4	2.17 ± 0.35
7	$2 \times 10^{-4} \pm 20\%$	0.26 ± 0.02	32.9 ± 5.0	12.2 ± 1.2	2.7 ± 0.16
8	$1.5 \times 10^{-4} \pm 20\%$	0.32 ± 0.02	39.3 ± 7.7	17.8 ± 2.4	2.21 ± 0.2
9	$8 \times 10^{-5} \pm 20\%$	0.30 ± 0.04	63.2 ± 23.2	26.5 ± 6.6	2.38 ± 0.37
10	NA	NA	NA	NA	NA
11	$10^{-4} \pm 20\%$	0.37 ± 0.04	50.2 ± 15.1	26.5 ± 5.2	1.90 ± 0.28

TABLE 3.3: Frequency of spectral break (f_b), normalized fluctuation $\frac{\delta B}{B}$ at the break frequency, non-linear time T_{nl} at the initiation of the break, the Alfvén time T_A and the ratio T_{nl}/T_A for the non-Alfvénic slow wind intervals analyzed. Intervals for which the break frequency cannot be meaningfully estimated are indicated as NA.

that as we go towards the lower and lower frequencies the ratio $\frac{\delta B}{B}$ becomes large (Matteini et al., 2018; Bruno, R. et al., 2019) and tends to 1 (Matteini et al., 2018). As $\frac{\delta B}{B}$ becomes large, δB and B are comparable and we do not have anisotropy anymore. Indeed, observations show that in the 1/f regime the PSD is comparable along and perpendicularly to the mean magnetic field, whereas in the inertial range they are different (Wicks et al., 2010). Therefore, T_{nl} calculated assuming an isotropic MHD case is valid in the f^{-1} range and close it. However as we go towards the smaller and smaller scales in the inertial range our isotropic assumption does not hold anymore.

The question now arises: Is the slow wind spectral break present where it is expected to be observed and is the physics of the evolution of turbulence governed by similar mechanisms in the slow and fast solar winds? To answer this we compare the non-linear time to the Alfvén time, which is defined as

$$T_A = \lambda / V_A, \tag{3.7}$$

where V_A is the Alfvén speed. At the spectral break, the ratio T_{nl}/T_A can be interpreted as the number of Alfvénic collisions needed for the non-linear cascade to begin. If this ratio is nearly the same, then one may expect that the same physical reasoning leads to the location of the spectral break between the 1/f range and the inertial range, regardless of whether the wind is fast or slow.

We have estimated this ratio at different scales for the different intervals that were mentioned above. Some of the results obtained at 1 AU are illustrated in Figure 3.11. We show two cases of non-Alfvénic slow wind (corresponding to solar minimum and to solar maximum): one case with a fast wind and one case with an Alfvénic slow wind. The analyzed intervals are the same as those shown in Section 3.3. A striking feature that is common to all intervals is the saturation of the ratio T_{nl}/T_A below a given frequency, with a saturation value of approximately 2 that is nearly the same for all solar wind conditions. The onset of this saturation coincides with the spectral break between the f^{-1} range and the inertial range. The value of T_{nl}/T_A at the spectral break for all the non-Alfvénic slow wind analyzed is provided in Table 3.3 and all the values are around 2.

We observe the same saturation of the T_{nl}/T_A ratio in the inner heliosphere once

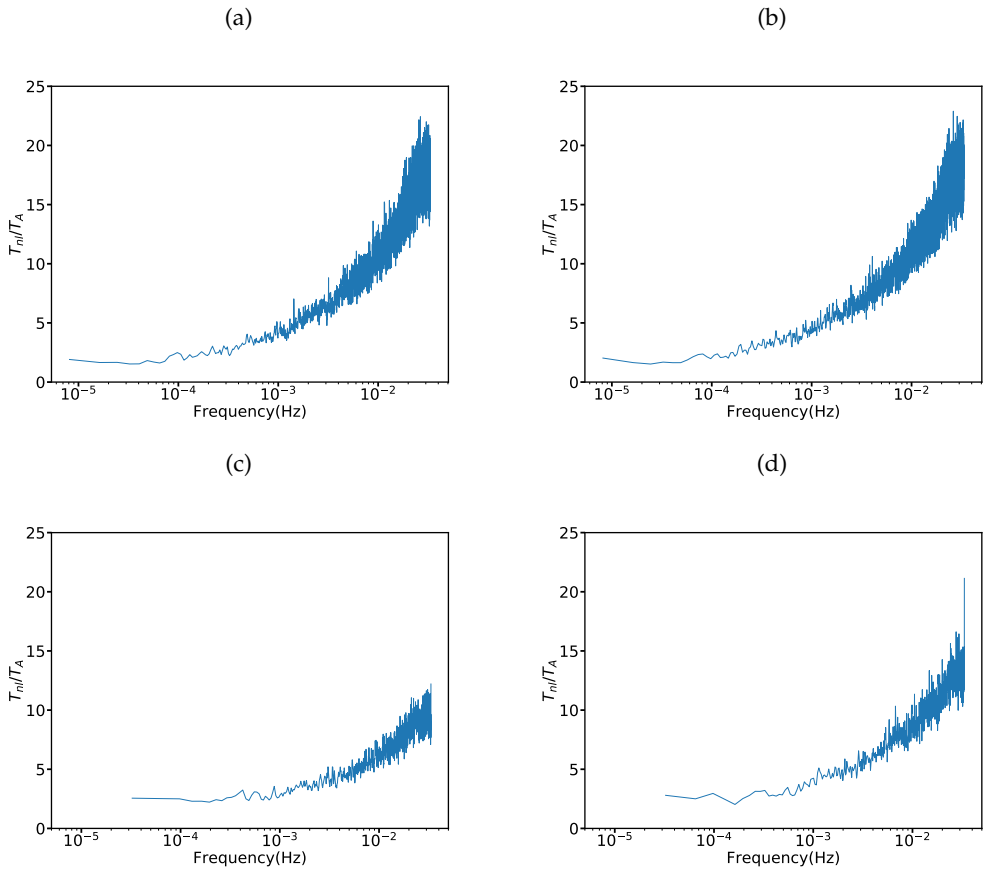

FIGURE 3.11: Ratio of non-linear time to Alfvén time for 4 different intervals: (a) non-Alfvénic slow wind (solar minimum), 2008 days 234-245 ; (b) non-Alfvénic slow wind (solar maximum), 2013 first 11 days; (c) Fast wind (solar maximum), 2015 days 280-282; and, (d) Alfvénic slow wind (solar maximum), 2015 days 16-19.

the frequency of the spectral break is hit. Figure 3.12 shows two examples of that ratio for fast and Alfvénic slow wind at 0.3 AU. Interestingly, for the fast wind, this ratio does not change with the distance from the Sun. For the Alfvénic slow wind, the saturation value is approximately twice the value found at 1 AU.

(a)

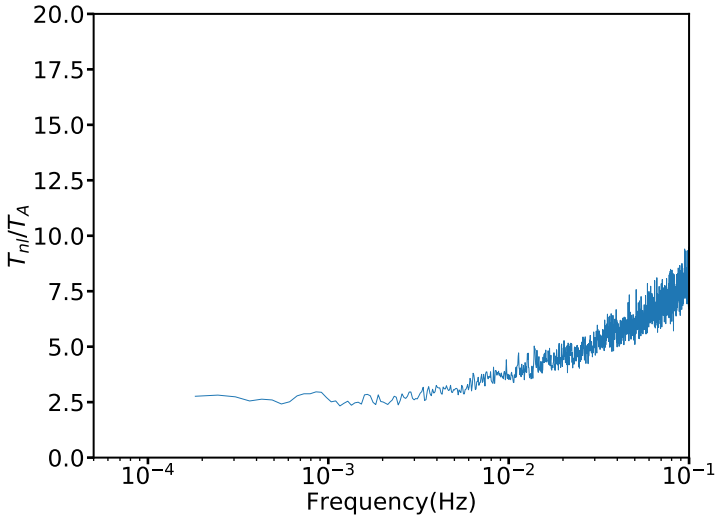

(b)

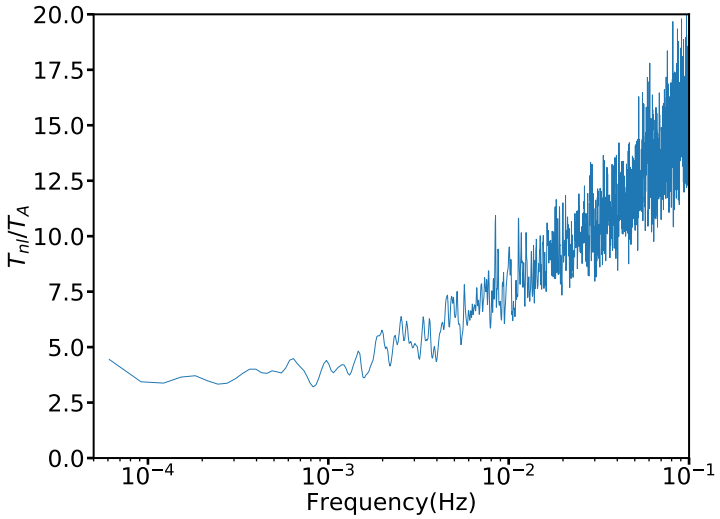

FIGURE 3.12: Ratio of non-linear time to Alfvén time at 0.3 AU: (a) Fast wind (days 72.1-74.5); (b) Alfvénic slow wind (days 66.4-67.6)

Let us simplify that ratio of non-linear time to Alfvén time and analyze which terms are governing it

$$\frac{T_{nl}}{T_A} = \frac{\lambda/Z}{\lambda/V_A} \tag{3.8}$$

$$= \frac{V_A}{Z} \tag{3.9}$$

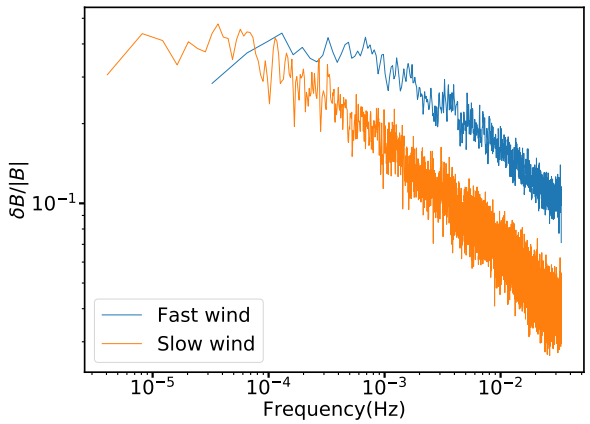

FIGURE 3.13: $\delta B/B$ at different scales of fast wind (2008 days 59.15-61.65) and slow wind (2008 days 234-245.5).

$$= \frac{\langle B \rangle / \sqrt{\rho \mu_0}}{\sqrt{2 f E_b(f)}} \tag{3.10}$$

$$= \frac{\langle B \rangle / \sqrt{\rho \mu_0}}{\sqrt{2 \delta b^2}} \tag{3.11}$$

$$= \frac{\langle B \rangle / \sqrt{\rho \mu_0}}{\sqrt{2 (\delta B / \sqrt{\rho \mu_0})^2}} \tag{3.12}$$

$$\propto \frac{\langle B \rangle}{\delta B} \tag{3.13}$$

Interestingly, what we observe is that T_{nl}/T_A is mainly dependent on the ratio $\frac{\langle B \rangle}{\delta B}$. This term is the main constraining factor and responsible for the observed behavior of the ratio of non-linear time to Alfvén time and plays a significant role in the turbulence evolution. The saturation of T_{nl}/T_A in the f^{-1} frequency range is directly related to the saturation of $\frac{\langle B \rangle}{\delta B}$ value. This can be observed through Figure 3.13, where $\frac{\delta B}{\langle B \rangle}$ is shown for an example of slow and fast wind interval. Here we observe that saturation of $\frac{\delta B}{\langle B \rangle}$ begins where the spectral breaks are observed. Even though the frequency where the saturation begins are different, the amplitude of saturation is the same for the slow and fast solar wind.

Matteini et al. (2018) from their fast wind studies suggested that the saturation of magnetic field Alfvénic fluctuations is responsible for the $1/f$ spectrum. Recently, the study by Bruno, R. et al. (2019) which is similar to us have shown that amplitudes of the Fourier modes reached a limit, i.e. there is the saturation of fluctuations (δB) below a certain frequency. Interestingly the frequency where the initiation of the saturation point happens as we move towards the lower frequency is the spectral break.

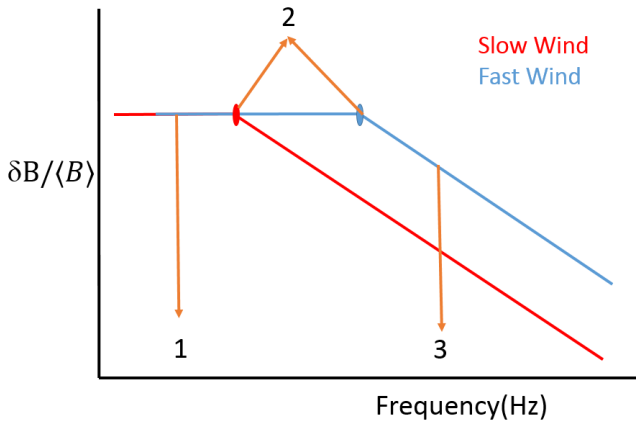

FIGURE 3.14: Schematic of $\delta B/B$ for usually observed slow and fast solar wind, here we point three different regions. Region 1, frequency below the spectral break, where amplitudes and frequencies are the same. Region 2, at the spectral break, amplitudes are the same, but the frequencies are different. Region 3, where amplitudes are different, but the frequencies are the same.

In Figure 3.14 we show a schematic of generally observed $\delta B/B$ vs frequency for the slow and fast solar wind. In the figure, we point out three different regions indicated as 1,2 & 3. One below the spectral break frequency of the slow wind, two at the spectral break frequency of slow and fast wind, three above the spectral break frequency of the fast wind.

Figure 3.14 is useful to get a physical picture of how the slow and fast wind normalized amplitudes and scales compare around the spectral break. To explain this we show a schematic of an eddy or a structure in three different regions in Figure 3.15 corresponding to Figure 3.14. First, the region below the spectral break frequency of the slow wind, we show that the normalized amplitudes are the same and are also of the same size for both the slow and fast solar wind. Second, at the spectral break frequency of the slow and fast wind, we show that the normalized amplitudes are the same, but the size of the eddy when the cascade begins is different in the slow and fast wind. Third, above the spectral break frequency of the fast wind, we show that the normalized amplitudes are different for the same size.

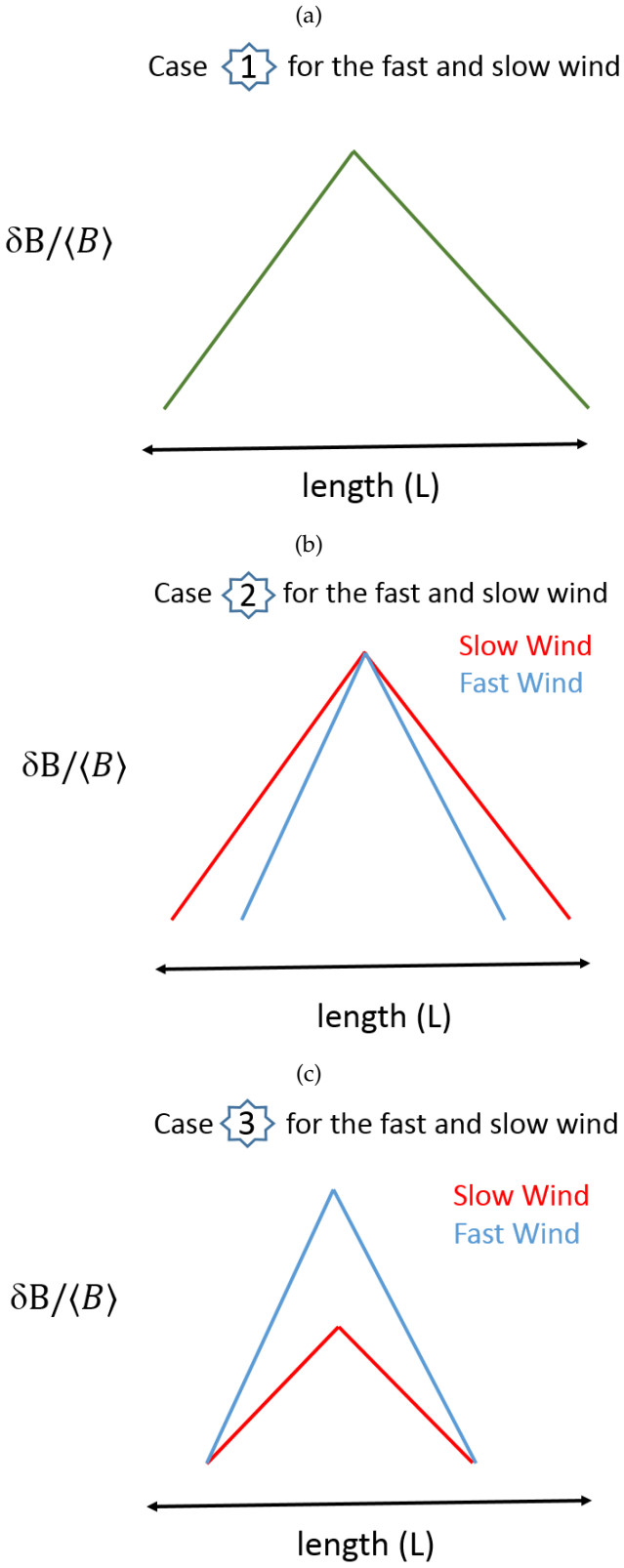

FIGURE 3.15: Schematic of how the eddy sizes and amplitudes may be related to regions shown in the Figure 3.14 in the slow and fast solar wind. (a) shows the region 1 when $\frac{\delta B}{\langle B \rangle}$ and the frequency are similar. (b) shows the case 2 at the spectral break when $\frac{\delta B}{\langle B \rangle}$ is similar, but the frequency is different. (c) shows case 3 where the $\frac{\delta B}{\langle B \rangle}$ is different but the frequency is the same.

Our analysis of *HELIOS* data shows that $\frac{\langle B \rangle}{\delta B}$ remains constant between 0.3 and 1 AU, thereby confirming the constant value of T_{nl}/T_A at the spectral break, irrespective of the distance from the Sun.

To summarize:

- Even though the value of the non-linear time T_{nl} strongly depends on the type of solar wind, the ratio of non-linear time to Alfvén time at the spectral break (between the f^{-1} and inertial range) is found to be close to 2, irrespective of the wind type and distance.
- The $\frac{T_{nl}}{T_A}$ ratio saturates close to 2 in the whole f^{-1} range, irrespective of the type of the wind and distance from the Sun.
- This constancy of the $\frac{T_{nl}}{T_A}$ ratio at the spectral break suggests that the same number of accumulated Alfvénic collisions might be needed for the turbulent energy cascade to be initiated both in the slow and the fast solar wind.
- This also suggests that the evolution of turbulence at the interface between the f^{-1} and inertial ranges is mainly constrained by the value of the term $\frac{\langle B \rangle}{\delta B}$, in agreement with Matteini et al. (2018) and Bruno, R. et al. (2019).

In the next section we shall move to the other side of the spectrum and investigate the evolution of turbulence at kinetic scales.

3.4 Kinetic scale turbulence in the inner heliosphere

The material in this section is also presented partially in the recently submitted article by Alexandrova et al. (2019), in which the author of this thesis is a second author. The work shown here is the contribution of the author in that article.

In this section, we will focus on the evolution of turbulence in the kinetic and dissipative ranges, i.e near ion and electron scales. Our focus will be on the inner heliosphere, using the magnetic field spectral data from *HELIOS* 1. Due to the lack of data between 1 to 7 Hz we will not be focusing on the transition region at the ion scales. Our focus here is on the frequency range above the ion transition region and at least until the electron transition region.

The properties of solar wind turbulence in the kinetic range have received considerable attention in recent years. The large interest is motivated by the role this range plays in mediating the partition of energy among particle species, which in turn affects the large scale properties of plasma (Goldstein, Roberts, and Fitch, 1994). Generally in a turbulent medium, energy is injected at the large scales and dissipate at the small scales, this can be due to viscous effects when the collisions between the particles are dominant. However, as we know that the solar wind is dominantly collisionless, here wave-particle interactions may play a prominent role in the exchange of energy between the fields and particles (Goldstein et al., 2015). However, there are also indications that dissipation may take place at larger scales in relation to plasma turbulence.

As of today, the mechanism of the dissipation in the solar wind kinetic range is poorly understood. Studies have shown that dissipation is setting in at two different scales that are associated respectively with ion and electron motion (Sahraoui et al., 2010; Alexandrova et al., 2012). One of the recent and key result related to the dissipation mechanism at the ion transition region is the evidence of proton-cyclotron resonant damping, which is observed to be occurring at least 50% of the time.

Unfortunately, there have been relatively few observations of the magnetic field in the electron kinetic range in the solar wind. High time resolution particle measurements are even more scarce. Because of the limited availability of observational data the space science community has recently submitted different mission proposals that precisely aim at properly sampling the kinetic range: *TOR*, *THOR* and *DEBYE*. Missions such as MMS (Magnetospheric Multi-Scale) were designed to study rapid fluctuations up to electron kinetic scales. However, their instruments are designed to operate in the magnetosphere and are not sensitive enough for solar wind conditions.

The mission that has really opened access to the electron kinetic range in the solar wind (at 1 AU) is *CLUSTER* whose STAFF instrument (Cornilleau-Wehrlin et al., 2003) measures electric and magnetic fields up to 4 kHz; this frequency range allows to probe the kinetic range down to the electron scales such as electron Larmor radius (ρ_e) and the electron inertial length (λ_e). The search-coil magnetometer(SCM) of *CLUSTER* is the most sensitive magnetometer which has ever flown (Goldstein et al., 2015). It allowed to capture the low-amplitude magnetic fluctuations in the solar wind which has never been measured before. Several observational studies of spectra at kinetic scales at 1 AU are based on these data (Alexandrova et al., 2012; Alexandrova et al., 2013; Sahraoui et al., 2009; Sahraoui et al., 2013). What is still missing, however, is a thorough study of solar wind turbulence at kinetic scales in the inner heliosphere.Because no systematic study of the magnetic field turbulence at kinetic scales has been performed yet in the inner heliosphere.

HELIOS is the first (and until the launch of Parker Solar Probe in 2018, the only) mission to measure high-frequency magnetic fields in the inner heliosphere. The search-coil onboard *HELIOS* 1 measures fluctuations up to 2.2 kHz. In their study of these data, Denskat, Beinroth, and Neubauer (1983) showed that the PSD of the magnetic field in the kinetic range approximately follows power-law $E_B \propto f^{-3}$ with the same spectral index of -3 whatever the radial distance from the Sun between 0.3 and 1 AU. However, they did not study frequencies larger than 470 Hz. In addition, they performed a statistical study and did not attempt to remove the contribution from coherent whistler wave activity at those high frequencies. Therefore and to the best of our knowledge, these high-frequency spectral data from *HELIOS* 1 have never been analyzed in detail.

To study how the turbulence spectra at kinetic scales are behaving at different radial distances in the inner heliosphere we use the magnetic field spectral density values from the *HELIOS* 1 search-coil. We use spectra from the fast wind to study the spectral shape, the main reason behind using the fast wind is due to the presence of higher amplitude fluctuations compared to the slow wind so that we can probe up to higher frequencies. Another important reason is that slow wind intervals are usually observed to be influenced by the whistler waves and chances are high that studied spectra might have been influenced by whistlers. Therefore, in what follows, we shall focus on fast wind conditions only.

In Figure 3.16 we show the ratio of the amplitude of the PSD between three different frequency channels of the SCM for slow and fast wind at 0.3 AU. We can observe how intermittent waves are influencing the slow wind spectra. Notice how in fast wind conditions this ratio remains much more constant, which indicates that the spectral shape remains nearly constant.

As in Chapter 5 for the study of whistler waves we first identify a total number of 246'543 individual spectra of the B_y component. These spectra are measured in 8 logarithmically-spaced frequency bands whose central frequencies are: 6.8 Hz, 14.7 Hz, 31.6 Hz, 68 Hz, 147 Hz, 316 Hz, 681 Hz, and 1470 Hz. We identify those

spectra whose value at 147 Hz exceeds the instrument noise floor by at least a factor of 2. This noise level, which is further described in Chapter 2 is taken from Neubauer, Musmann, and Dehmel (1977). While all low-frequency channels offer a good signal-to-noise ratio, the other ones are being increasingly dominated by noise as their frequency increases. The presence of instrumental noise manifests itself by a flat signal with occasional spikes. Therefore, it is particularly important to isolate spectral values that are physically meaningful.

Among the spectra that are selected, we find 2% of them to have a bump that is the signature of narrowband whistler waves, see Chapter 5. These spectra are discarded. The remaining spectra represent what we call background turbulence spectra; they are similar to the ones discussed by Alexandrova et al. (2012) using *CLUSTER* data, see Figure 3.17. To further ensure that our data are not contaminated by instrumental noise we discard all spectral densities whose values do not exceed the noise floor by at least a factor of 3. A factor of 3 seems to be a reasonable approximation as this assumption makes sure that the data considered is not influenced by the noise of the instrument, this has been even verified by looking into the correlation plots between the consecutive bands. However, downside of this assumption is that we will be considering the spectral shape of only high amplitude fluctuations.

To study the shape of background turbulence spectra up to the electron scales, we have to work with the spectra which satisfy our SNR condition beyond the frequency bands which covers the electron scales such as electron Larmor radius (ρ_e) and the electron inertial length (λ_e).

$$\rho_e = \sqrt{2k_b T_{e\perp}/m_e}/(q_e B/m_e), \tag{3.14}$$

$$\lambda_e = c/\sqrt{n_p q_e^2/(m_e \epsilon)}, \tag{3.15}$$

where, k_b is Boltzmann constant, $T_{e\perp}$ is perpendicular electron temperature, q_e is electron charge, m_e is mass of the electron, B magnetic field magnitude, n_p proton density, ϵ is permitivity of free space.

These electron scales are encountered at different frequency bands at different distances, as the spacecraft approaches closer and closer to the Sun these scales are observed at higher and higher frequencies due to the change in the plasma properties. For example, these scales are generally encountered $\sim$ 60 Hz at 1 AU and at 0.3 AU these scales are encountered $\sim$ 200 Hz. Therefore, as we approach closer to the Sun we need spectra which satisfy our SNR of 3 at high frequencies. Interestingly as we approach closer to the Sun, the signal to noise ratio of the magnetic field fluctuation increases and this helps in probing the higher frequency ranges.

We use the fast wind (>600 km/s) spectra for our analysis, as they have a higher signal to noise ratio so that we can probe high-frequency regions and get a good picture of turbulence evolution. Another important factor to use the fast wind is that the occurrence of whistler waves is very sparse in the fast wind as shown in the studies of Lacombe et al. (2014) and also in our study in Chapter 5. This implies the probability of background turbulence spectra getting influenced by whistler waves is very less.

For our analysis we have looked into the fast wind spectra at 0.3 and 0.9 AU, for which the electron scales, λ_e and ρ_e are well covered.

The spectra analyzed at two different distances are shown in the Figure 3.18, for the spectra at 0.3 AU we have considered spectra which satisfied the 3x noise cutoff at least for the first 7 bands (681 Hz) and for the case of spectra at 0.9 AU we have

considered spectra which satisfied noise cutoff at least till 5 bands (147 Hz). These are the best possible spectra we could have to study the turbulence evolution to the maximum possible frequency at their corresponding distances using *HELIOS* 1.

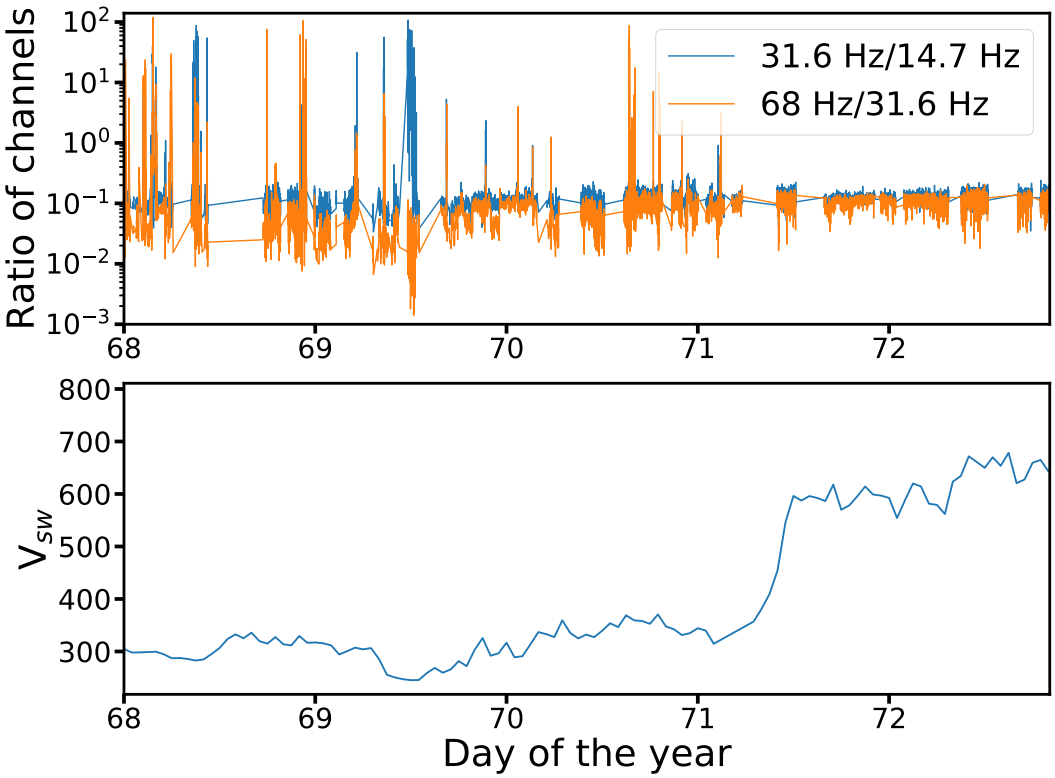

FIGURE 3.16: The ratio of PSDs between three different channels is shown in the upper panel and variation of velocity in the lower panel around 0.3 AU in 1975 from *HELIOS* 1.

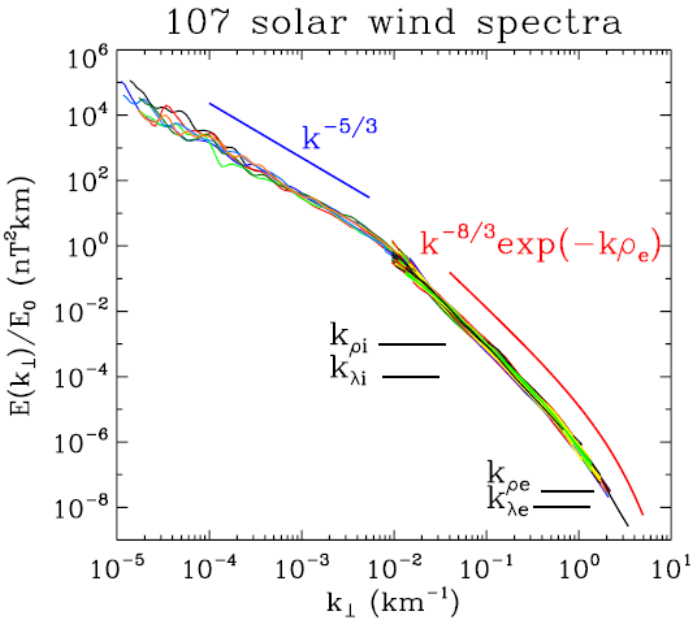

FIGURE 3.17: Spectra analyzed in kinetic scales at 1 AU, taken from the studies of Alexandrova et al. (2012)

(a) (b)

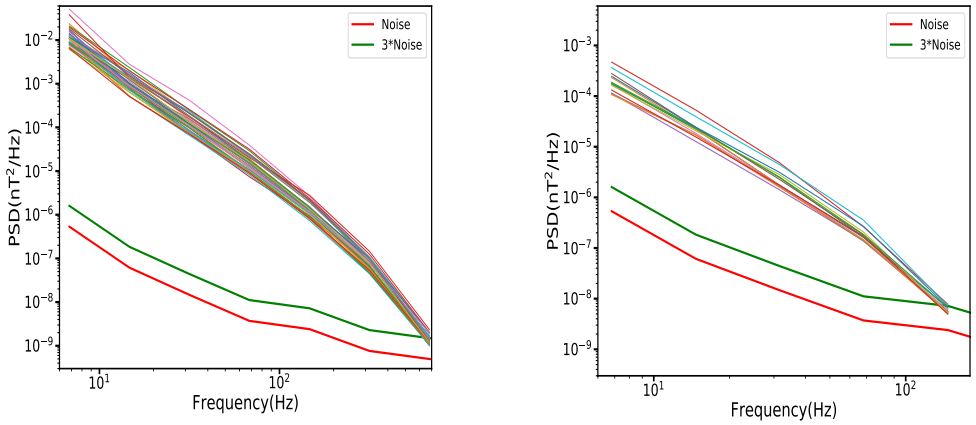

FIGURE 3.18: Fast wind spectra analyzed at different distances during Jan-Mar 1975 (a) Spectra at 0.3 AU (b) Spectra at 0.9 AU.

Now after selecting the spectra, we would like to know which model fits well the turbulence spectra in kinetic scales and explains the observed spectral behavior. There are two well discussed models for the PSD of the magnetic field at kinetic scales in the solar wind at 1 AU:

- An exponential model (Alexandrova et al., 2009; Alexandrova et al., 2012)
- A double power law model (Sahraoui et al., 2009; Sahraoui et al., 2010)

So, which model to be used for our analysis? A recent study by Schreiner and Saur (2017), in which they use an analytic model which integrates the energy transport

from large to small scales and the dissipation of turbulence is explained by collisionless damping of Kinetic Alfvén waves (KAW), suggests that the exponential model proposed by Alexandrova et al. (2012) to be one of the best models to suit the solar wind turbulence spectra at 1 AU in kinetic scales.

In the study by Alexandrova et al. (2012) other than using the exponential model, they have also compared their results of fitting with the double power-law model. Their conclusion was that there is no significant difference between the models in terms of fitting, except that the double power-law model has more free parameters than the exponential model.

Even though there is no significant change in terms of fitting, there is a major difference in the outcome of the analysis of two models. The exponential model points towards the universality of the turbulent spectrum at the kinetic scales and double power-law contradicts it, suggesting that spectrum has to be studied on the case to case bases (Sahraoui et al., 2010; Sahraoui et al., 2013). The significance of the exponential model is that there is no need of studying the spectra by an event to event as it is governed by a nearly universal equation (at 0.3 or 1 AU) unless there are some transient events or in the presence of any narrowband waves such as whistler waves.

We fit our spectra with the exponential model proposed in Alexandrova et al. (2012), which is an improvement to the old model of Alexandrova et al. (2009) and verify whether the spectral properties observed at 0.3 AU and 0.9 AU have a correlation with what has been observed at 1 AU.

Spectra analyzed in Alexandrova et al. (2012) and their spectral shape is shown in Figure 3.17.

The model we use intially to fit the spectra is:

$$Af^{-\alpha}exp(-f/f_d) \tag{3.16}$$

In Figure 3.19 we show how the spectra have been analyzed and the spectral fit is made. First the spectra that are at least 3 times above the noise level are selected as in the Figure 3.19 (a), then the noise is removed from the spectra and it is shown in Figure 3.19 (b) and then the spectra are fitted with the model equation 3.16.

We did this spectral fitting for all the spectra, which satisfied the SNR$\sim$ 3 at least for 7 spectral bands (681 Hz) at 0.3 AU. In Figure 3.20 we show the fitting parameter 'α' values for the case of 39 spectra at 0.3 AU. We observe how the values of 'α' are concentrated around 2.5-2.9.

The dissipation scale (l_d) can be estimated from the dissipation frequency (f_d) obtained from the fitting and using the Taylor hypothesis, $l_d = V_{sw}/2\pi f_d$. We would like to know to which scales the dissipation scale (l_d) is correlated to, is it electron inertial length (λ_e) or electron gyro length (ρ_e)? Here, $\lambda_e = c/\omega_{pe}$ and $\rho_e = \sqrt{2kT_{e\perp}/m_e}/\omega_{ce}$.

In Figure 3.21 we show the correlation plots, where we look into the correlation between the l_d and λ_e, and l_d and ρ_e. The correlation analysis suggests that the dissipation scale is correlated (> 0.6) with the electron Larmor radius as in the studies of Alexandrova et al. (2012), Sahraoui et al. (2013), and Schreiner and Saur (2017). The correlation with the electron inertial length is found to be negligible (< 0.2) as shown in Figure 3.21.

We have verified whether the subtraction of the noise floor has any significance on our fitting, for that, we have done a similar fitting of the exponential function without removing the noise. The results we have obtained are similar to the one with the noise subtracted. Therefore, we have understood that the removal of noise is not

(a) (b)

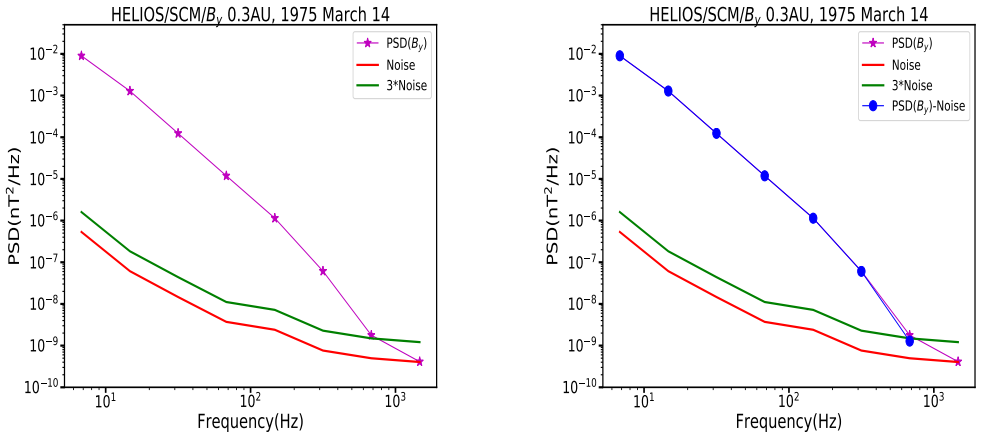

(c)

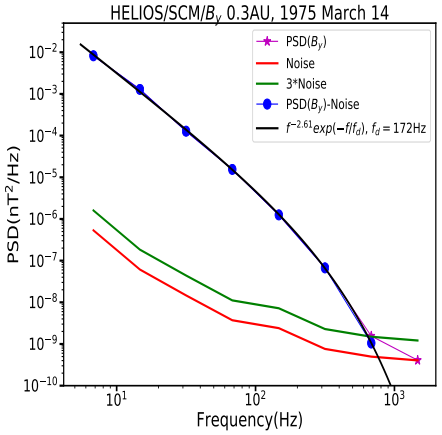

FIGURE 3.19: Representation of how the analysis has been done (a) Power spectral density values. (b) Only points above 3 times the noise are considered for the analysis, background noise is removed from the 7 power spectral density values (c) An exponential model has been fitted.

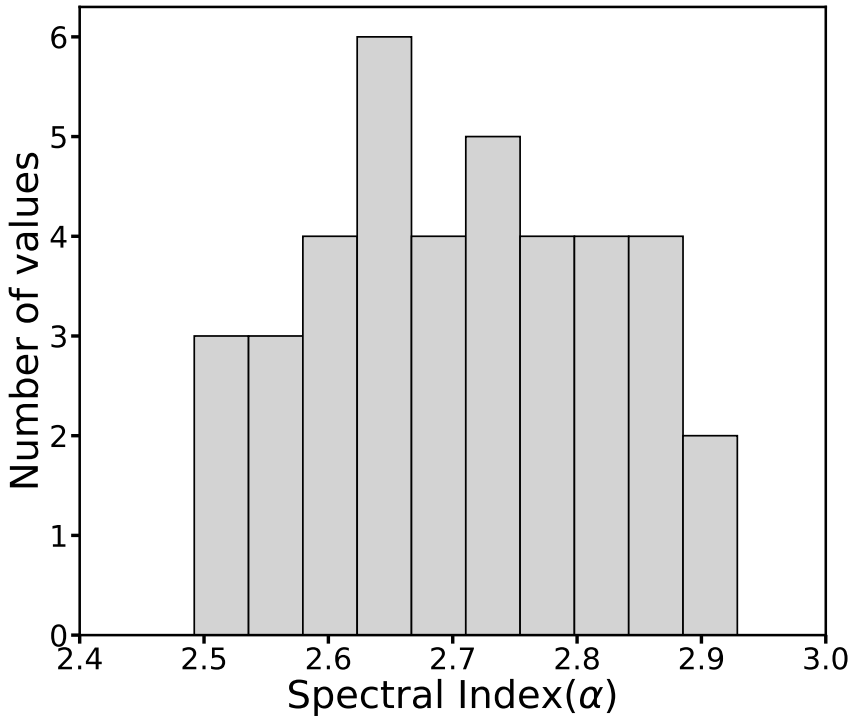

FIGURE 3.20: The values of 'α' at 0.3 AU, considering the noise cutoff for 7 spectral bands

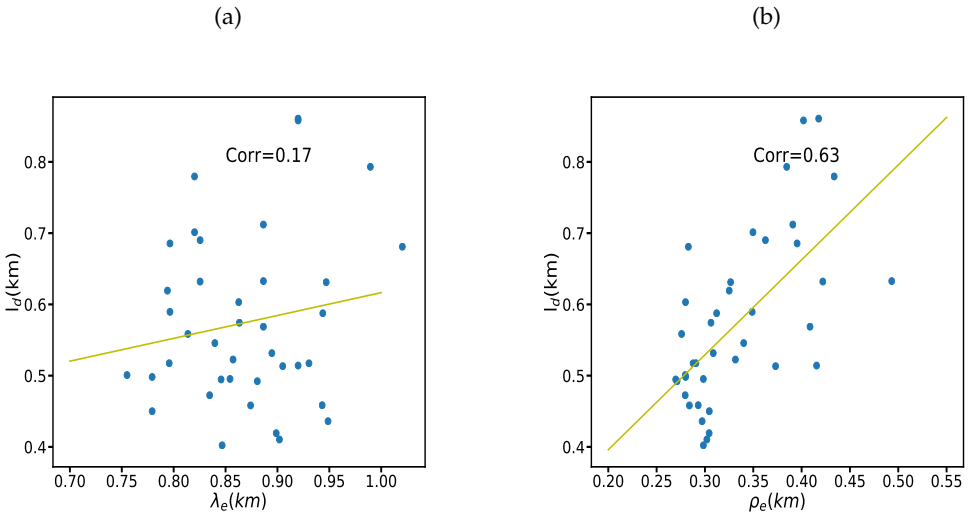

FIGURE 3.21: Scatter plot of dissipation scale (l_d) vs different electron scales at 0.3 AU, (a) l_d versus ρ_e, (b) l_d versus λ_e.

playing a significant role in determining the shape of the spectra in our analysis. This is on the expected lines as we have chosen spectra of higher amplitudes.

We did a similar analysis with the spectra observed at 0.9 AU. We found similar spectral indices (α) values and the high correlation ($\approx$0.6) of the dissipation scale with the electron Larmor radius (ρ_e).

After our initial analysis, we would like to decrease the number of free parameters in the fitting. As shown before we found that the spectral index values are concentrated in a small range between 2.5-2.9, so it can be approximated by to a single value. Studies by Alexandrova et al. (2012) at 1 AU have shown a similar range of spectral index values and they have suggested that the spectral index value can be fixed to 8/3. In support of these results are the studies using different kinetic range turbulence models which point the spectral index value to be 8/3 (Galtier, Pouquet, and Mangeney, 2005; Boldyrev and Perez, 2012).

Recently, studies by Schreiner and Saur (2017), using their analytic model which explains the solar wind turbulence dissipation by kinetic Alfvén waves and combining the observations at 1 AU have shown that the value of spectral index around 2.7 describes kinetic turbulence spectra well. They suggest that deviations from the usually expected 7/3 value from the theoretical calculations using KAW (Howes et al., 2006; Schekochihin et al., 2009) might be related to intermittency or sample effects. Therefore, we fix our $\alpha = 8/3$.

For the case of dissipation frequency f_d, we also found that it is highly correlated with the electron larmor frequency ($f_{\rho e} = V_{sw}/2\pi\rho_e$), but there is a difference between the values of f_d and $f_{\rho e}$. Therefore, we introduce $f_d = f_{\rho e}/c$, where 'c' is an adjustable parameter.

Now after the analysis we decrease the free parameters of the proposed model, the improved equation in which $\alpha = 8/3$ and $f_d = f_{\rho e}/c$:

$$Af^{-8/3}exp(-cf/f_{\rho e}) \tag{3.17}$$

Using this model (Equation 3.17) we fit the spectra at 0.3 AU and at 0.9 AU as shown with an example in Figure 3.22. We repeated the correlation studies between l_d and ρ_e at 0.3 AU and found that the correlation was nearly the same with a slight increase from 0.63 to 0.68. Even though our correlation studies at 0.3 AU give similar results as at 1 AU, we have to be careful as we have only 39 spectra in the analysis and this reduces the statistical significance of the result.

From our analysis, we understood that we could even fix the 'c' parameter, i.e. the ratio of $\frac{f_{\rho e}}{f_d}$. At 0.3 AU, the $\frac{f_{\rho e}}{f_d}$ ratio for different spectra are concentrated around 1.6-1.9. We found that the best suited 'c' value for the spectra we have analyzed is $\sim$ 1.8. We have understood that the spectra could be modeled with only one free parameter. Therefore, we can fit the whole kinetic scale spectra from the ion scale to the dissipation scale and beyond that using only one free parameter (A) as suggested in the studies of Alexandrova et al. (2012).

For further detailed analysis at 0.3 AU using the exponential model for a large number of spectra at 0.3 AU, but only using the first 6 spectral bands (up to 316 Hz) we refer to Alexandrova et al. (2019).

The ability to adequately reproduce all spectra between 0.3 and 0.9 AU with the same model in which the only free parameter is the amplitude of the fluctuations suggests the presence of some unique spectral shape for all the distances. This along with the studies of Alexandrova et al. (2012) at 1 AU guides us in proposing that there is a unique spectral model that fits all the kinetic scale spectra observed at different radial distances in the heliosphere. This explains that the evolution of

turbulence and its dissipation is governed by similar physical quantities at all the distances. Even though the electron inertial length is the first physical spatial scale encountered during the cascade, it is the electron Larmor radius that governs the dissipation scale at all the distances. Our result explains that there is universality in the turbulence evolution, at least in the heliosphere.

How does the transition point between the 8/3 power-law and the exponential shape vary with radial distance ? From our studies we have understood that the transition point is related to electron Larmor frequency, therefore we can understand that the radially the transition point varies as to how the electron Larmor frequency varies. We can have a rough estimate of the radial dependence:

$$f_{\rho e} \propto \frac{\mathbf{B}}{\sqrt{T_{e\perp}}}. \tag{3.18}$$

Considering the case for the fast wind, we know $T_{e\perp} \propto R^{-0.53}$ (Stverák, Trávníček, and Hellinger, 2015) and $\mathbf{B} \propto R^{-1.6}$ (Perrone et al., 2019). Therefore, radially the kinetic scale electron transition scale is expected to vary as $\approx R^{-1.35}$.

For further discussion on what these turbulence spectra might actually be made up of (waves, structures etc) and on the universality of the turbulence spectra, we would like the readers to refer to the recently submitted article by Alexandrova et al. (2019).

We would like to add a word of caution regarding our analysis, we have only used the exponential model to fit the spectra. The double power-law model has not been tested due to the limitations on the data to fit a second power law properly. However, we can point out a few similarities between the two models. The spectral index we observe in the exponential model corresponds to the initial power-law spectral index observed before the spectral break in the double power-law model. The spectral index of this power-law at 1 AU (Sahraoui et al., 2013) matches well with the spectral indexes of different spectra fitted using the exponential model at different distances. However, the main difference between the two models comes after the electron transition point. In our model exponential shape takes over naturally from the electron transition point, whereas in double power-law model a steeper power-law between 3.5 to 4.5 is fit from the electron transition point (Sahraoui et al., 2013).

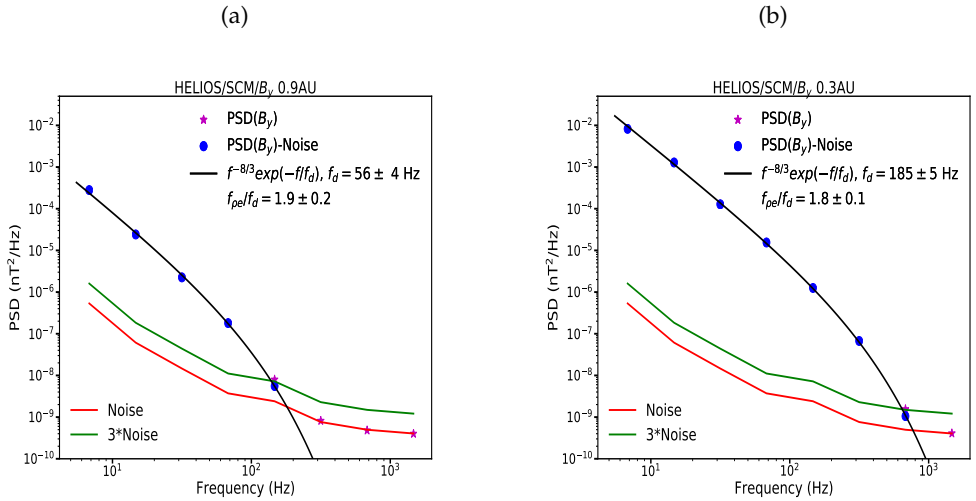

FIGURE 3.22: Example of one individual spectrum fit using the Equation 3.17 at 0.9 AU and at 0.3 AU

3.5 Evolution of turbulence from the f^{-1} range to the dissipation range in the inner heliosphere

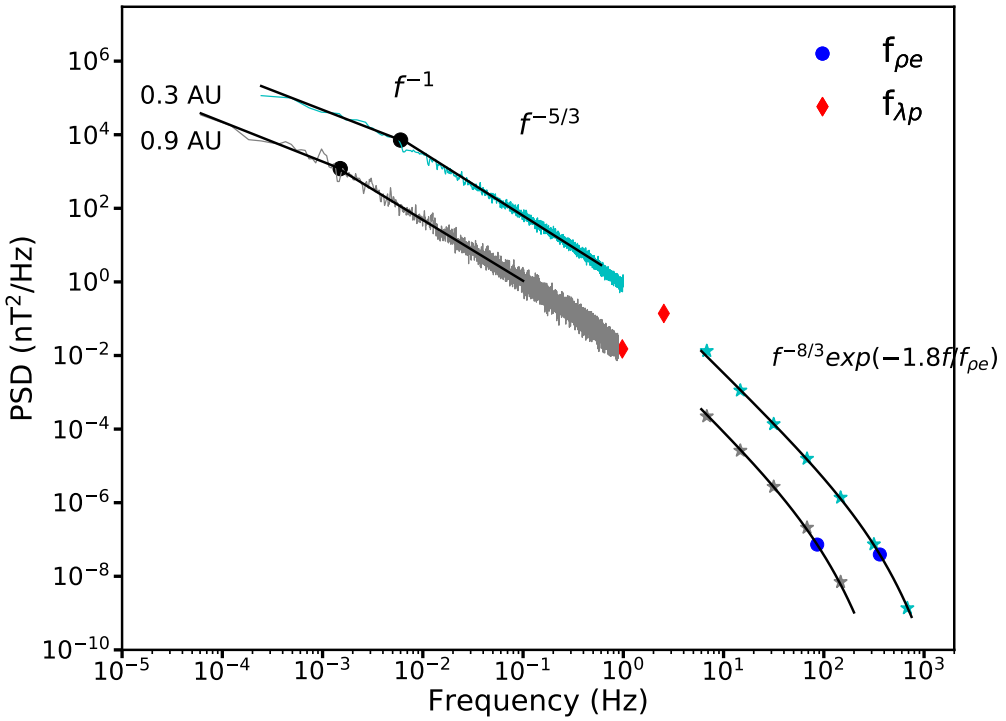

FIGURE 3.23: Evolution of turbulence from the f^{-1} range to the dissipation range in the inner heliosphere at 0.3 AU and 0.9 AU for fast wind intervals.

From our study of magnetic field turbulence spectra in low-frequency scales using fluxgate data and high-frequency scales using search-coil data at different radial distances in the inner heliosphere, we observe that the turbulence spectra follow certain general behavior.

- A 1/f power law in the very low-frequency range: This region is considered as an energy reservoir from which energy is injected for the turbulent cascade to initiate.
- A Kolmogorov-like $f^{-5/3}$ spectrum as we move towards higher frequencies away from 1/f spectra: This region considered to be inhibited by the dissipationless turbulent cascade of energy till the ion scales are reached.
- A transition region: A region between the Kolmogorov-like $f^{-5/3}$ spectrum and the kinetic range. We cannot properly observe this spectral range due to the lack of measurements from the *HELIOS* and literature studies to date suggest the spectra are steepened after the inertial range and the slope is suggested to vary between -2 to -4 (Leamon et al., 1998; Smith et al., 2006; Chen et al., 2012; Roberts, Li, and Li, 2013).
- A kinetic range or dissipative range: An initial power-law spectra with steeper slopes of the order of -8/3 dominates till scales closer to the electron Larmor radius and then the spectra start to show exponential behavior as the dissipation effects start to dominate.

In Figure 3.23 we show the radial evolution of solar wind turbulence from injection to the dissipation scales using the fast solar wind at two different radial distances 0.3 AU (Day 72.4-73.5, 1975) and 0.9 AU (Day 14.4-15.9, 1975). These are the intervals where we have observed the best possible kinetic spectra to probe the high-frequency scales as shown in the previous section. The low-frequency spectra are calculated using the magnetic field values from the fluxgate magnetometer as explained in section 3.3 and the kinetic scale spectra showed is the average of the individual power spectral density spectra shown in the previous section 3.4. This is the first time that a full evolution of turbulence from injection to the dissipation scale is shown in the inner heliosphere, these observations are important as using the similar magnetic field spectra at different distances we can study the similarities and differences in the turbulence evolution through out the inner heliosphere and beyond.

Using the spectra observed at different radial distances at different scales, we understood that the turbulence spectra follow a general shape from the range of energy injection to the dissipation, irrespective of the distance from the Sun (atleast ≤ 1 AU). We have made a prediction for the possible magnetic field spectra, which *Parker Solar Probe* would be measuring in the fast solar wind as close as 0.05 AU. For the prediction of the spectra, we use the plasma parameters as estimated in the studies of Maksimovic et al. (2019). For the turbulence level estimation, we have assumed that the $\delta B/B \approx constant$ at all the radial distances and estimated the turbulence level at 0.05 and 0.1. For the spectral break (f_b) identification, i.e. break between f^{-1} and $f^{-5/3}$, we have analyzed that the break is evolving like $f_b = f_0(R_0/R)^{1.5}$, as in the studies of Bruno and Carbone (2013b). We use 0.3 AU as a reference and predict f_b for 0.05 AU and 0.1 AU. Kinetic scale spectra are predicted assuming that the spectra observed at 0.05 and 0.1 AU follow a similar spectral shape as at 0.3 AU. The predicted spectra are shown in Figure 3.24, taken from the studies of Alexandrova et al. (2019).

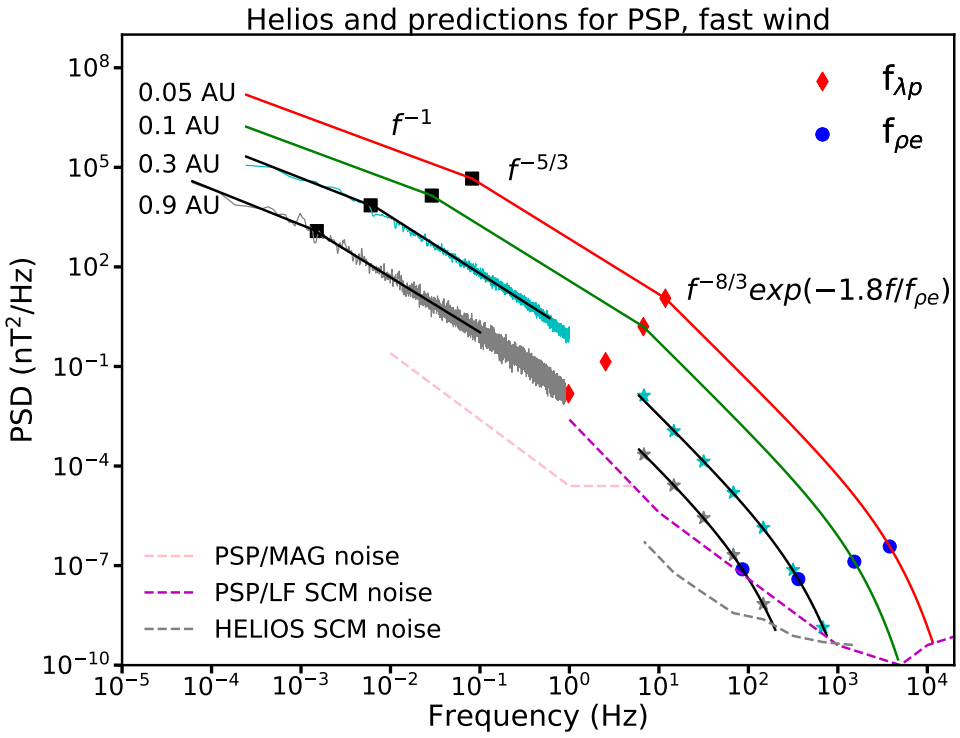

FIGURE 3.24: Extrapolation of magnetic field spectra observed at 0.3 Au to possible spectra at 10 and 20 solar radii, taken from Alexandrova et al. (2019).

3.6 Conclusion

In this chapter, we have studied the evolution of turbulence from the initiation of the turbulence cascade to the dissipation and also the radial evolution of the turbulence using the *WIND* and *HELIOS* spacecraft.

Initially, using large slow solar wind intervals of magnetic fields from the *WIND* spacecraft at 1 AU, we have analyzed the very low-frequency scales of the slow solar wind. We have observed a clear presence of f^{-1} scaling of the PSD of magnetic field fluctuations in non-Alfvénic slow solar wind samples, this is the first time that a f^{-1} in non-Alfvénic slow solar wind interval is observed. This observation has a very important consequence as we now know the characteristic scale for the initiation of non-linear energy cascade in the slow solar wind, which was not known before. This information helps us in understanding the basic similarities and differences in the evolution of turbulence in the slow and fast solar wind.

The difference between the spectral break frequency between the slow and fast wind interval is found to be around 1 decade. In the slow wind, the spectral break is found to be around 10^{-4} Hz, whereas for the fast wind case the break is found to be around 10^{-3} Hz at 1 AU.

We have calculated the ratio of non-linear time (T_{nl}) to the Alfvén time (T_A) at different frequency scales for the slow and fast wind intervals we have analyzed. We observe a decrease in $\frac{T_{nl}}{T_A}$ ratio as we move towards lower frequencies and once the

spectral break frequency corresponding to that interval is encountered the $\frac{T_{nl}}{T_A}$ ratio saturates. Quite surprisingly, irrespective of the type of wind, the saturation value is the same in the case of fast and slow wind. The $\frac{T_{nl}}{T_A}$ ratio at the spectral break for both the slow and fast wind at 1 AU is around 2. Therefore, we can suggest that the same number of Alfvénic collisions is needed for the non-linear cascade to be initiated in both the slow and fast solar wind.

The $\frac{T_{nl}}{T_A}$ ratio is found to be dependent on the $\frac{\langle B \rangle}{\delta B}$ or $\frac{\delta B}{\langle B \rangle}$. We understood that the spectral breaks in the slow and fast wind are constrained by the same normalized amplitudes ($\frac{\delta B}{\langle B \rangle}$) at the spectral break. The similarity is due to the saturation of the normalized fluctuations ($\frac{\delta B}{\langle B \rangle}$) to the same value below the spectral break frequency irrespective of the wind type and distance. However, the scales at which the spectral breaks are observed in the slow and fast solar wind are different.

After the analysis of low-frequency scales, we have looked into the high-frequency scales (> 1 Hz) in the inner heliosphere using the search-coil of *HELIOS* 1. We have studied the spectra without the influence of any narrowband whistlers. The spectra initially showed a power-law scaling of around $f^{-8/3}$ and gradually moved towards an exponential shape as the dissipative effects start to dominate. We have observed that the dissipation scale is highly correlated with the electron Larmor radius irrespective of the distance. Radially the electron transition scale which is encountered at the transition point between the $8/3$ power-law and the exponential decay is expected to vary as $\approx R^{-1.35}$.

We have understood that a quasi-exponential model $Af^{-8/3}exp(-cf/f_{\rho e})$ with only one to two free parameters can describe the solar wind kinetic turbulence spectrum of magnetic fields, i.e. scales above the ion frequency scales and beyond the electron scales such as electron Larmor radius and electron inertial length.

The validity of the exponential model at different radial distances analyzed in the inner heliosphere and its similarities to the exponential hydrodynamic turbulence models directs us in suggesting that there is a kind of universality of magnetic turbulence in the whole heliosphere. However, readers have to consider this result with caution as we have not tested other fitting models for our spectra.

Finally, we present the whole picture of turbulence evolution together, i.e. from the initiation of the non-linear cascade in low-frequency scales to the dissipation scales in the inner heliosphere for the very first time using the fast wind spectra at 0.3 and 0.9 AU.

A detailed study has to be done in the future to understand what the kinetic turbulence spectra is actually made up of in the inner heliosphere, whether it is constituted of waves or structures or a mixture of them. This can be done with the ongoing missions like Parker Solar Probe and the new mission Solar Orbiter, which have the capability to provide high-resolution waveform and particle data.

3.7 Résumé en français: La turbulence des échelles d'injection aux échelles dissipatives

Le vent solaire subit des fluctuations à toutes les échelles que l'on regroupe généralement sous le vocable générique "turbulence plasma". Toutefois, derrière un mouvement apparemment désordonné se cachent un ensemble de processus physiques qui laissent leur empreinte dans les propriétés statistiques des fluctuations. Ces dernières ont la particularité d'être auto-similaires sur un large plage d'échelles. Il est alors commode de les analyser dans le domaine spectral. L'invariance d'échelle

se traduit en effet par une densité de puissance spectrale en forme de loi de puissance $P(f) \propto f^{\beta}$. Dans le régime dit inertiel où domine la cascade turbulente, l'indice spectral β est généralement proche de -5/3 (loi de Kolmogorov). Pour des plus basses fréquences (typiquement $f < 1 - 10$ mHz) nous avons le régime dit en $1/f$ qui correspond à des structures cohérentes qui n'ont pas encore été entamées par la cascade turbulente. A l'inverse, pour des fréquences plus élevées (typiquement $f > 1 - 10$ Hz) on entre dans le régime dit cinétique, dans lequel la présence de diverses fréquences caractéristiques du plasma (cyclotronique ionique, cyclotronique électronique, etc.) accentue la valeur absolue de l'indice spectral, jusqu'à ce que la dissipation prenne le dessus et mette fin à la loi de puissance.

La caractérisation de ces divers régimes a fait l'objet de nombreuses études. Toutefois, la plupart ont été effectuées à proximité immédiate de la Terre (à 1 UA du Soleil). Or HELIOS nous offre l'opportunité d'étudier comment ces régimes évoluent en fonction de la distance par rapport au Soleil. Notre étude a fourni plusieurs résultats.

D'abord, nous avons mis en évidence la présence d'un régime dit de $1/f$ dans le vent solaire lent observé par le satellite WIND (qui mesure le champ magnétique du vent solaire à 1 UA). Le régime de $1/f$ avait déjà été observé dans le vent rapide. En revanche son existence dans le vent solaire lent était sujette à caution. Cela tient notamment à la difficulté d'observer les très basses fréquences ($f < 0.1$ mHz) dans des intervalles de vent solaire qui durent rarement plus de quelques jours.

Nous avons aussi montré que temps non-linéaire τ_{nl} associé à la transition entre régime en $1/f$ et régime inertiel est proportionnel au temps d'Alfvén, et ce pour différentes distances du Soleil. Ce résultat original suggère que la transition entre ces deux régimes pourrait être contrôlée par les collisions d'Alfvén.

A l'autre extrémité du spectre, dans le régime cinétique et au-delà des échelles électroniques, nous avons montré que la densité de puissance spectrale peut être approximée par la loi $P(f) \propto f^{-8/3} e^{-cf/f_{pe}}$, où c est un paramètre libre. Cette loi reste valable à différentes distances du Soleil. La même expression se rencontre dans la description de la turbulence en hydrodynamique, ce qui souligne son caractère universel.

Enfin, avec les données des deux capteurs magnétiques de HELIOS 1, nous avons été en mesure d'exprimer la densité spectrale de puissance pour des fréquences allant du régime en $1/f$ jusqu'aux échelles électroniques.

Chapter 4

Non-stationarity in solar wind

The material in this chapter draws heavily on the author's recently published work (Krishna Jagarlamudi et al., 2019).

4.1 Introduction

The stationarity of the solar wind is a frequently made assumption in most of the statistical time series analysis of the turbulence. Stationarity implies strict invariance of statistical properties under all and every time shift (Beran, 1994). This assumption is of considerable importance for properly characterizing finite amounts of random process observations as it leads to many simplifications (Bendat and Piersol, 2000). Usually, a random process can be classified into two types; stationary and non-stationary, and we can further sub divide different classes as shown in the Figure 4.1. Importantly, in order to consider the solar wind as ergodic, which further simplifies the analysis, we need to know whether it is stationary or not first. In ergodic random process, the time-averaged values of the mean and autocorrelation function (ACF) are equal to the corresponding ensemble averages (Bendat and Piersol, 2000).

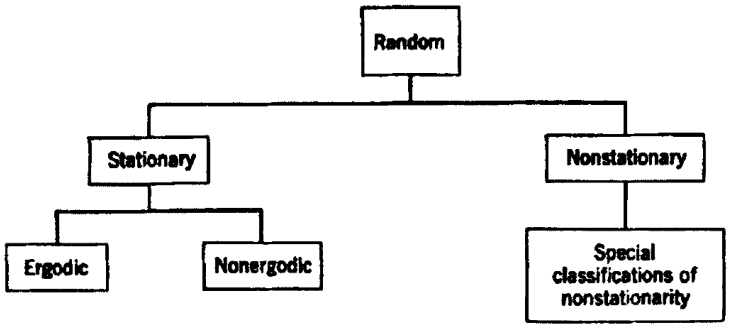

FIGURE 4.1: Classification of random data, taken from Bendat and Piersol (2000)

The main idea of studying stationarity in the context of solar wind other than determining whether the solar wind is stationary or not, we are more interested in knowing how the physical interpretation of different solar wind parameters are affected due to the departure from the stationarity.

The stationarity condition is usually assumed to be satisfied in the solar wind studies. However, there are several physical reasons on why the stationarity might be violated. Some of them can be due to the presence of coherent or some organized structures such as shocks (Tu and Marsch, 1995b; Matthaeus et al., 2015), long-range

memory associated with the sources of the solar wind (Nicol, Chapman, and Dendy, 2009) and many others. Importantly, the source of solar wind, the solar corona is always evolving with respect to time and space, and can be a major cause of non-stationarity.

One of the key question is whether non-stationarity is inherently part of the turbulent solar wind flow. As we will find out, in the time scales (minutes to days) usually considered for solar wind turbulence studies, non-stationarity is indeed an inherent property.

There are quite a few literature studies on answering the question of whether the solar wind is stationary or not. In their pioneering study, Matthaeus and Goldstein (1982) concluded that statistical quantities such as the ACF converge toward a constant value if long enough intervals were considered, typically days to weeks. This would suggest that the solar wind is approximately stationary in time beyond such time scales. Podesta and Roberts (2005) reached the similar conclusion, with special emphasis on the validity of power spectral estimates. Perri and Balogh (2010) extended these results to different parameter ranges in different types of the solar wind based on velocity and their inference was that for the time scales inside the inertial range of turbulence the assumption of stationarity only holds for fast solar wind flows.

The outcome of these different studies is that the problem of stationarity of solar wind largely remains unsettled. To answer the question of stationarity we should start with a clear and realistic definition of what actually stationarity means. The definition of stationarity, which we mentioned earlier is a mathematical concept that applies to populations but cannot be applied to real data with finite samples.

For this reason, almost all of the studies concentrate on weak (wide-sense or second-order) stationarity, for which the necessary condition is that only the first and second order moments are time-invariant (Priestley, 1988). This implies that the expected mean $\mathbb{E}[x(t)] = m_x(t)$ and variance $\mathbb{E}[(x(t) - m_x(t))^2] = \sigma_x^2(t)$ on any time interval should both be independent of time, where $\mathbb{E}(\cdot)$ stands for the expectation.

In addition, the autocovariance function

$$C(t,\tau) = \mathbb{E}\left[(x(t) - m_x(t))\ (x(t+\tau) - m_x(t+\tau))\right], \tag{4.1}$$

should only depend on the time difference τ, so that $C(t,\tau) = C(\tau)$. Equivalently, the autocorrelation function (ACF)

$$\mathrm{ACF}(t,\tau) = \frac{C(t,\tau)}{C(t,0)}, \tag{4.2}$$

should also be time-independent, i.e. $\mathrm{ACF}(t,\tau) = \mathrm{ACF}(\tau)$.

As pointed out by Bendat and Piersol (2000), the above mentioned criteria apply to mathematical expectations (i.e. probability-weighted averages) and are meaningful only when instantaneous time-averages can be performed. This can only be done when we have an ensemble of records for a random process, as shown with an example of ensemble of time records for a random process in the Figure 4.2. However, having an ensemble of records cannot be practically possible when working with the time series measurements from single spacecraft observation. This is because we will have only 1 record as shown in Figure 4.2, but not the ensemble of records. Our aim is now towards determining whether the estimated statistical properties from finite time intervals vary significantly in time or not.

Different approaches have been suggested for the above analysis, (e.g. Priestley

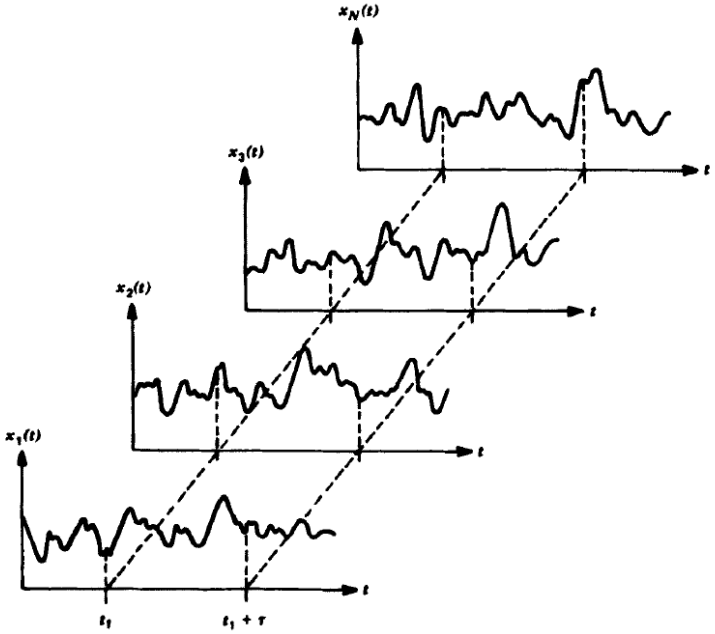

FIGURE 4.2: Example of ensemble of time history records of a random process, taken from Bendat and Piersol (2000)

and Rao, 1969; Bendat and Piersol, 2000; Borgnat and Flandrin, 2009). Among these different approaches, the ACF offers many advantages and is widely used. Primarily, its expression is directly involved in the definition of weak stationarity. Second and most importantly it allows us to check how the absence of stationarity is affecting the correlation length.

There is abundance of literature on the investigation of ACFs in the solar wind: Matthaeus and Goldstein (1982), Klein et al. (1992), Tu and Marsch (1995b), Richardson and Paularena (2001), King and Papitashvili (2005), Matthaeus et al. (2005), Podesta, Galvin, and Farrugia (2008), Wicks, Owens, and Horbury (2010), and Marquette et al. (2018) to mention a few. Most of the studies did not question the effect of non-stationarity on the studied ACFs, which will precisely be our focus here. In what follows, we shall focus on the ACF only and analyze how different time-scales and in different regimes of the solar wind are affected due to the presence of non-stationarity.

4.2 Data

For the study of stationarity, we consider the magnetic field observations made by the fluxgate magnetometer (Lepping et al., 1995) onboard the *WIND* spacecraft between 2006 and 2016. *WIND* was positioned at a constant distance of 1 AU from the Sun, around the L1 Lagrange point in a halo orbit, to constantly observe the Sun in an ecliptic plane. WIND gives us the opportunity to look into long and uninterrupted records of large number of samples from slow and fast wind regimes. The sampling time of the records we consider here is 15 seconds. Therefore, stationarity can be investigated at different time scales from seconds to days. This range covers the inertial range and also includes the integral scale both in the slow and fast solar wind.

In Figure 4.3 we present examples of the fast and slow solar wind magnetic fields, both the data reveal strong fluctuations at all scales.

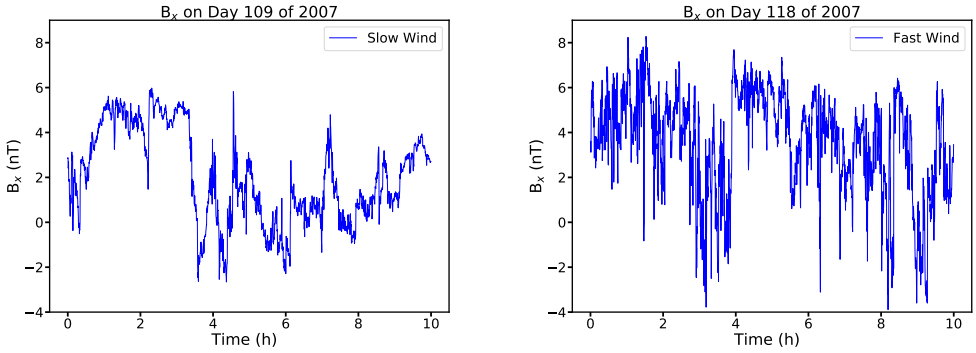

FIGURE 4.3: 10 hours of radial magnetic field (B_x) observations made in 2007, in the slow wind (left) and in the fast wind (right), taken from Krishna Jagarlamudi et al. (2019).

As the properties of the slow and fast solar wind are different, it is essential to analyze the statistical properties separately for the fast and slow wind. There is an upper limit on the time scales we can inspect, especially for the pure fast wind as WIND observes at best a few days of uninterrupted fast wind.

For our analysis, we define the solar wind based on the velocity as follows, slow winds as $v < 400$ km s^{-1} and fast winds as $v > 600$ km s^{-1}. The three orthogonal components of the magnetic field are expected to give qualitatively the same results (e.g. Wicks, Owens, and Horbury, 2010), therefore we focus on the radial component B_x only.

4.3 Results

4.3.1 Autocorrelation function (ACF) Analysis

As mentioned before, the general expression of the ACF (Equations (4.1) and (4.2)) which is a part of weak stationarity definition applies only for populations. Therefore, it is practically impossible to apply directly to the finite samples. We replace expectations by a finite sample averages (Bendat and Piersol, 2000; Papoulis and Pillai, 2002) and as our solar wind observations are discrete time signals, but not continuous time signals, we replace integrals by sums.

$$\mathrm{ACF}(t,\tau) = \frac{\langle (x(t) - m_x)(x(t+\tau) - m_x) \rangle_T}{\sigma_x^2} \tag{4.3}$$

where $x(t)$ is the magnetic field here, $\langle \cdots \rangle_T$ stands for sample averaging over a sample of duration T and m_x and σ_x^2 are respectively the mean and the variance of the sample.

For the stationarity analysis the separation between the populations and finite samples is not trivial, and has several consequences (see for example Kasdin, 1995). Specifically, the sample duration T comes in as an extra parameter and there is a need to determine which part of the observed ACF reflects the properties of the sample and which part is influenced by the choice of the estimator.

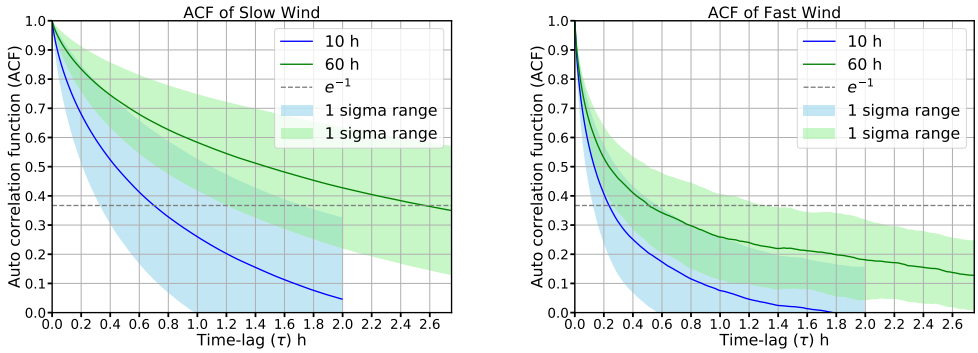

FIGURE 4.4: Autocorrelation function of the B_x component at 1 AU for slow and fast solar wind for sample duration of 10 h and 60 h, along with their dispersion, which is expressed by $\pm$ one standard deviation, taken from Krishna Jagarlamudi et al. (2019).

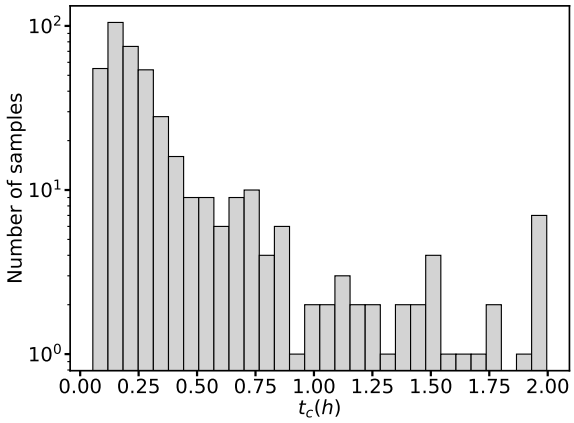

FIGURE 4.5: Histogram of the correlation time t_c estimated using 420 intervals of 10 hours each using the e-folding method, in the fast solar wind, taken from Krishna Jagarlamudi et al. (2019)

As Bendat and Piersol (2000) suggest, we can relax the definition of weak stationarity and consider a slightly weaker version of it. This is based on determining whether the mean and ACF vary significantly from one time interval to the other. However, we do not have a proper reference value to know what we can suggest as a significant change. This explains why it is so difficult to formulate a rigorous statistical test for stationarity.

Therefore, in our study we follow an exploratory approach, we investigate how the ACF of the solar wind varies with occurrence time t and sample duration T.

The typical integral time scales of solar wind turbulence is expected to be around 1-2 hours, therefore we need to analyze a solar wind interval typically of 10 hours to have a reasonable estimate of ACF at different time lags. We have carefully chosen non-overlapping intervals of various sizes and estimated the ACF of each of them.

We have analyzed 4409, 2026, 875 and 508 intervals with respectively 10, 20, 40 and 60 hours of slow wind and for the case of fast solar wind we have analyzed 420, 163, 51 and 23 intervals respectively, between the years 2006 and 2016. Since

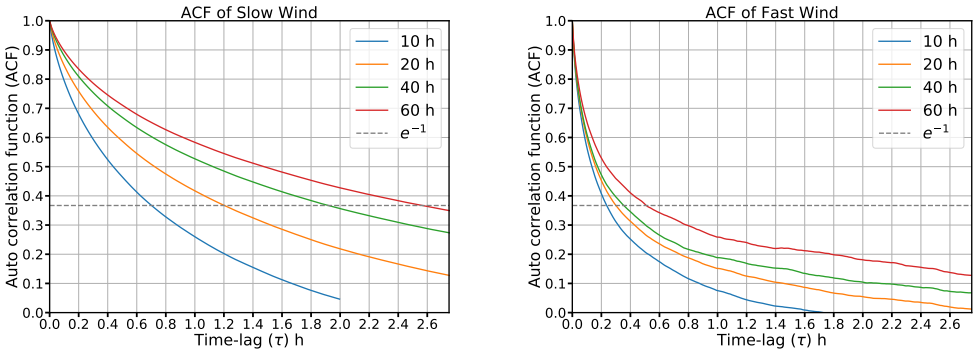

FIGURE 4.6: Autocorrelation function of the B_x component at 1 au for different sample durations of 10 h, 20 h, 40 h and 60 h, for slow and fast winds. The dashed horizontal line represents the e^{-1} value, taken from Krishna Jagarlamudi et al. (2019).

the WIND spacecraft is located in the ecliptic plane, it spends more time in the slow wind and therefore we have a larger number of slow wind intervals.

Figure 4.4 displays the average ACF obtained for both solar wind regimes for samples of 10 hours and 60 hours duration along with the standard deviation, which quantifies the dispersion of the ACF values at different time lags.

There are two important results. First, there is a considerable difference between the ACFs estimated from intervals lasting for 10 and 60 hours. Second, there is a large dispersion of the ACFs, which indicates that for a given lag τ, the values of the ACFs vary significantly from one sample to an another. Both the above results creates a doubt on the physical interpretation of the ACF values.

Magnetic field fluctuations in the solar wind can be approximated by a random first order Markov process in which future state of the system does not depend on the past history, but solely on the present state. For solar wind model, whose dynamics can be approximated by a Markov process, the ACF of the fluctuations should be decaying exponentially (Papoulis and Pillai, 2002).

$$ACF(\tau) = \frac{C(\tau)}{C(0)} = e^{-|\tau|/t_c}. \tag{4.4}$$

The correlation time (t_c) is usually estimated by means of the e-folding technique, i.e. by considering the time it takes for the ACF to drop to e^{-1} of its maximum value (Matthaeus, Smith, and Oughton, 1998; Weygand et al., 2013; Ruiz et al., 2014). However, ACFs seldom show a pure exponential decay, and therefore the estimates based on e-folding technique are approximate ones. Although there are limitations, the e-folding estimator is widely used one and we use it in our work for the sake of continuity.

In Figure 4.4 the correlation time is given by the intersection between the ACF curve and the horizontal dashed line (which represents the e^{-1} value). We infer that the correlation time is longer in the slow wind than in the fast solar wind and the values are varying in the range of one to two hours. These observed properties are not new, they have been already documented (Weygand et al., 2013; Isaacs, Tessein, and Matthaeus, 2015a).

The important point to note is that due to the large dispersion in the ACFs there is also a large dispersion of the correlation time t_c. This is shown in Figure 4.5 using

a histogram of t_c, which is calculated using 10-hour samples of the fast wind. The observed large dispersion can be due to poor convergence of our estimator of the ACF or may be due to the lack of stationarity or by both. At this stage we cannot come to a conclusion.

To show how the duration T is affecting the ACF, we show in Figure 4.6 the ACF for slow and fast solar wind regimes with $T = 10, 20, 40$ and 60 h. A noticeable result is the gradual change in the ACF with sample duration with no clear evidence for convergence.

The observed behaviors are in contradiction to the the standard beliefs, as one would normally expect the ACF to converge toward a fixed function when the sample length becomes considerably longer than the correlation time. However, in our analysis we observe that even with 60 hours of observations there is no evidence for convergence.

Isaacs, Tessein, and Matthaeus (2015a) in a statistical study observed a similar lack of saturation. This is shown in the Figure 4.7 where we can observe how the correlation length is increasing with the interval of averaging (sample size) for different wind velocities. The authors suggest the presence of long range correlated structures as one of the possible reasons. Moreover they suggest to consider a sample size of the order of 10 to 20 h to avoid observed effect. This, however, is against one of the major assumptions of stationarity, which is the invariance versus translation in time.

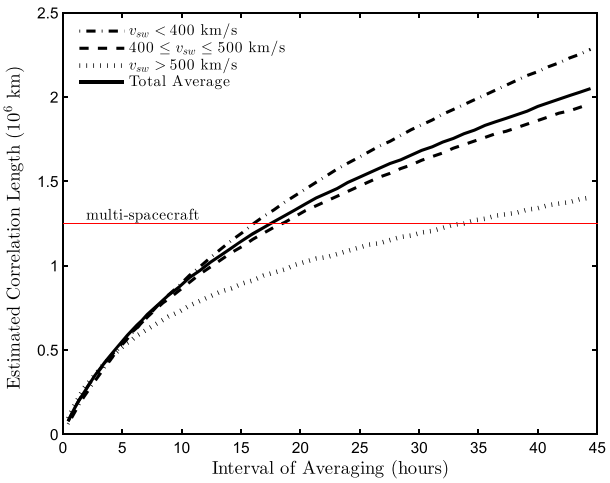

FIGURE 4.7: Illustration of the change in correlation length with respect to the wind velocity and the duration of the sample considered, taken from Isaacs, Tessein, and Matthaeus (2015b).

There can be arguments that intervals of 60 h are not long enough to properly estimate the ACF. For this reason we have extended our analysis to intervals of size 300 h. However their availability is confined to the slow solar wind only. In Figure 4.8 we can observe that there is no evidence for convergence even using a long records.

At this point, we can come to a conclusion that the ACF estimates for fast or slow solar winds cannot be meaningfully estimated. This questions the physical meaning of correlation times that are usually inferred from the solar wind.

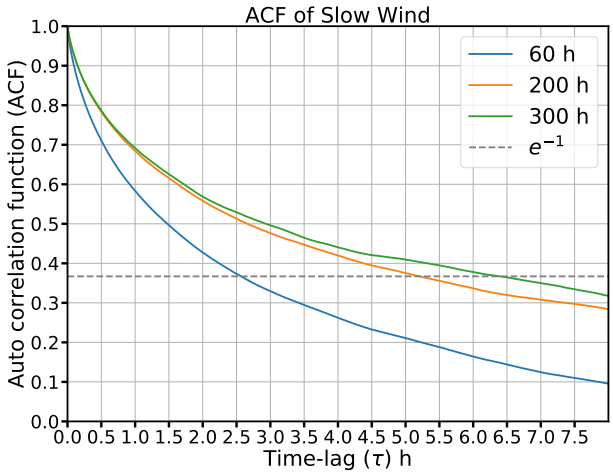

FIGURE 4.8: Similar to Figure 4.6 but for longer samples of the solar wind of up to 300 hours.

To better understand the origin of the above observed properties and their connection to stationarity, let us now connect the power-law scalings observed in the magnetic field power spectral density of the solar wind.

4.3.2 Relating the ACF observations to the power spectral density

From our study on turbulence in Chapter 3, we observe that power law scalings in the PSD of the solar wind are omnipresence. The important result to be highlighted is the presence of double power law $P(f) \propto f^{\gamma}$, where spectral index γ approaches 1 at low frequencies and is closer to 5/3 (Kolmogorov) in the inertial range both in the slow and fast solar wind. Similar power laws have been observed by many in the solar wind (Bruno and Carbone, 2013a, and references therein) and their spectral indices have been abundantly discussed.

Notice that two naming conventions are used in the literature: $P(f) \propto f^{\gamma}$ and $P(f) \propto f^{-\gamma}$. In the present context it is more common to use the first one, while in Chapter 3 we used the second naming convention. Eventually, only the magnitude of γ matters.

Multiple studies have been performed on the analytical properties of the ACF of a time series whose PSD is a power law with spectral index γ (Keshner, 1982; Kasdin, 1995; Hooge, Kleinpenning, and Vandamme, 1981; Hooge and Bobbert, 1997).

From the works of Kasdin (1995) we can show that if the ACF is calculated over a sufficiently long time interval $t \gg \tau$, so that we can assume that the transients have disappeared then the autocovariance is approximately given by:

When $0 < \gamma < 1$,

$$C(t, \tau) = C(\tau) \propto |\tau|^{\gamma - 1}. \tag{4.5}$$

When $\gamma = 1$,

$$C(t, \tau) \propto \log 4t - \log |\tau|. \tag{4.6}$$

When $1 < \gamma < 2$,

$$C(t, \tau) \propto t^{\gamma - 1} - c|\tau|^{\gamma - 1}, \tag{4.7}$$

where, $c > 0$ is a constant. These asymptotic results apply to the autocovariance. To convert them into autocorrelations we normalize them by $C(t, \tau = 0)$.

The important result is the presence of an offset which is dependent on t. This offset is unexpectedly large when $1 \leq \gamma \leq 2$, i.e. for spectral indices that we normally encounter in solar wind turbulence.

Importantly, the characteristic scale we infer from the decay of the ACF is dependent both on the underlying physics and on the observing window, and in this sense also on sample duration T.

We will investigate the above observed properties using the synthetic time series in the coming section.

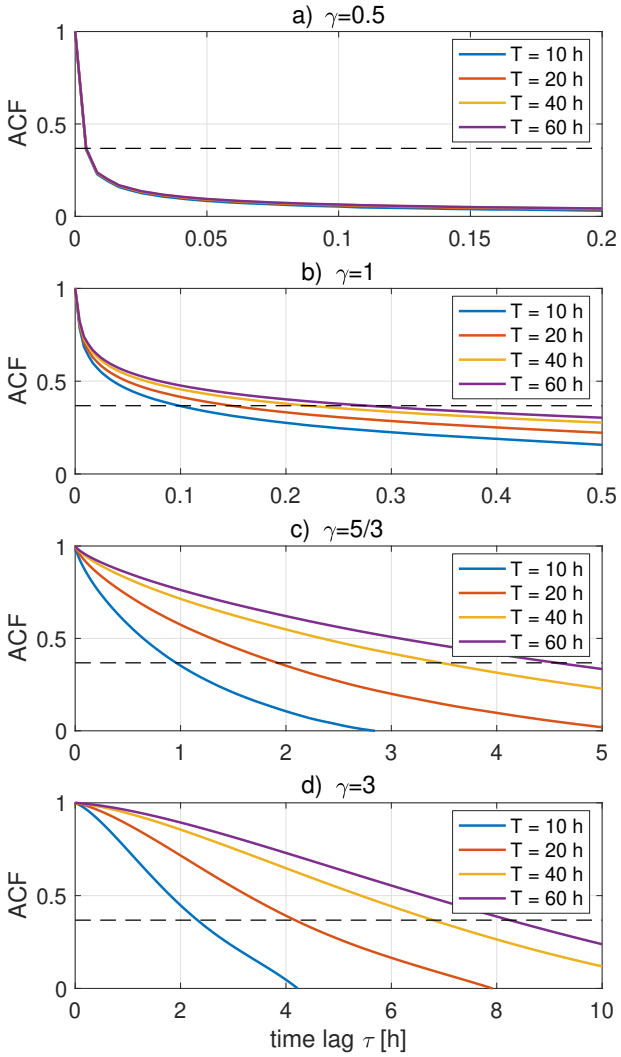

FIGURE 4.9: Autocorrelation function of synthetic data for four different spectral indices, from top to bottom: $\gamma = 0.5$, $\gamma = 1$ $\gamma = 5/3$ (Kolmogorov model) and $\gamma = 3$. All plots show the average ACF for 1000 realizations that have the same length as the original data in Figure 4.6. The intersection with the horizontal dashed line defines the e-folding time. Figure taken from Krishna Jagarlamudi et al. (2019).

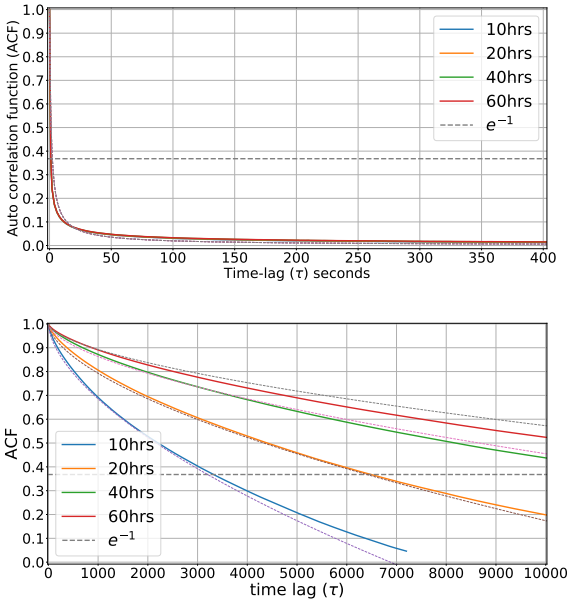

FIGURE 4.10: Autocorrelation function of synthetic data for $\gamma = 5/3$ and $\gamma = 0.5$ for sample duration of 10, 20, 40 and 60 h, showed in normal lines and the dotted curves are Autocorrelation function drawn using the analytical functions.

.

4.3.3 Synthetic data analysis

To demonstrate the affect of self-affinity on the auto-correlation function, we created synthetic magnetic field data whose PSD is a power law with a spectral index we are interested in. We will consider the case when the PSD consists of a single power law.

The synthetic data is computed as follows, first we Fourier transform a sequence of white noise, apply the spectral index we are interested in, and then invert the Fourier transform (Kasdin, 1995). The sampling of the sequences are such that they equal the solar wind records, i.e. 14400 samples for 60 hours of WIND data. Using the suggested approach, 1000 records that imitate the properties of 10, 20, 40 and 60 hours of solar wind are generated, which enable us to carry out statistical tests. We can improve our approach by imposing a condition that the magnetic field and the synthetic data will have the same probability distribution function, using the surrogate data technique (Theiler et al., 1992). However, as our concern is only with the second order moments, we do not impose this.

In Figure 4.9, we outline the key results by showing the average ACF of 1000 synthetic time series of four different spectral indices: $\gamma = 0.5, 1, 5/3$ and 3. A noticeable property of the ACFs is their dependence on the spectral index: the larger the γ is, the slower the ACF decays, and the longer the memory of the system is. The other important result in which we are interested in is the difference between the ACFs estimated from sequences of T=10,20,40 and 60 hours. These results confirm what had been observed with real magnetic field data, i.e. there is lack of convergence even with the increase of the length of sequence. This is clearly evident when the $\gamma = 1$ and $\gamma = 5/3$ and this is in agreement with the analytical expressions given in Equations (4.5) to (4.7). For $\gamma = 3$, we find a similar behavior. On the contrary for $\gamma = 0.5$, the ACF seem to collapse to fixed function, irrespective of the length of the

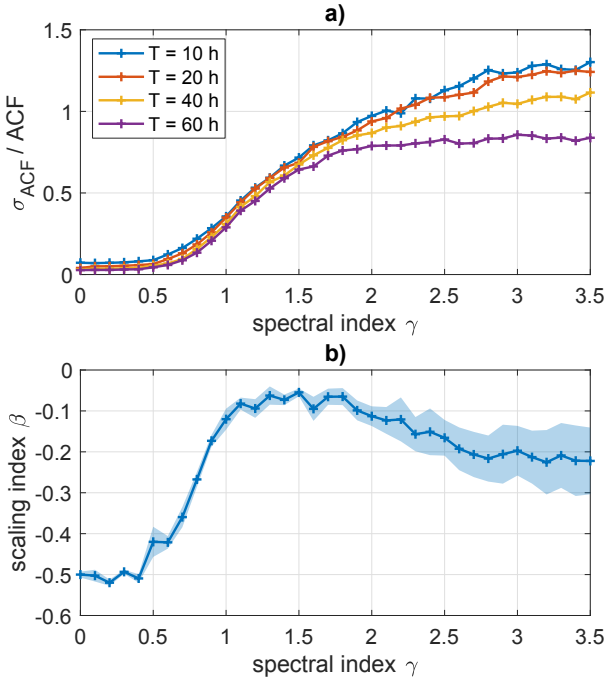

FIGURE 4.11: Upper plot: relative standard deviation of the ACF $\sigma_{ACF(t_c)}/ACF(t_c)$, measured at the *e*-folding time for synthetic data at different values of the spectral index $|\gamma|$. Lower plot: scaling index β and its confidence interval ($\pm$ one standard deviation), estimated from samples of duration $T = 10$, 20, 40 and 60 hours. An ensemble of 1000 realizations was used to estimate these quantities, taken from Krishna Jagarlamudi et al. (2019).

sequence. In this particular case the ACF is well defined.

Using the synthetic data of different lengths for the case of $\gamma = 5/3$ and $\gamma = 0.5$ and the analytical functions (equation 4.5 and 4.7)for the case of $0 < \gamma < 1$ and $1 < \gamma < 2$, we show the exponent index and the interval length dependence in the Figure 4.10. You can observe how for the non-stationary case of $\gamma = 5/3$, the analytical dotted curved follows the synthetic data curves and verifies the sample length and exponent dependence. Where as for the stationary case of $\gamma = 0.5$ there is no interval length dependence and analytical function too shows the same.

We tested whether the dispersion in the ACF can be reduced by using longer records, for this we simulated an ensemble of 1000 self-affine records for a given spectral index γ and for each of them we estimate the ACF by using intervals of duration T =10, 20, 40 and 60 h. Then we estimate the standard deviation $\sigma_{\mathrm{ACF}(t_c)}$ of the ACF at the e-folding time.

From the synthetic data analysis we have two important results, which are summarized in Figure 4.11. First, we can see how the standard deviation of the ACFs gradually increases with the spectral index, especially once the spectral index (γ) exceeds one. This result show that there is high uncertainty in ACF value when the power law is steep.

It would be acceptable to have high standard deviation, if this uncertainty could be reduced by further increasing T.

Bartlett (1946) has shown that the standard deviation should be approximately decreasing as $\sigma_{\mathrm{ACF}} \propto T^{-1/2}$ for a stationary process. For our case we consider a

general scaling $\sigma_{ACF} \propto T^{\beta}$ and investigate how the value of β is varying for different spectra indices. Values $\beta >> -1/2$, imply a slow convergence and we need very long records to reduce the uncertainty. Figure 4.11 shows that the scaling with $\beta = -1/2$ is observed only for small spectral indices with $\gamma < 1$. For power laws which are steeper, β rapidly approaches zero, which means that considerably longer records are required to achieve the same reduction in uncertainty.

This result explicitly shows why a processes with spectral indices above one require an extra care (Beran et al., 2016). Notice that the value of β increases again when $\gamma > 2$, but still the uncertainty remains prohibitively large.

The major uncertainty arises for spectral indices which fall between 1 and 2. These are the indices which coincide with the f^{-1} and inertial range of solar wind turbulence. Therefore, we can understand that ACF estimates in the solar wind have large uncertainties associated with them and they cannot be mitigated with the increase in the sample duration. To conclude, with our short and generalized synthetic data analysis we can understand that there are several pitfalls that can easily lead to miss interpretation of the correlation time.

Finally, a question arises, whether ACF can be meaningfully interpreted for physical purposes ? Yes, the ACF even with a large uncertainty is useful for comparative studies. Example, taking same sample duration of the fast and slow wind shows that the correlation times are higher in slow wind compared to fast wind and this is a physically acceptable result. However, it is not that meaningful to use ACF for the measurements of absolute values and importantly ACF decay rate cannot be used to make physical interpretations.

4.4 Discussion

As we have understood that formal existence of weak stationarity cannot be proven from solar wind observations, the right question is whether we have enough evidence to draw conclusions on stationarity of the solar wind. As suggested before, the main signature of non-stationarity is to verify whether there is a significant variation in the ACF values of the solar wind. Our observations first show a clear lack of convergence of the ACFs, ACF fails to saturate with the increase of the sample size (duration of the observations). Along with the lack of saturation is the systematic increase of the correlation time with the sample size. For example in the slow solar wind, the value of the correlation time is around 0.7 h for intervals of 10 h and around 7 h when intervals of 300 h are considered. The correlation time, which is normally interpreted as the integral scale, keeps on increasing. These results create a serious doubt on how meaningful the ACF estimates and also the integral scale values from solar wind observations are.

Practically speaking, the problem of ACF convergence directs to the in-consistency of the estimator and only provides an in-direct proof of non-stationarity. However, from the observational evidence of power laws in the power spectral density of the magnetic field we can derive theoretical expressions for the ACF (Equations (4.5) to (4.7)) and infer that ACFs may or may not converge depending on the value of the spectral index γ . Therefore, we can understand that the lack of convergence we observe is not just a property of the estimator, but also originates from the non-stationarity of the population.

The second important result is the presence of large variance of the ACF estimates even with large samples, as shown in the Figure 4.4. The presence of such a

large dispersion raises a serious concern on our ability to make a meaningful physical conclusions. These large uncertainties are not an issue as long as they can be reduced by considering longer time intervals. However, Figure 4.11 shows that long time intervals help only when the spectral index is relatively small, i.e. for $\gamma < 1$. For spectra that are steeper, typically in the inertial range, the uncertainty of the average ACF cannot be notably reduced by increasing the duration T. This effect even exists for spectral indices corresponding to the sub-ion range of solar wind turbulence, for which $\gamma > 2$. For spectra that are steep, longer durations might help to reduce the standard deviation, however their remain a large dispersion of the ACFs.

At very long time scales of weeks or more we expect the f^{-1} scaling of the PSD to break down to prevent the infrared catastrophe; the amount of energy that is injected into the solar wind cannot grow forever.

The picture that comes out from these results is the presence of scale-dependent non-stationarity, i.e dependent on the PSD spectral index of the scales we are working with. A firm evidence for the signatures of non-stationarity in the inertial range and in the f^{-1} range is found. These are the frequency ranges in which the ACF shows a high variance and converges slowly.

Another significant result is that we show how improbable it is to have a meaningful characteristic scales from the ACF in the f^{-1} and inertial ranges. The integral scale length cannot be rightly inferred from the ACF because its value other then depending on the underlying physics, but also depends on the duration of the time intervals and on the number of intervals used for averaging.

Considering longer intervals or increasing the number of samples offers no solution, it just creates a false impression that the estimator is more accurate. This deceptive result questions the validity of correlation times that are usually published in the literature. The outcome of our analysis is that we should stay away from working with the ACF to obtain accurate measurements of correlation times or the correlation lengths.

The ideal tool to study self-affine processes such as the ones that are encountered in the solar wind is the discrete wavelet transform, as it is self-affine by construction (Mallat, 2008). Instead of ACF, we can use the wavelet transform to accurately determine the the size of the eddy, non-linear time when the non-linear cascade begins.

4.5 Conclusion

In the study presented here, using the ACF as a tool we have revisited the problem of weak stationarity in the solar wind. Even though ACF is not designed to test the stationarity problem, its sensitiveness to stationarity and its regular use in solar wind studies motivated us in using ACF as a tool.

We observe a signature of non-stationarity, both in the slow and in the fast solar wind although no definite proof can be given. We explain that the signatures of non-stationarity arise in specific frequency ranges only, which makes the question of whether the solar wind is stationary or not ill-posed.

The outcome of our analysis is based on the observation of power-law scalings in the power spectral density (PSD) of the magnetic field using the *WIND* spacecraft at 1 AU. Using the analytical expressions we first show how the ACF is affected by non-stationarity when the spectral index of PSD is between 1 and 2. The ACFs suffer from high variance and the convergence to a stable mean value is slow, such that the estimated ACFs from finite observations are not meaningful.

Similarly, the correlation time which is normally inferred from the ACFs is most likely affected by the length of the observed intervals rather than by any physical timescale associated with the turbulent eddies. These problems have been often overlooked and this highlights the need for a systematic validation of measurements using the ACF.

The problem of convergence also exists for spectral indices greater than 2, i.e., in the sub-ion and in the electron kinetic range, therefore this range should also be considered as non-stationary.

We expect that for very long timescales, usually of the order of several days to weeks, stationarity may set in. This is because in the solar wind the spectral energy content cannot keep on growing indefinitely at very low frequencies.

Non-stationarity of the solar wind has many implications on the proper interpretation of the statistical analysis usually performed in the solar wind turbulent studies. Non-stationarity importantly implies that the ergodicity condition can not be valid. This cautions the solar wind turbulence community in making the assumption that time average is similar to the average over the probability space or the ensemble average.

Based on our results we recommend avoiding using the non-stationarity sensitive ACF as an estimator of large-eddy size, even for the records which exceed the correlation time by a considerable amount. A good alternative can be working with wavelet transform, as it is ideally suited for the study of self-affine processes as encountered in the solar wind.

Our analysis guides the solar wind community to know at which scales the non-stationarity would be dominant by looking into the spectral index of the power spectra of the physical parameter we are working with. If the spectral index goes below 1 we expect that at those scales we have stationarity. The conventional method of using the ACF could be applicable in the scales when the stationarity dominates (PSD spectral index less than 1). These scales would be dependent on the wind type and the distance. We cannot provide definitive scale yet, as to date we do not have a clear indication of when the stationarity dominate and the scales also vary with the variable to variable. This is a topic to be focused on in the future. However, we can suggest that our analysis of interpreting non-stationarity using the PSD spectral index of the data lays a good path for the future work.

Nevertheless, we have a caveat in our study. Here, we are confined to address the problem of weak stationarity only, which considers first- and second-order moments only of the wave-field. Higher-order moments are not considered as their assessment is increasingly difficult and beyond the scope of our study. However, these moments are exactly the ones that give insight into the existence of phase couplings, which may give rise to shocks, compressions, rapid rotations or some other coherent structures which are inherent in the solar wind.

4.6 Résumé en français: Non-stationnarité dans le vent solaire

Ce chapitre est fortement inspiré de l'article (Krishna Jagarlamudi et al., 2019).

Les études statistiques basées sur des observations in-situ du vent solaire font généralement hypothèse de la stationnarité du vent. La stationnarité est en effet une condition nécessaire pour pouvoir appliquer ombre d'outils standards d'analyse de données. La stationnarité implique une invariance stricte par rapport à toute translation dans le temps. Dans la pratique, cette hypothèse s'avère très difficile

à vérifier. Du coup, on préfère recourir à la notion de "stationnarité faible", qui consiste à vérifier l'invariance dans le temps des moments statistiques d'ordre un et deux. Ou encore, que la fonction d'autocorrélation (ACF) est indépendante de l'intervalle de temps pour lequel elle est estimée.

L'ACF est couramment utilisée pour étudier le vent solaire. Cette fonction tend généralement à décroître avec la durée; cette décorrélation permet de quantifier des échelles de temps caractéristiques du vent solaire. Pour des mesures du vent solaire obtenues dans le régime inertiel (pas de temps allant de la seconde à plusieurs heures) le temps de décorrélation est de l'ordre de l'heure et est appelé temps inertiel. Ce dernier marque la transition entre régime inertiel et le régime en f^{-1} qui est dominé par des structures cohérentes. Paradoxalement, à quelques rares exceptions près, l'ACF est toujours appliquée sans vérification de la condition de stationnarité.

Motivés par la nécessité de comprendre si et comment les mesures d'autocorrélation dans le vent solaire sont affectées par la non-stationnarité présumée de celle-ci, nous avons analysé divers jeux de données expérimentales et synthétiques. Les premiers sont des mesures du champ magnétique interplanétaire obtenues par le satellite WIND. Les secondes sont des séries temporelles dont la densité de puissance spectrale suit une loi de puissance avec un indice spectral donné, comme observé dans le vent solaire. Pour chacun de ces jeux de données nous avons estimé l'ACF pour des séries temporelles de durées différentes. Nous avons ensuite comparé les résultats à ceux issus de la théorie.

De cette étude nous concluons que l'ACF est un estimateur à éviter en raison de son biais et de sa forte variance. Quand la densité de puissance spectrale de la variable observée suit une loi de puissance d'indice spectral $\gamma < 1$, l'ACF converge rapidement vers une valeur fixe dès lors que l'intervalle étudié dépasse d'un ordre de grandeur le temps inertiel. En revanche, pour $\gamma > 1$, la convergence ralentit fortement au point de rendre impossible l'estimation de l'ACF, même quand on dispose de longues séries temporelles. Par ailleurs, la variance de l'estimateur croît avec γ.

Ces résultats surprenants remettent en question notre capacité à tirer des conclusions physiques à partir de l'analyse de l'ACF. Dans le régime inertiel du vent solaire l'indice spectral est compris entre 1 et 2. Or dans cette plage le bias et la variance sont justement élevés. Cet effet est d'autant plus sournois que la fonction d'autocorrélation présente souvent une allure régulière qui peut faire croire que le résultat est précis. Notre résultat explique a posteriori la forte dispersion de valeurs obtenues par des auteurs différents dans des conditions semblables du vent solaire. La meilleure alternative à une analyse par ACF est une analyse spectrale ou par ondelettes, qui sont moins sensibles aux écarts à la stationnarité.

Quant à la question de la stationnarité faible, nous concluons que celle-ci est mal posée puisqu'elle dépend des échelles de temps considérées. Pour le régime inertiel ainsi que pour le régime f^{-1} le vent solaire n'est clairement pas stationnaire.

Chapter 5

Whistler waves in the inner heliosphere

5.1 Introduction

Whistler waves are right handed (with respect to the mean magnetic field) circularly polarized waves whose frequency range falls between the lower hybrid frequency (f_{LH}) and electron cyclotron frequency (f_{ce}) (Stenzel, 1999). Whistlers are the most probable electromagnetic modes to be observed in this range (Gary, 1993). Therefore, the range between f_{LH} and f_{ce} is usually termed as *whistler range*, shown in Figure 5.1 using simplified dispersion relation curves. In this Figure 5.1 we can also see the dispersion relations for other waves and see how distinctive is the whistler range.

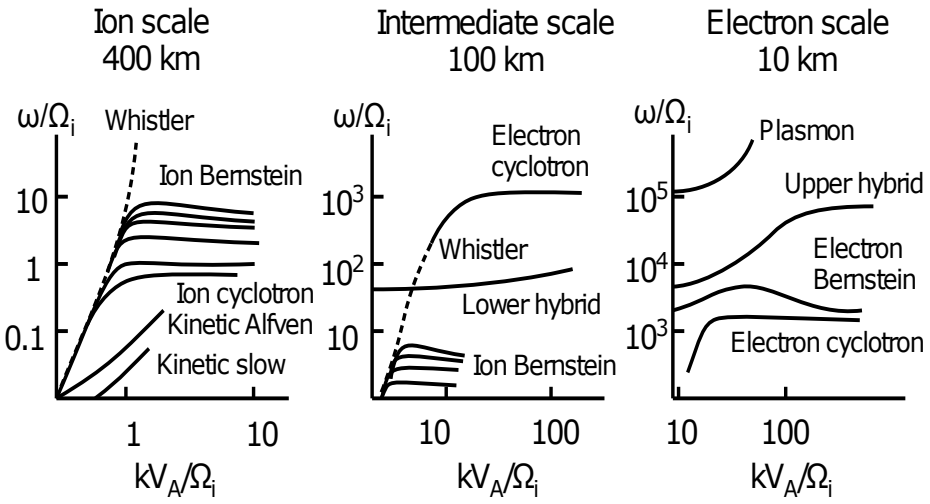

FIGURE 5.1: Illustration of the dispersion relations from ion to electron scales for different waves, taken from Narita (2017).

How are these whistler waves generated? The primary source of energy in the pristine solar wind are instabilities that are related to the electron distribution function, such as whistler temperature anisotropy instability, which depends on the ratio between perpendicular and parallel electron temperatures $T_\perp / T_\parallel > 1$. Another source is the whistler heat flux instability, which develops when the heat flux is mainly carried by the anti-sunward movement of the halo electrons relative to the sunward moving core (Gary and Feldman, 1977; Breneman et al., 2010).

Whistler waves are thought to provide a significant contribution in the control of electron properties in the solar wind and therefore have been widely studied to better understand global solar wind thermodynamics and energy transport. For example whistlers play a significant role in the evolution of solar wind velocity distributions through the pitch angle scattering of Strahl electron population (Vocks et al., 2005; Vocks, 2012; Kajdič et al., 2016), which in turn is expected to affect the halo electron population, and therefore the total electron dynamics. Whistler waves are expected to suppress the heat flux below a certain threshold (Gary et al., 1994; Gary, Skoug, and Daughton, 1999). Whistler waves, through the heating and acceleration of high energy electrons could provide a mechanism for the continuous formation of suprathermal electrons in the corona (Vocks and Mann, 2003; Vocks, 2012). In the magnetosphere, whistler waves have received considerable attention because of their role in acceleration and precipitation of particles in the radiation belts (Artemyev et al., 2016).

In our studies, we focus on whistler waves in the solar wind and we mention a few of the important whistler wave observational studies. Among the studies that gave a piece of clear evidence for the existence of whistler waves in the solar wind is the one by Zhang, Matsumoto, and Kojima (1998), using magnetic field observations made by the *Geotail* spacecraft. Figure 5.2 shows the waveform, the power spectral density (PSD) and a hodogram of the observed large-amplitude whistler waves. The authors suggest that observed whistlers are short-lived, propagate mainly parallel to the magnetic field and in anti-sunward direction. Breneman et al. (2010) studied large-amplitude whistler waves at the stream interaction region using high-resolution electric field data from *Stereo* and observed that whistlers were propagating obliquely and suggest the requirement of sudden disturbances of the solar wind magnetic field and plasma for their presence. Wilson et al. (2013) investigated whistler waves downstream of super-critical interplanetary shocks and suggest that the whistler mode waves might be driven by a heat flux instability and cause perpendicular heating of the halo electrons. These authors have also observed the presence of waves which are a mixture of both lower hybrid and whistler mode waves and observed in the whistler range.

One of the initial extensive studies on whistlers in the pristine solar wind is done by Lacombe et al. (2014) who using magnetic field observations from the *Cluster* spacecraft and studied the intervals with long intermittent whistler wave activity (10 min). Using the simultaneous electron heat flux measurements they have tried to show that whistler heat flux instability is responsible for the observed whistler activity. Stansby et al. (2016) identified large amplitude whistler waves by comparing the experimental measurements from the *Artemis* spacecraft with the theoretical dispersion relations and Tong et al. (2019b) studied the simultaneous field and particle measurements when the whistler waves are observed and explained the importance of electron halo temperature anisotropy on whistler wave generation. Quite recently Tong et al. (2019a) using the 3 years of *Artemis* spacecraft data have performed a statistical study of whistlers at 1 AU and shown that occurrence probability of whistlers is highly dependent on the electron temperature anisotropy.

One of the earliest studies of whistlers in the inner-heliosphere is the work by Beinroth and Neubauer (1981) who used the PSD of the magnetic field measured by *HELIOS* 1 and interpreted the shape of the broadband spectrum as evidence for whistler waves. It later became evident that these are not whistler waves and whistler waves observed to date are monochromatic and occupied a narrow frequency band but not broad band. These waves are convected past the spacecraft by the moving solar wind so that their true velocity (in the plasma frame) differs

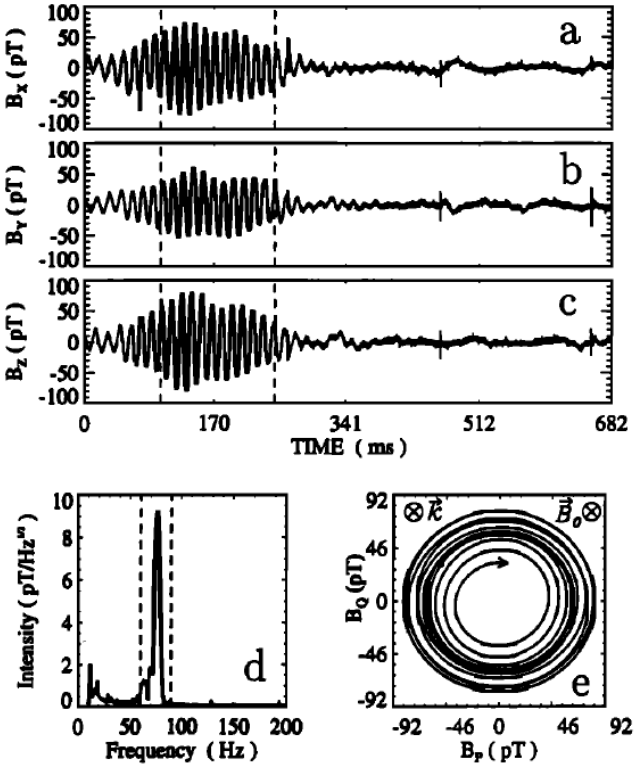

FIGURE 5.2: Waveforms of the magnetic field in the presence of whistler waves: panels 'a', 'b' and 'c'. In panel 'd' their corresponding PSD and panel 'e' the hodogram are shown. Measurements are made in the solar wind using the *GEOTAIL* satellite. Figure taken from Zhang, Matsumoto, and Kojima (1998)

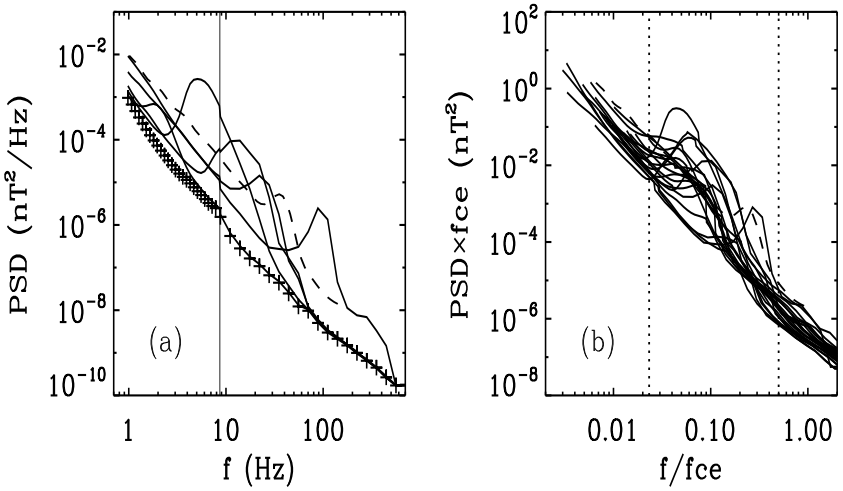

FIGURE 5.3: Example of magnetic field PSD measured at 1 AU during the presence of whistler waves using the *CLUSTER* satellite. On the left: frequencies expressed in the spacecraft frame. On the right: frequencies normalised with respect to f_{ce}. Figure taken from Lacombe et al. (2014).

from the observed one (in the spacecraft frame) by a Doppler shift. In the plasma frame, the frequency is expected to be located between the lower hybrid frequency $f_{LH} = \sqrt{f_{ce} f_{ci}}$ and the electron cyclotron frequency f_{ce} (Stenzel, 1999). At 1 AU, and in the spacecraft frame, the corresponding frequencies range between 1 and 100 Hz. An example of the spectral signature of whistler waves is given in Figure 5.3.

Another characteristic feature of whistler waves is their right-handed circular polarisation, which is often the key to their unambiguous identification (Alexandrova et al., 2012; Lacombe et al., 2014; Roberts et al., 2017). For these reasons it is important to have access to all three components of the magnetic (or electric) field. Alternatively, if only Fourier spectra are provided, the full 3×3 spectral matrix is required for unambiguous identification.

Meanwhile, the first and simplest criterion for detecting the possible presence of whistler waves is a local concentration of spectral power in the frequency range where such waves are expected to occur. Such bumps can easily be detected in Figure 5.3. In the following, we shall rely on spectral data from the search-coil of *HELIOS* 1, for which only the PSD of two components is available, which excludes polarisation measurements. For that reason, we can only rely on the presence of a "bump" or inflexion point in the PSD to detect whistler waves, assuming that the spectral shape without whistler waves is featureless.

In what follows we shall be focusing on the study of large amplitude whistler waves in the inner heliosphere ($0.3 < R < 1$ AU) using search-coil data from *HELIOS* 1. Surprisingly, whistler waves in the inner heliosphere have received relatively little attention since the initial short study by Beinroth and Neubauer (1981), who essentially interpreted changes in the shape of the PSD as evidence for whistler

waves. Considerably more evidence has been accumulated since near 1 AU. In comparison, the major advantage of the *HELIOS* 1 mission is that it allows us to investigate the radial dependence of the properties of these waves. As of today, this radial evolution is unknown, while it may shed new light on the generation of whistler waves. The main drawback of these data is the incomplete spectral matrix which prohibits the assessment of the polarisation and therefore makes it impossible to detect such waves in an unambiguous way. For that reason, in what follows, our sole criteria for detecting whistler waves will be an excess of spectral power (i.e. a spectral bump) and the frequency range in which this bump occurs.

5.2 Data used for the whistler wave analysis

Our magnetic field observations come from the search-coil magnetometer (Dehmel et al., 1975) onboard *HELIOS* 1. Most of our data are time series of the spectral density of the B_y component of the sensor (located in the ecliptic plane) that were collected during the first months of 1975 with an 8-second cadence. Although the instrument worked longer than that, the remaining data seem to have been lost.

The working principle of the search-coil magnetometer (SCM) has already been explained in Chapter 2. The spectral density of the B_y component is measured in 8 logarithmically-spaced frequency bands. Their central frequencies are 6.8 Hz, 14.7 Hz, 31.6 Hz, 68 Hz, 147 Hz, 316 Hz, 681 Hz, and 1470 Hz. From these, we obtain the PSD by squaring the spectral density. Although the B_z component (perpendicular to the ecliptic plane) is also measured, it is more affected by stray magnetic fields and so we discard it. The SCM has two data products: mean and peak magnetic field spectral density in the considered time interval. We use mean data products for the analysis as it is representative of the whole time interval, for removing the irregularities in the data products, we have followed the similar steps suggested in the Chapter 2.

An important issue is the noise level, which is needed to determine to what degree the observed PSD is affected by instrumental noise. For the noise level we use the values provided by Neubauer, Musmann, and Dehmel (1977) and only consider values of the PSD that exceed the background noise level by at least a factor of 2[1]. With this, the total number of spectra is 246543.

For the physical interpretation of our data, we use electron densities and electron temperatures from the E1 instrument onboard *HELIOS* 1 that were provided by Štverák et al. (2009). Unfortunately, these observations have a lower time resolution of 40.5 s and are less regularly available. For the sake of our analysis we divide the observations into the fast solar wind (bulk velocity $v > 600$ km/s) and slow solar wind (bulk velocity $v < 500$ km/s) as we did in the previous chapters.

[1] In Chapter 3 we use a higher factor of 3 because of the more stringent signal-to-noise requirements.

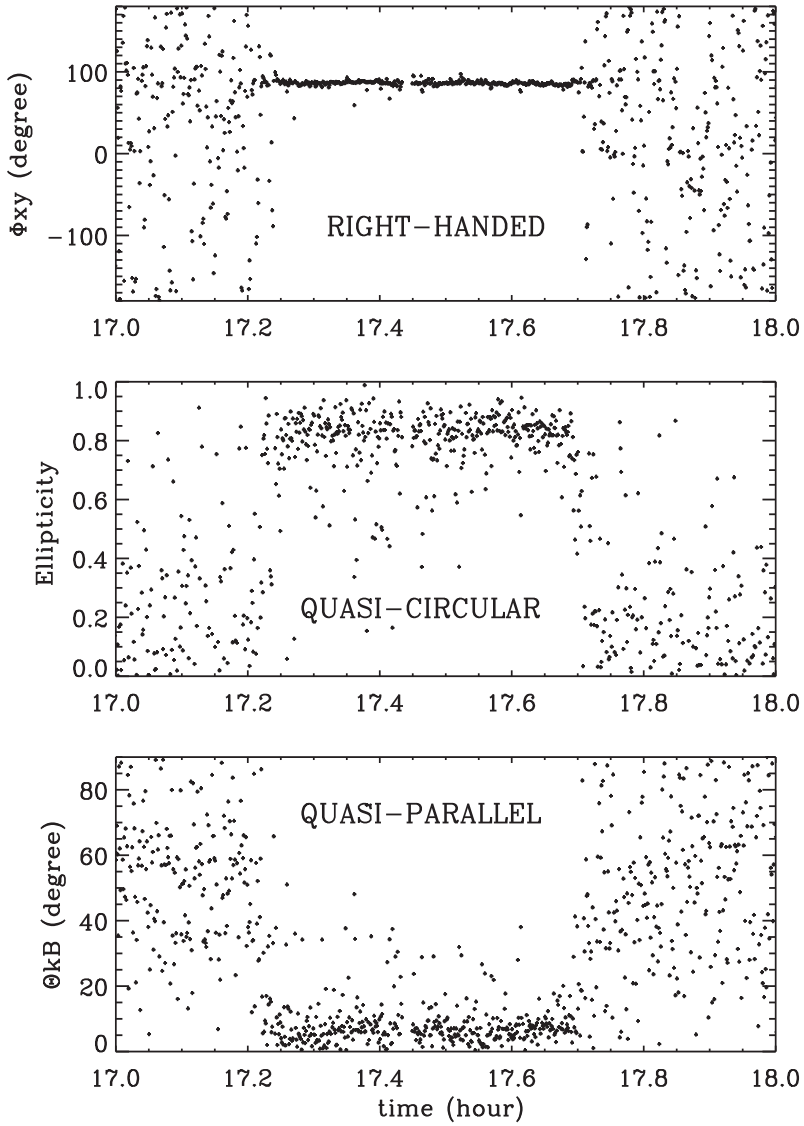

FIGURE 5.4: Values of phase angle (ϕ_{xy}), ellipticity and the angle of propagation with respect to the mean magnetic field, when the spectral bumps are observed consecutively in the whistler range for nearly 30 min (from 17.2 to 17.7 h) at 1 AU using the *CLUSTER* satellite in the solar wind. Taken from Lacombe et al. (2014).

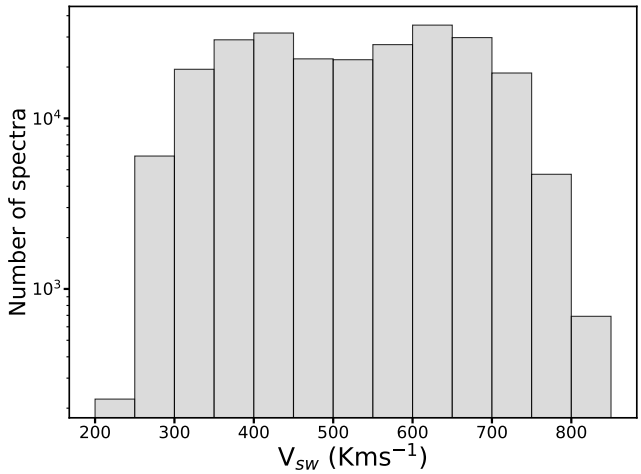

FIGURE 5.5: Distribution of the solar wind velocities of the spectra used for our analysis.

From Figure 5.5 we can understand that in our analyzed samples there are nearly equal amounts of observations made in the slow and in the fast solar wind: 44 % of the spectra are in the slow wind and 36 % in the fast wind. The remaining 20 % correspond to intermediate velocities.

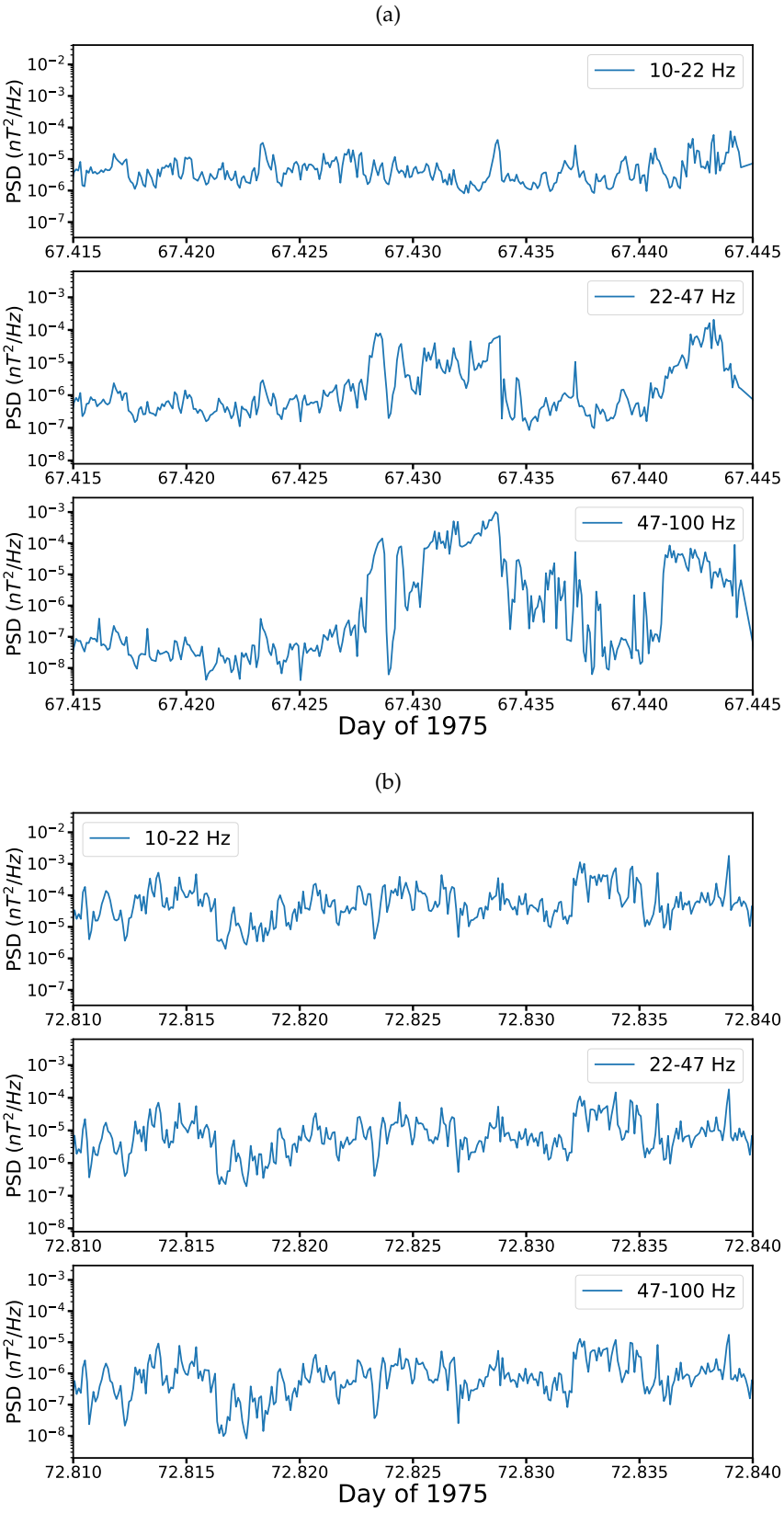

FIGURE 5.6: PSD of the magnetic field in a 45-min interval of slow wind (a) and fast wind wind (b) for 3 different bands.

In Figure 5.6 we show an example of the PSD of the B_y component in 3 frequency

bands using a 45 minute interval of the slow and fast solar wind. In the fast wind, we observe that all the spectral bands show similar behavior, with no spectral bands behaving differently from the others. This coherent evolution of the spectra means that the spectral shape is conserved and only the amplitude of the spectrum is varying. A completely different picture emerges from the slow wind, in which the channels show more individual behavior and so the spectral shape is changing. These variations are most conspicuous on Day 67.425-67.435. This general behavior of the slow and fast solar wind is shown using the ratio of different channels vs time in the 3.16.

5.3 Whistler wave identification and their confirmation

5.3.1 Identification

As said before the available spectral density values of *HELIOS* are the main source to identify the whistler waves in the inner heliosphere in our analysis.

In the Figure 5.7 we show the respective spectra of the example interval chosen in Figure 5.6. In Figure 5.7 (a), we observe spectra with large spectral bumps along with the spectra without any clear spectral bumps and some smooth spectra. In Figure 5.7 (b), we observe mostly smooth spectra without any spectral bumps.

Generally, when we analyze spectral data from the Helios SCM we regularly observe spectra as in Figure 5.7:

- Spectra with local maxima (bump), background magnetic field turbulence spectra influenced by large amplitude quasi-monochromatic waves as in 5.7 (a).
- Other is smooth spectra, decreasing monotonically with frequency, with no local maxima, a permanent feature of background magnetic field as in the Figure 5.7 (b), i.e., spectra showing only the background magnetic field turbulence, see chapter 3 for detailed analysis.
- There are some spectra which are in between, without a distinctive local maxima, those are the ones that might have been affected by very low amplitude quasi-monochromatic waves.

We consider those spectra in which one single local maximum (bump) clearly stands out with respect to the PSD of the background turbulence. We are concentrating on the distinctive, large amplitude waves compared to the background fluctuation amplitudes in the inspected regions. Mathematically speaking, $\frac{dPSD}{df}$ is negative for the usual background turbulence like spectra as we go towards higher frequencies. However, when the large amplitude whistler waves influence the spectra, as we go towards higher frequencies at a certain frequency $\frac{dPSD}{df}$ will be positive and again goes to negative. In this way, we are able to identify the presence of spectral bump. In our analysis we have excluded events that can be interpreted as interplantery shock or as magnetic clouds. In our study, we have excluded the events observed closer to the interplanetary shocks (Kruparova et al., 2013) or the magnetic clouds (Bothmer and Schwenn, 1998). In our total analyzed samples of 246543 we have observed 5276 of the spectra which have a clear distinctive spectral bump.

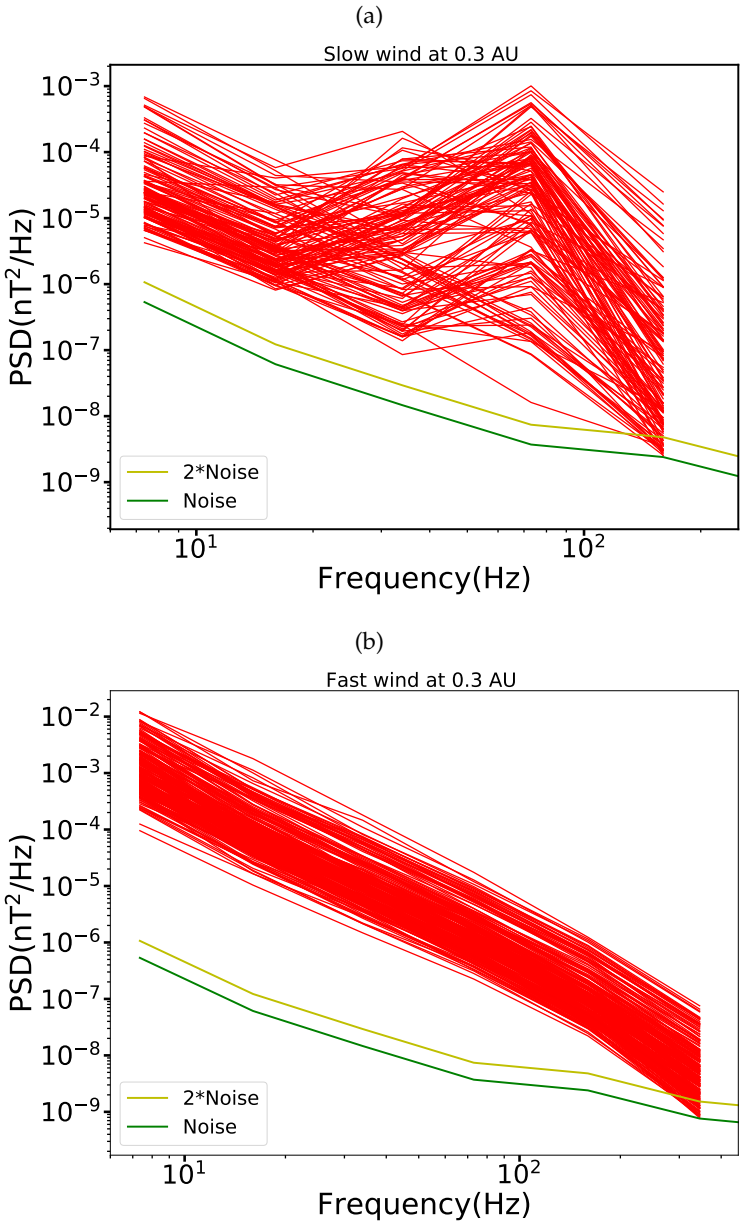

FIGURE 5.7: Spectra corresponding to the time interval shown in Figure 5.6, in (a) we show the spectra observed in slow wind and in (b) we show the spectra observed in the fast wind interval .

5.3.2 Method of conformation of the whistler waves

After the identification of spectra with spectral bumps throughout the data, we identify the peak of the bump and its corresponding central frequency. Now we analyze whether the observed frequencies are in the whistler range or not.

We show our analysis using an example spectra. In the Figure 5.8 we show the spectra with distinctive local maxima corresponding to the time interval shown in Figure 5.6. In Figure 5.8 (a) we show the spectra and in Figure 5.8 (b) we show the spectra with respect to $\frac{f}{f_{ce}}$. From this Figure we can infer that for the observed example spectra, peaks of the spectral bumps are in the whistler range, i.e. between $f_{lh} \approx \sqrt{f_{ce} f_{ci}}$ and electron cyclotron frequency f_{ce}. Now we verify this for all the spectra.

In the Figure 5.9 we show the distribution of normalized central frequencies corresponding to the bumps observed throughout our analysis, almost all of the bumps observed are between lower hybrid frequency $f_{lh} \approx \sqrt{f_{ce} f_{ci}}$ and electron cyclotron frequency f_{ce}. There were 10 spectra which were observed very close but below the whistler range, Doppler shift may be the reason behind this, but we discard them in our analysis. As mentioned before, studies by Lacombe et al. (2014) have shown that fluctuations were right handed circularly polarized and showed all the features of narrowband whistler waves whenever they have observed a spectral bump in the whistler range. This important observation from the study of Lacombe et al. (2014) guides us in understanding that the spectra with the bumps in the whistler range are likely due to the presence of narrowband whistler waves.

In our study we have 5276 spectra (8 s) of the B_y component which include whistler waves. This number is minute ($\approx$ 2%) compared to the total number of spectra analyzed. Therefore, we understand that only a smaller portion of spectra are influenced by whistler waves. These observed whistlers provide us the picture of large amplitude whistler behavior at different radial distances and in different wind types. However, we have to warn the readers that the very low amplitude whistler waves might be left out of the analysis as their amplitudes are not high enough to validate the presence of a spectral bump, in turn the presence of whistlers.

(a)

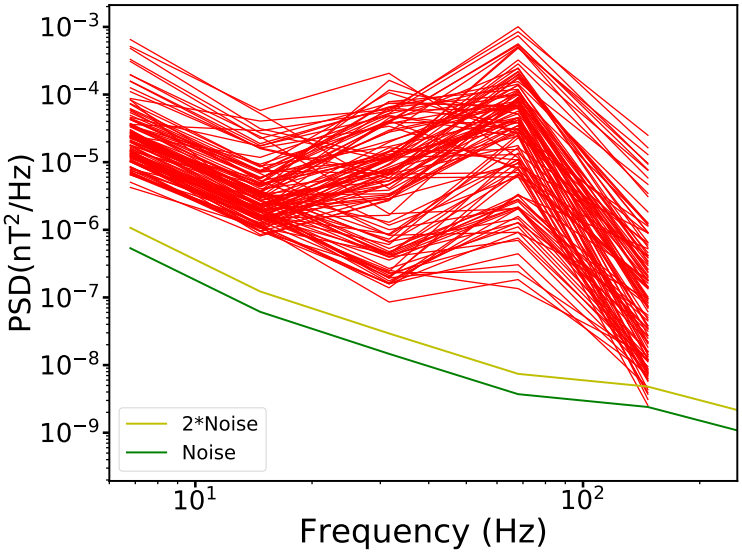

(b)

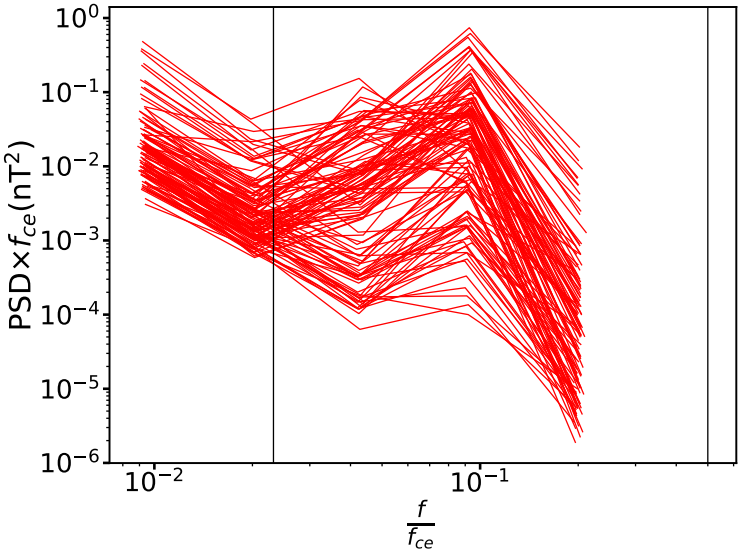

FIGURE 5.8: Example spectra with clear bumps in the Figure 5.7 are used. In (a) we show the spectra with clear bumps and in (b) we show the spectra with respect to the normalized frequency. The region between the black vertical lines correspond to whistler range.

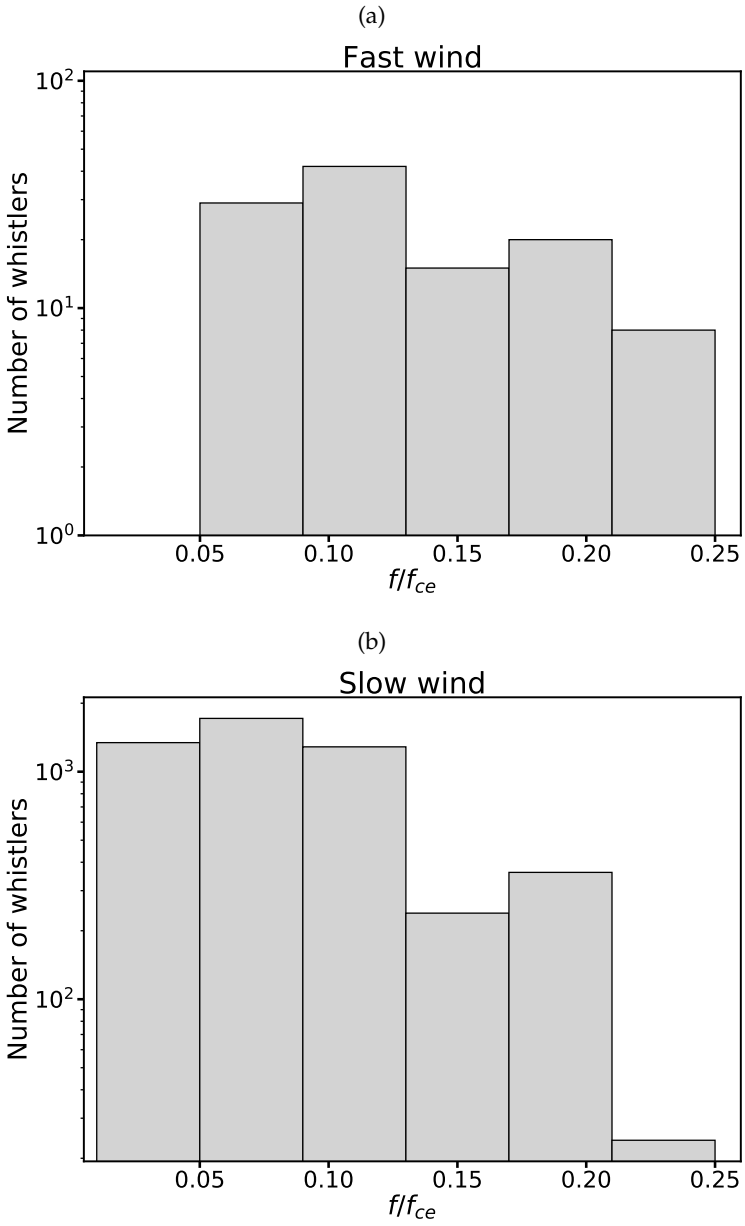

FIGURE 5.9: Range in which central frequencies corresponding to whistler waves are spread with respect to the electron cyclotron frequency in (a) fast wind and (b) slow wind.

The identification procedure we have looked into is the frequency range in which we observe spectral bumps. Usually, the frequency observed by the spacecraft is Doppler shifted, to know the real frequency of the observed waves we have to remove the Doppler effect.

In Equation 5.1, f_{sc} gives the observed frequency in the spacecraft frame, f is the real frequency of the wave and $\mathbf{k} \cdot \mathbf{v}_{sw}$ gives the Doppler effect contribution.

$$f_{sc} = f + \mathbf{k} \cdot \mathbf{v}_{sw} \tag{5.1}$$

$$f = f_{sc} - f_{sc} \frac{\mathbf{k} \cdot \mathbf{v}_{sw}}{f_{sc}} \tag{5.2}$$

Approximately

$$f = f_{sc}(1 - \frac{v_{sw}}{v_\phi}\cos\theta_{kv}) \tag{5.3}$$

From the Equation 5.3 we can see that to get the real frequency of the observed wave we have to know the θ_{kv} and the phase velocity (v_ϕ) of the wave in the spacecraft frame. We can not calculate the θ_{kv} values due to the non-availability of waveform data. However, we can approximately calculate the phase velocity assuming the observed wave is a whistler and check whether the phase velocities are high enough that Doppler effect is negligible.

Using the cold plasma theory we get the dispersion relation of the right hand circularly polarized whistler waves (Bellan, 2006),

$$n^2 = \frac{c^2k^2}{\omega^2} \approx 1 + \frac{\omega_{pe}^2/\omega^2}{(\frac{\omega_{ce}\cos\theta_{kB}}{\omega} - 1)} \tag{5.4}$$

Assuming that whistler waves are propagating quasi parallel to magnetic field, we can consider $\cos\theta_{kB} \approx 1$, for observed whistler frequencies $\omega < \omega_{ce}$, so $(\frac{\omega_{ce}\cos\theta_{kB}}{\omega} - 1) \approx \frac{\omega_{ce}}{\omega}$

$$c^2k^2 \approx \omega^2 + \omega_{pe}^2(\omega/\omega_{ce}) \tag{5.5}$$

$\omega << \omega_{pe}$,

$$c^2k^2 \approx \omega_{pe}^2(\omega/\omega_{ce}) \tag{5.6}$$

Now the phase velocity of the whistler is given by

$$v_\phi = \frac{\omega}{k} = c\frac{\sqrt{\omega\omega_{ce}}}{\omega_{pe}} \tag{5.7}$$

Figure 5.10 shows the distribution of phase velocity of all the observed whistler waves for the case of fast and slow wind separately at different radial distances. From Figure 5.10 we can observe that most of the whistler waves have high phase velocities compared to the solar wind speed. However, there is a bin (250-300 kms^{-1}) with low phase velocities, this bin is related to the whistler waves observed closer to the Sun. These whistlers solar wind velocity is found to be comparable to the phase velocities. Therefore, on overall it can be expected that the Doppler effect is not the main effect to observe the spectral bumps in the whistler frequency range. Therefore, if the spectral bumps we observe satisfy the whistler frequency range criteria, i.e. between f_{lh} and f_{ce}, then they are most probably the spectra affected by the whistler waves.

We have also looked into how the phase velocity compares to the Alfvén velocity (V_A) for the observed whistler waves. For the fast wind case, $10 \leq V_\phi/V_A \leq 20$ and for the slow wind case, $7 \leq V_\phi/V_A \leq 20$. This explains that the phase velocity of the whistler waves is very high when compared to the Alfvén velocity (V_A).

All of our analyses on phase velocities have to be considered with a bit of caution, as phase velocity calculations itself are based on the assumption that the observed waves are whistler waves.

Even with the limitations on the data availability, we tried to verify whether the observed whistlers are propagating parallel to the mean magnetic field. We have followed a simple approach: knowing that the spectra available are of B_y and B_z, using the MAG we have looked into the intervals in which the magnetic field is dominantly ($> 90\%$) observed in the B_x component. We expect a parallel propagating

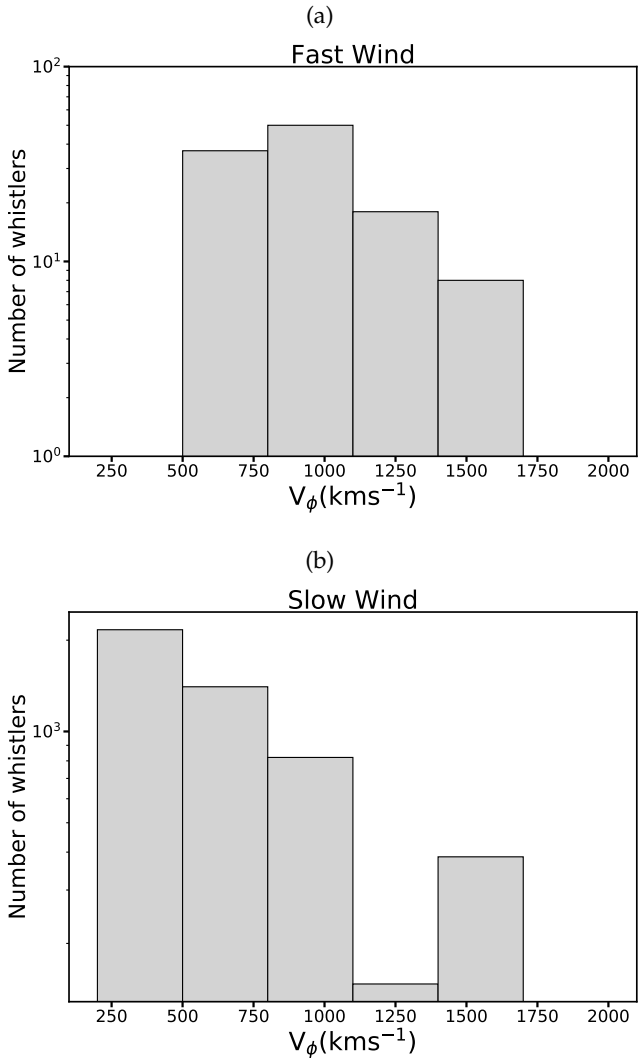

FIGURE 5.10: Phase velocity of all the observed whistler waves (a) fast wind and (b) slow wind.

circularly polarized whistler wave to show nearly the same level of whistler amplitudes in both y and z direction. However, for the cases we have analyzed we have not observed the same level of fluctuations in both y and z direction. The reason might be that whistlers of the analyzed interval might not be the parallel whistlers, but oblique. The other important reason might be the stray magnetic field affecting the B_z component, which might be causing the fluctuations to look different.

We have even tried to generalize the calculation for all the different directions of propagation, for a whistler propagating parallel to the mean magnetic field. If δB is the amplitude of whistler wave then we can have an idea on the ratio of amplitudes observed in the two of the components knowing the mean magnetic field direction. The approximate ratio of the whistler amplitudes in the B_y and B_z component is expected to be:

$$\frac{\delta B^2 \sin^2 \theta_{By}}{\delta B^2 \sin^2 \theta_{Bz}} \rightarrow \frac{\sin^2 \theta_{By}}{\sin^2 \theta_{Bz}}. \tag{5.8}$$

Where, θ_{By} & θ_{Bz} are the angles between the mean magnetic field and B_y, B_z component respectively. We know the amplitude of whistlers observed in B_y and B_z direction, we can estimate their ratios and correlate with expected ratios using the equation 5.8. From our analysis, we have observed that there is no correlation (< 0.1). Which directs us towards the conclusion that, either the whistlers are propagating obliquely or the stray field effects are responsible for no correlation. However, we cannot be conclusive about the angle of propagation with the mean magnetic field.

For our analysis we assume the whistlers to be quasi-parallel to the mean magnetic field as all the observations at 1AU provide a strong motivation for supporting that closer to the Sun too, the whistlers are quasi-parallel.

5.4 Whistler wave properties

After the identification and the confirmation of the presence of whistler waves, let us now look at some of the important properties related to the observed whistler waves.

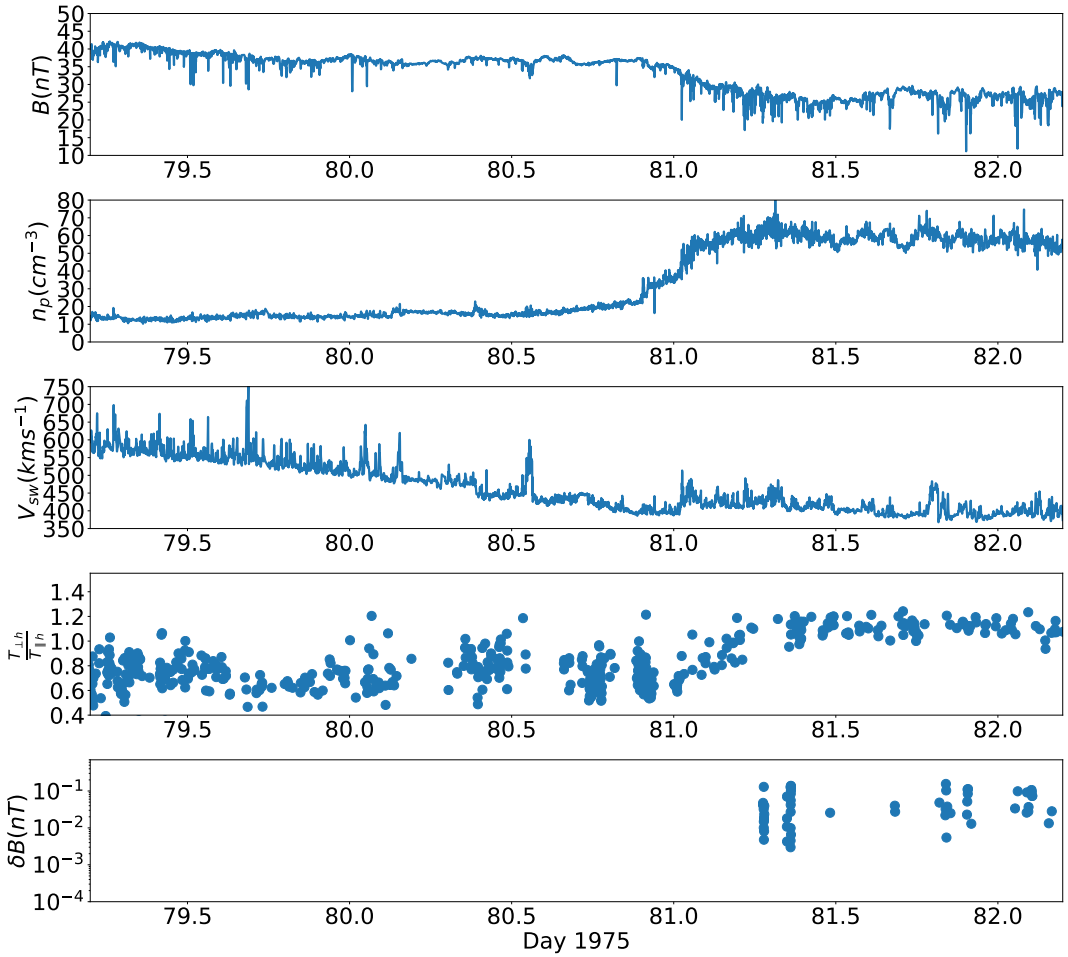

FIGURE 5.11: A three day interval around 0.4 AU, where we have a good amount of electron temperature values and whistlers. The panel (1) shows the magnitude of magnetic field, panel (2) shows the proton density, panel (3) shows the velocity, panel (4) shows the halo aniostropy ($\frac{T_{\perp h}}{T_{\parallel h}}$) values taken from Štverák et al. (2009) and in the panel (5) we show where the whistler waves are observed and the amplitudes of observed whistler waves

In the Figure 5.11 we show an example of the typical plasma parameters around 0.4 AU along with the amplitudes (detailed discussion follows in the coming subsections) of the observed whistler waves to get a perspective on the plasma conditions when the whistler waves are observed and not observed. We observe that whistler waves appear in the slow solar wind, which is a general behavior observed throughout our analysis in the inner heliosphere.

5.4.1 Velocity of the observed whistler waves

In Figure 5.12 we show the distribution of total spectra as a function of velocity in grey and the distribution of slow wind whistler waves are shown in green, mixed wind whistler waves are shown in red and the fast wind whistler waves are shown in blue. We observe that whistler waves are dominantly observed in the slow solar wind.

When we consider the percentage of whistler waves as a function of the wind velocity, we observe that there is a constant decrease of whistler waves as the wind velocity is increasing. We observe this clearly in Figure 5.13. This is the first time that the decrease in the presence of whistler waves with the increase in the wind velocity is shown.

Even though we have observed nearly equal amount of spectra in slow and fast wind with respect to the total analyzed spectra which satisfy the 2x noise cutoff, nearly 94% of the identified whistler waves were observed in slow solar wind, i.e. whistler waves are dominantly observed in the wind with velocity less than 500 kms^{-1}. This is similar to the studies by Lacombe et al. (2014) at 1 AU, where they suggest that the slow wind is a necessary condition for the observation of intense whistler waves. This is quite interesting to see that conditions suggested at 1 AU are also satisfied in the inner heliosphere.

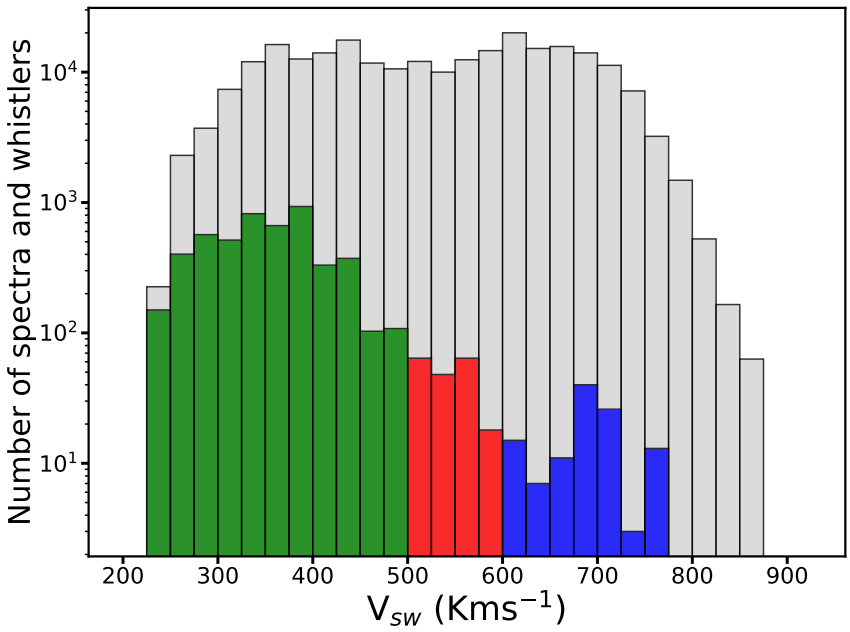

FIGURE 5.12: In grey: histogram of the number of observed spectra with respect to the solar wind velocity. The green color shows the number of whistler spectra in slow solar wind, the red color shows the number of whistler spectra in the mixed solar wind and the blue shows the number of whistler spectra in the fast solar wind.

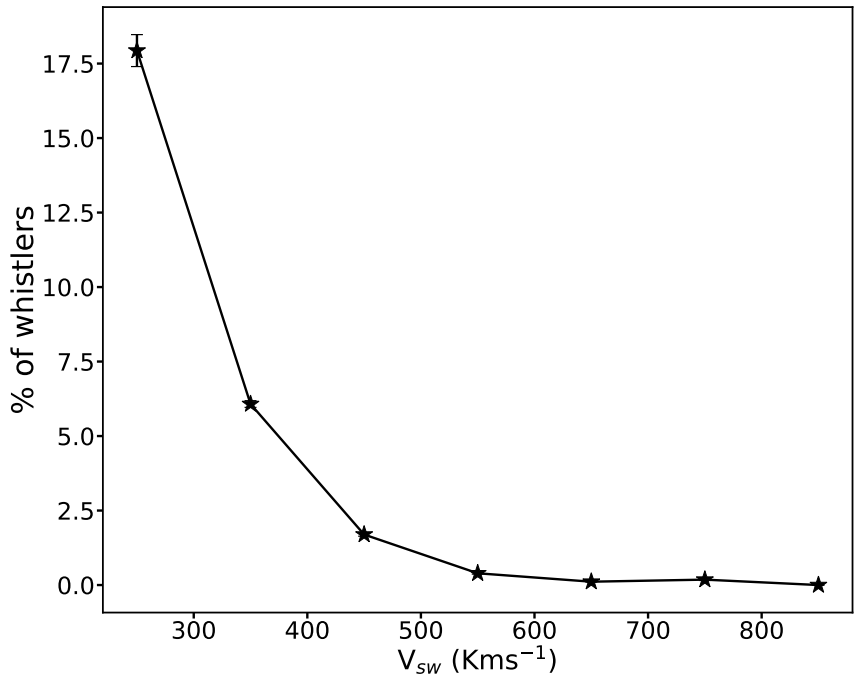

FIGURE 5.13: Percentage of the spectra showing the presence of whistler waves as a function of the solar wind velocity.

In our study, we also observe whistler waves in the fast solar wind but they are observed very sparsely, a minute 2% of the total observed whistler waves. The fast wind whistler waves were mostly observed at 0.9 AU, that too in a pure high speed stream.

5.4.2 Radial distribution of the observed whistler waves

We have analyzed how the whistler waves are distributed radially in the inner heliosphere between 0.31 to 0.91 AU. We have analyzed the number of whistler waves in the slow and fast wind with respect to the number of spectra which satisfy our noise condition of 2 times the noise level at least till the 4th band for slow and fast wind respectively. In Figure 5.14 we show how the percentage of slow and fast wind whistler waves is changing as a function of radial distance.

Interestingly what we observe from Figure 5.14 is that how low the presence of whistler waves is in the fast wind when compared to the slow wind. The fast wind whistler waves start to appear far away from the Sun and the percentage of this fast wind whistler waves increases as we move away from the Sun. We observe a slight increase in the percentage of whistler waves in the slow wind as well.

The increase in the presence of whistler waves with the radial distance shown in the Figure 5.14 is one of the main results of our whistler analysis.

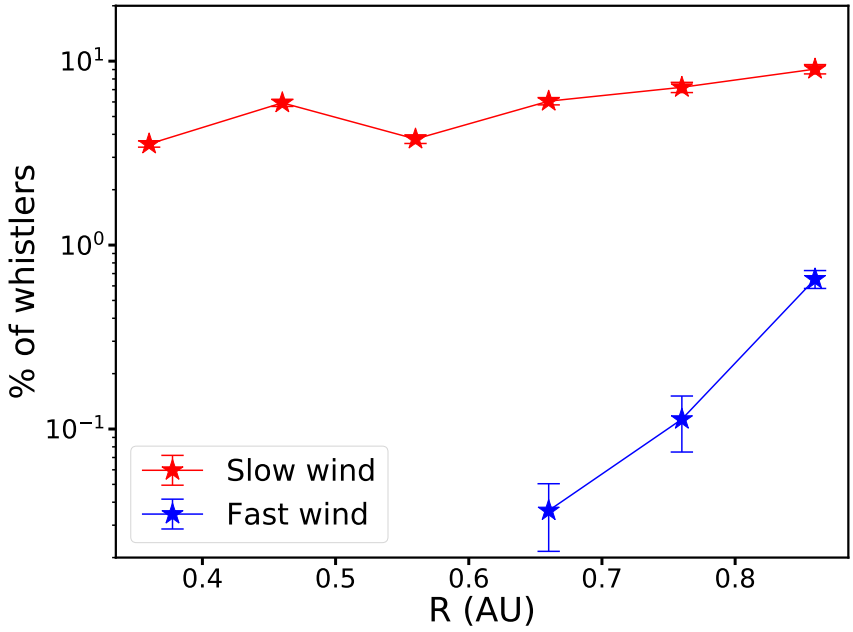

FIGURE 5.14: Radial variation of percentage of whistler waves in the slow and fast wind. Error bars show standard error.

5.4.3 Thermal pressure of the observed whistler waves

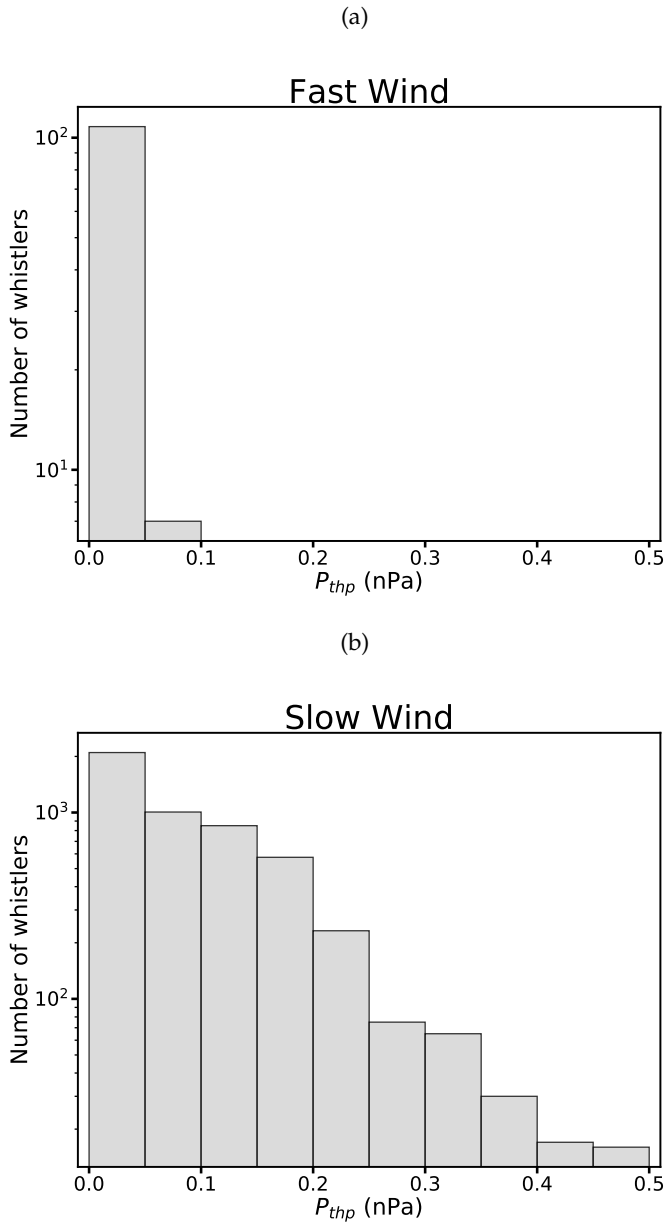

FIGURE 5.15: Proton thermal pressure of whistler waves (a) fast wind and (b) slow wind.

The thermal pressure ($P_{thp} = n_p k_B T_p$) which is correlated with the magnetic fluctuation level (Smith, Vasquez, and Hamilton, 2006; Alexandrova et al., 2013; Lacombe et al., 2014) is one of the other important parameters thought to have a clear limitation for the whistler waves to be observed (Lacombe et al., 2014). It is understood that the higher the turbulence level (magnetic fluctuations), the higher the thermal pressure. So, higher thermal pressure is expected to mask the observed whistlers. Studies by Lacombe et al. (2014) at 1 AU have suggested that all of their observed whistler waves have thermal pressure values below 0.04 nPa and they did not observe whistlers above this value.

In Figure 5.15 we show the thermal pressure of our observed whistler waves in the slow and fast solar wind. We observe that the thermal pressure of observed

whistler waves covers a wide range of values (0.01,0.5), not constrained to $<$ 0.04 nPa suggested by Lacombe et al. (2014). This is as expected as the thermal pressure values increase as we move closer to the Sun and there cannot be one distinctive limit of thermal pressure value for all the distances.

In Figure 5.16 we can see a difference in the thermal pressure values of whistler waves from closer to the Sun (0.3-0.4 AU) to away from the Sun (0.8-0.9 AU).

We have verified whether the upper limit of 0.04 nPa suggested in the studies of Lacombe et al. (2014) for slow wind at 1AU is satisfied when we are away from the Sun, i.e. at-least above 0.8 AU. As expected we observe that cutoff (0.04 nPa) is satisfied for all the observed slow wind whistler waves, this can be seen from Figure 5.17 (b). Therefore, we can reaffirm that for the slow wind whistler waves away from the Sun ($>$ 0.8 AU), the thermal pressure condition of $<$ 0.04 nPa is an appropriate condition as suggested in the studies of Lacombe et al. (2014). Whereas for the fast wind whistler waves above 0.8 AU, we observe in the Figure 5.17 (a) that the thermal pressure condition of $<$ 0.04 nPa is not satisfied, fast wind whistler waves showed higher thermal pressure. We have looked into magnetic pressure and plasma beta (protons), but could not establish any clear correlation.

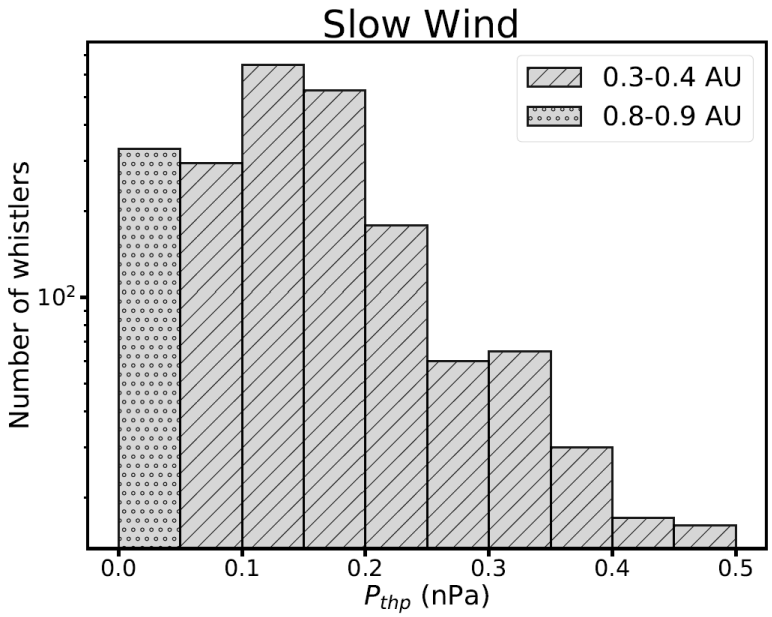

FIGURE 5.16: Thermal pressure of whistler waves in slow wind closer (0.3-0.4 AU) and farther (0.8-0.9 AU) from the Sun

(a)

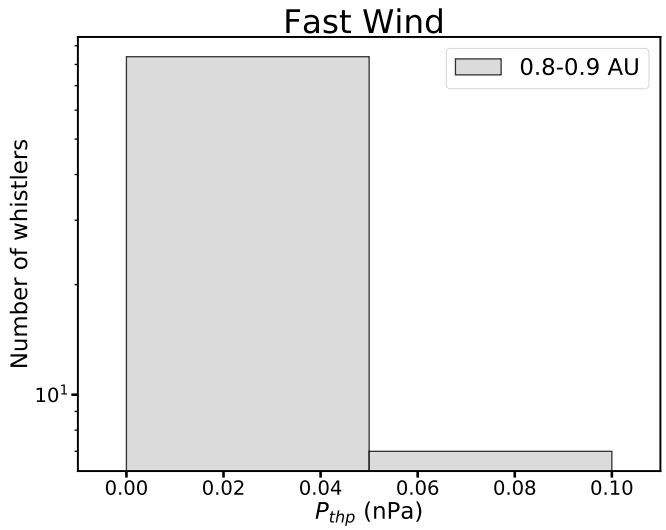

(b)

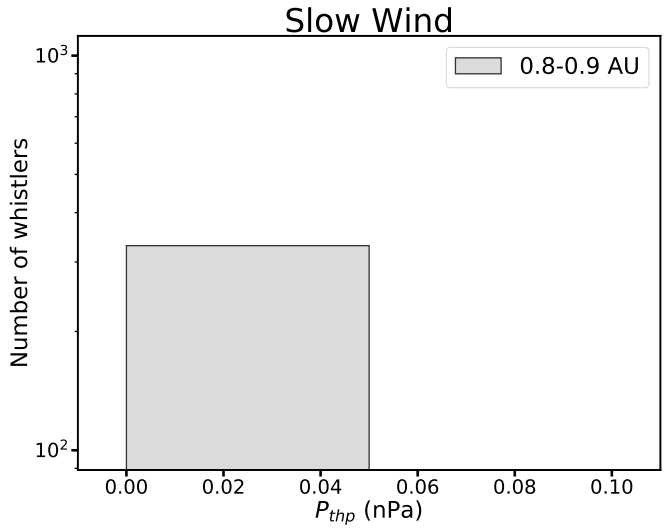

FIGURE 5.17: Proton thermal pressure of whistler waves observed between 0.8 to 0.9 AU (a) fast wind and (b) slow wind.

5.4.4 Halo electron anisotropy ($\frac{T_{\perp h}}{T_{\parallel h}}$) values corresponding to the observed whistler waves

Studies such as Gary, Skoug, and Daughton (1999), Wilson et al. (2013), and Tong et al. (2019b) have shown the significance of electron $\frac{T_{\perp h}}{T_{\parallel h}}$ ratio when the whistler waves are observed. The reason for its significance will be discussed in detail in the coming sections. However, in the case of *HELIOS* the electron data are not regularly available as the proton data, there are large gaps, therefore there are not many $\frac{T_{\perp h}}{T_{\parallel h}}$ values corresponding to the observed whistler waves. Our technique to identify the accurate $\frac{T_{\perp h}}{T_{\parallel h}}$ values corresponding to whistler waves identified is such that we find the time intervals in which we observe the 8 s whistler spectra consecutively

for at least 80 s, i.e. 10 consecutive spectra and then identify the electron temperature values which are measured in those whistler intervals, by this method we are sure that electron temperatures measured are always during the presence of whistler waves. We found 11 such intervals and all the observed whistler waves have values $\frac{T_{\perp h}}{T_{\parallel h}} > 1.0$ as in agreement with the studies of Gary, Skoug, and Daughton (1999) and Wilson et al. (2013).

We could have more intervals if we look for the closest time to the observed whistler at which $\frac{T_{\perp h}}{T_{\parallel h}}$ value is available, keeping the constraint of 10 min we found that 86% of the $\frac{T_{\perp h}}{T_{\parallel h}}$ values corresponding to whistlers satisfied $\frac{T_{\perp h}}{T_{\parallel h}} > 1.0$. In Figure 5.18 we show the $\frac{T_{\perp h}}{T_{\parallel h}}$ as a function $\beta_{e\parallel h}$, where red dots correspond to whistlers and green dots to all the cases (including whistlers). We observe that whistlers are predominantly observed when $\frac{T_{\perp h}}{T_{\parallel h}} > 1.0$ and high $\beta_{e\parallel h}$.

Even though we do not have exact values of $\frac{T_{\perp h}}{T_{\parallel h}}$ for all the observed whistler waves, we can have a general idea of the conditions around when the whistler waves appear, i.e. usually in the slow wind. $\frac{T_{\perp h}}{T_{\parallel h}}$ values are relatively higher in the slow solar wind when compared to the adjacent fast solar wind, a glimpse of this transformation can be seen from the example Figure 5.11. To summarize, whistlers are mostly observed when the $\frac{T_{\perp h}}{T_{\parallel h}}$ vales are higher.

5.4.5 Amplitude of the fluctuation of the observed whistler waves

For the observed whistler waves we have calculated the amplitude and normalized amplitude of fluctuation, however, it is only the contribution from the B_y component. After the confirmation that the peak or a bump is observed in the whistler range, the peak value (PSD_y) of the bump is multiplied with its respective frequency bandwidth (Δf), which gives us the mean square amplitude of the fluctuation. The square root of mean square amplitude can be interpreted as the amplitude of the fluctuation, as in the Equation 5.9.

$$\delta B_y = \sqrt{PSD_y * \Delta f} \tag{5.9}$$

We have not removed the background turbulence contribution as the amplitudes of the whistler waves are so large that the contribution of background turbulence represents a minor fraction only of the total amplitude ($< 10\%$). This is the first time that amplitudes of the whistler waves in the inner heliosphere are shown.

In Figure 5.19 we present the radial variation of the mean whistler amplitudes separately for the case of the slow and fast solar wind. We infer that whistler waves observed in the fast wind are of higher amplitudes when compared to the slow wind at the same distance from the Sun. The amplitude of whistler fluctuations decreases in the case of fast wind as we move farther from the Sun. In the slow wind case too we observe a similar behavior, but first, we observe a decrease in amplitudes till 0.7 AU and then a small increase till 0.9 AU. We normalize the amplitudes with respect to the mean magnetic field, as the magnetic field fluctuations are directly related to the mean magnetic field. In the Figure 5.20 we show the radial variation of the normalized whistler amplitudes separately for the case of the slow and fast solar wind. We have normalized the whistler amplitude values with the closest mean magnetic field values. Interestingly we observe that even when the normalized amplitudes are calculated, whistler waves have larger relative amplitudes in the fast wind than

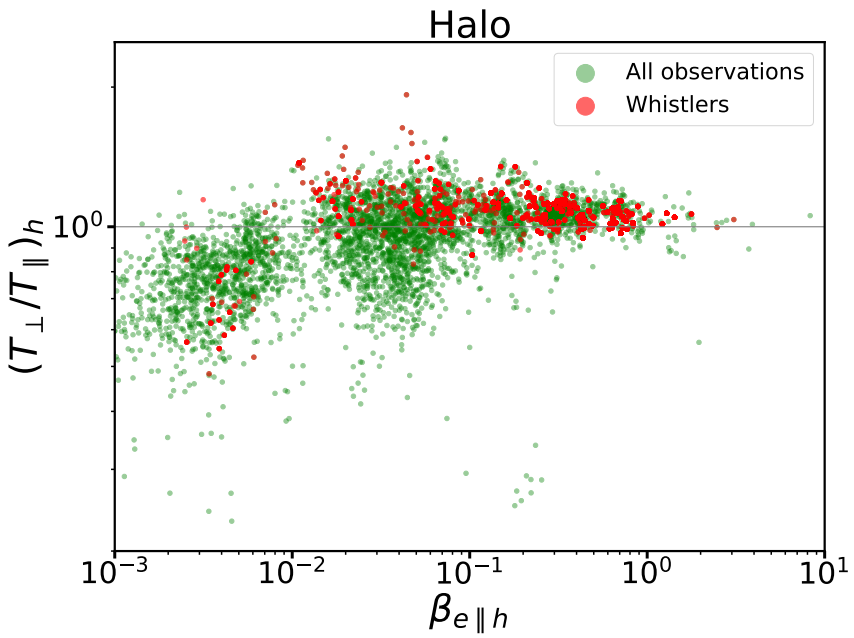

FIGURE 5.18: Halo anisotropy ($\frac{T_{\perp h}}{T_{\parallel h}}$) as function of β_e for the observed whistlers and the whole data during the time of Whistler analysis.

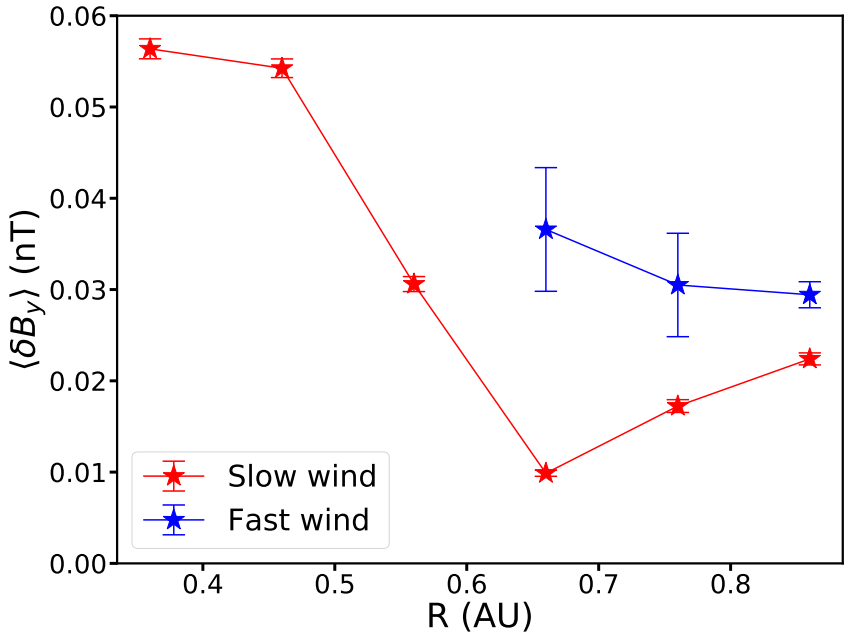

FIGURE 5.19: Amplitude of whistler waves in the slow and fast solar wind, error bars show the standard error ($\frac{\sigma}{\sqrt{n}}$)

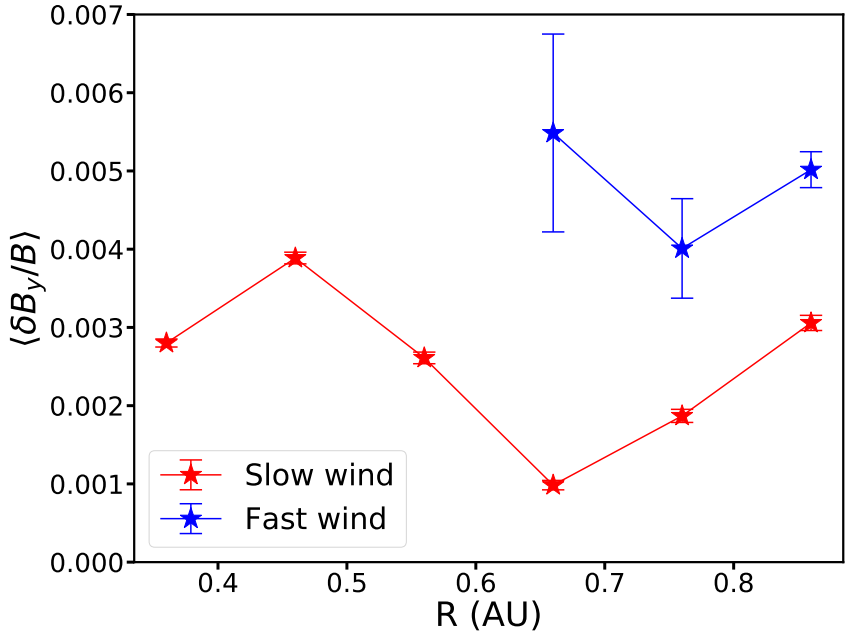

FIGURE 5.20: Normalized amplitude of whistler waves in the slow and fast solar wind, error bars show the standard error ($\frac{\sigma}{\sqrt{n}}$)

in the slow wind. There is no clear trend in the radial evolution of the relative amplitudes in the slow or the fast solar wind.

Summary of the important whistler properties

Many interesting properties of whistler waves are observed, we mention the important ones:

- Whistler waves are very dominantly observed in the slow solar wind in the inner heliosphere (0.3 to 1 AU).
- In the fast wind we observe a very minute percentage of whistler waves and that too farther from the Sun.
- The presence of whistler waves decreases as the wind velocity increases.
- Frequency of whistler waves decreases as we go closer to the Sun.
- For the whistler waves where the electron temperatures are available we have observed that $\frac{T_{\perp h}}{T_{\parallel h}} > 1$.
- The normalized amplitude of the whistler waves using the spectral density values from the single component (B_y) is below 0.01 for the majority of the observed whistler waves throughout the inner heliosphere for both fast and slow solar wind. This explains that waves are linear.
- For a given regime of solar wind, the probability of observing whistler waves increases in the inner heliosphere as we move away from the Sun. Especially the appearance of fast wind whistler waves farther from the Sun (>0.5 AU) and increase in their presence after that.

Some of the important implications of the observed whistler properties are:

Our whistler wave observations can explain the variations in the heat flux dissipation in the slow and fast wind in the inner heliosphere. We observe the majority of the whistler waves in the slow wind at all the radial distances and the gradient of heat flux variation with the radial distance is steeper in the slow wind compared to the fast wind (Stverák, Trávníček, and Hellinger, 2015). Therefore, the reason for heat flux dissipation to be efficient in the slow wind compared to the fast wind might be related to the presence of whistler waves as suggested by (Stverák, Trávníček, and Hellinger, 2015).

Whistlers are expected to scatter the Strahl electrons (Vocks and Mann, 2003; Vocks, 2012; Kajdič et al., 2016) and we know that Strahl part is highly scattered in the slow wind compared to the fast wind and Strahl is becoming broader with the radial distance (Hammond et al., 1996; Graham et al., 2017; Berčič et al., 2019). Therefore, we can understand that our observations of the higher frequency of whistlers in the slow wind could explain the higher scatter of Strahl electrons in the slow wind and their radial variations.

Our whistler wave observations could also possibly explain the presence of higher $\frac{T_{\perp h}}{T_{\parallel h}}$ value in the slow wind compared to the fast wind through the cyclotron resonance heating mechanism (Vocks et al., 2005; Vocks, 2012).

In the following section, we discuss on the possible reasons for the observed whistler properties.

5.5 Discussions on the observed whistler properties in the inner heliosphere

Here we investigate in more detail the reasons for the observed behaviors.

5.5.1 Why are whistler waves predominantly observed in the slow solar wind but not in the fast wind ?

A question raises on why do we observe whistler waves dominantly in the slow solar wind and even if we observe why only in minute quantities in the fast wind. Some of the assumptions can be that whistler waves might be present in fast wind but there might be a problem of visibility due to the large Doppler shift of the regular solar wind turbulence spectra and other is that turbulence level is higher in fast wind compared to the slow wind at the same position and this will hide the generally present whistler waves.

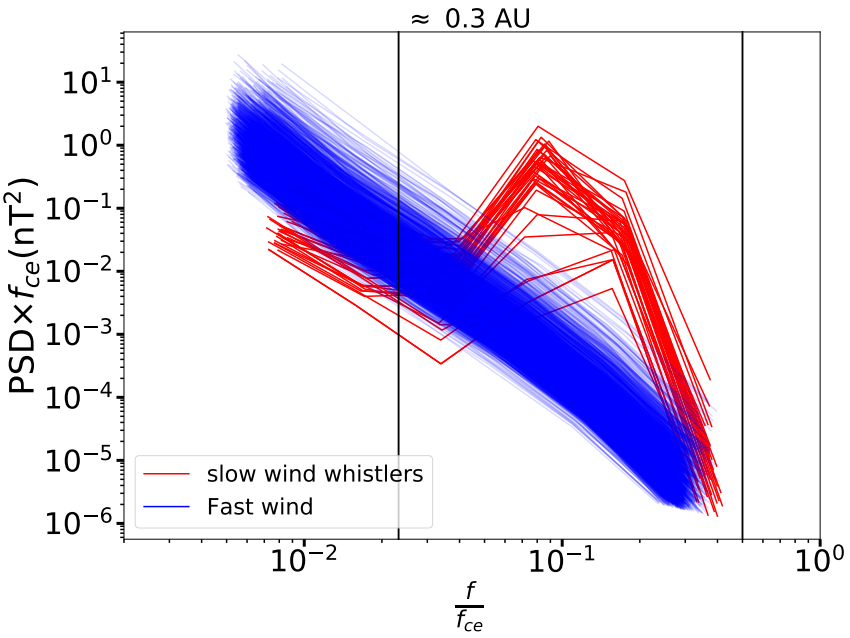

FIGURE 5.21: The spectra observed in the fast wind for 1 day (Day 73-74) and the whistler spectra observed in slow wind for 1 day (Day 68.5-69.5). The vertical lines correspond to f_{lh} and $0.5f_{ce}$.

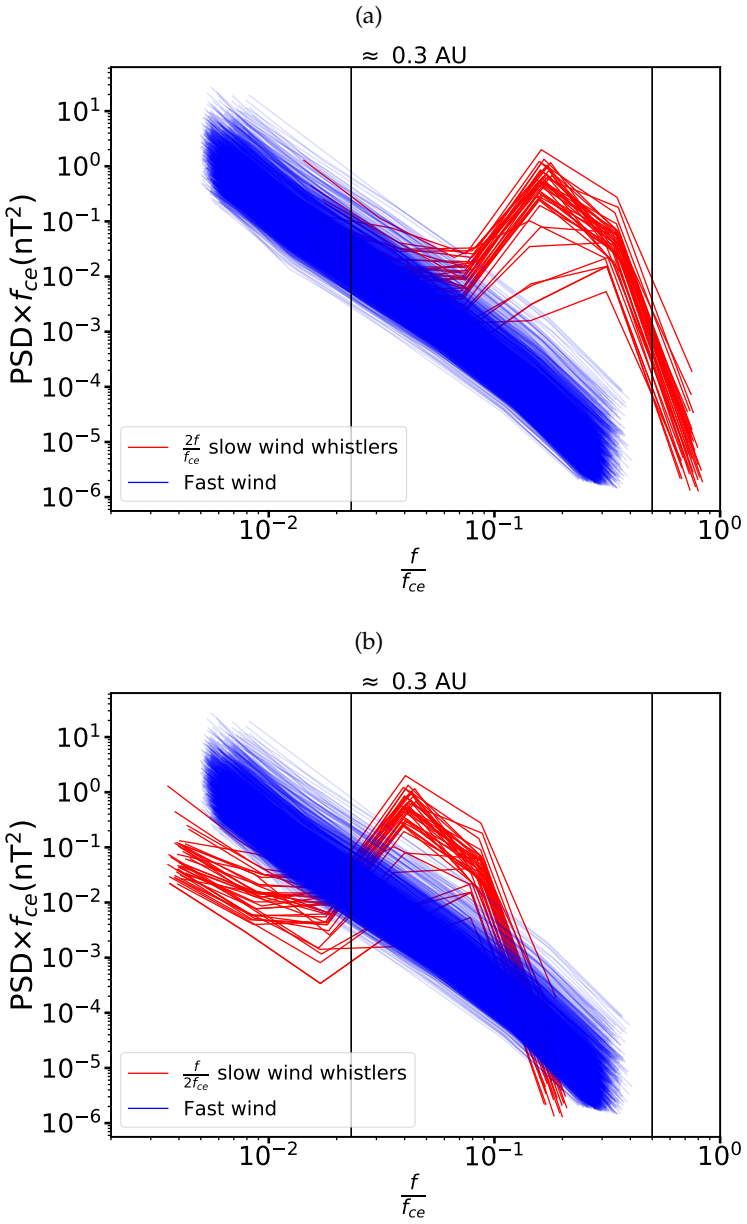

FIGURE 5.22: Slow wind whistler waves extrapolated considering the Doppler effect in two extreme cases (a) High frequency case (b) Low frequency case, the vertical lines correspond to f_{lh} and $0.5f_{ce}$.

We have looked into this issue on whether the visibility factors like high turbulence level and Doppler shift are the real issues to not observe or to observe very sparsely the whistler waves in the fast solar wind. For this, we have considered PSDs of at least 3 times the signal to noise ratio from one day of slow wind and one day of fast wind at $\approx$ 0.3 AU s. We have separated the observed whistler waves in the slow wind and all the observed spectra in the fast wind. We show them together in the Figure 5.21, here we plot PSD as a function of f/f_{ce}, so that plasma parameter differences in the slow and fast wind are taken care.

From this Figure 5.21 we get the first glimpse that, if whistler waves of large amplitude as in slow wind are present in fast wind, they would be clearly visible as the turbulence level in the fast wind is not so high enough to hide the large amplitude whistler waves.

However, there can be another important issue of Doppler effect, as the fast wind is near twice the velocity of slow wind we have considered both the possible extreme cases. Doppler shift towards high frequency (2f) Figure 5.22 (a) and Doppler shift towards low frequency (f/2) in the Figure 5.22 (b). From this Figure 5.22 we can understand that if the large amplitude whistler waves as in slow wind are present, the Doppler effect and turbulence level can be a reason but not the main issue to observe whistler waves. The high level of turbulence cannot hide these whistler waves.

There can be other reason, the possible reason might be that:

- The conditions are not favorable enough for the generation of whistler waves in the fast wind when compared to the slow wind. Even when generated, the whistlers might be of very low amplitude, especially closer to the Sun due to the generation conditions in the fast wind.

The above argument points us to see how the conditions related to the whistler generation are changing.

Is it related to generation mechanism ?

From our discussion before we have understood that lack of visibility due to the high level of turbulence or higher Doppler shift due to the high velocity in the fast wind might not be the main reason. We have to look into the conditions favoring the whistler wave generation, i.e. favoring the whistler heat flux (WHF) and whistler temperature anisotropy (WTA) instabilities, which are the major causes of whistler wave generation (Gary et al., 1994).

The lack of simultaneous electron temperature measurements for almost all of the cases when we observe whistler waves, lack of heat flux values and also the low resolution of the available measurements from the *HELIOS* mission halts us from making a direct check for the instabilities as a source of whistler wave generation. However, lack of data and the simultaneous measurements does not hinder us from understanding the general conditions related to the whistler wave generation in the slow and fast solar wind and also the variation of this conditions as we move away from the Sun to explain the observed behaviors in Figure 5.14.

Several studies carried out at 1 AU (Lacombe et al., 2014; Tong et al., 2019b) have shown that the conditions for the whistler heat flux instability to occur are met when whistler waves are observed. From the studies of Gary and Feldman (1977), Gary, Skoug, and Daughton (1999), and Wilson et al. (2013) we can understand that $\frac{T_{\perp h}}{T_{\parallel h}}$ plays a key role in improving the heat flux instability condition.

To understand why the $\frac{T_{\perp h}}{T_{\parallel h}}$ value so important in determining the instability conditions, we have to look into the dispersion relation which shows the growth rate of the instability.

Using a bi-Maxwellian distribution for core and halo, Gary and Feldman (1977) have calculated the dispersion relation for the whistler waves, and the growth rate, which is given as

$$\frac{\gamma}{\Omega_i} \propto \{(\mathbf{k}\cdot\mathbf{v}_{0H} - \omega_R)\frac{T_{\perp H}}{T_{\parallel H}} + \mid \Omega_e \mid (\frac{T_{\perp H}}{T_{\parallel H}} - 1)\}. \tag{5.10}$$

Where, Ω_e is the electron cyclotron frequency, Ω_i is the ion cyclotron frequency, $\mathbf{v}_{0H}$ is the halo electrons drift velocity, ω_R is the real frequency.

In the Equation 5.10, the first term on the right hand side is the contribution of heat flux due to the drift of the electrons and the second term is the contribution of the anisotropy to the growth of the instability.

Studies by Gary and Feldman (1977) suggest that for the solar wind parameters, normally $\mid \mathbf{k} \cdot \mathbf{v}_{0H} - \omega_R \mid << \mid \Omega_e \mid$ and explains that a slight increase in $\frac{T_{\perp H}}{T_{\parallel H}}$ value contributes positively in the growth of an instability.

If the ratio $\frac{T_{\perp H}}{T_{\parallel H}}$ decreases it might even suppress the instability due to the heat flux. When the $\frac{T_{\perp H}}{T_{\parallel H}}$ value increases it can help positively in driving the heat flux instability. If the value of $\frac{T_{\perp H}}{T_{\parallel H}}$ is high enough it can directly drive the whistler temperature anisotropy instability (WTA).

Recently Tong et al. (2019b) using the *ARTEMIS* data have shown the importance of $\frac{T_{\perp h}}{T_{\parallel h}}$ value in separating the stable velocity distribution functions from the unstable. They have performed a linear stability analysis which showed the plasma to be stable when there are no whistler waves, and unstable when the whistler waves are present.

From Figure 5.23, which is taken from the work of Tong et al. (2019b) we can observe that there is no clear separation between the stable and unstable points in the normalized heat flux vs beta core parallel ($\beta_{c\parallel}$) plot. Therefore, the heat flux values is not a clear indicator. However, we can see a clear separation in the Figure 5.23 for the stable and unstable points in the $\frac{T_{\perp h}}{T_{\parallel h}} - 1$ vs $\beta_{c\parallel}$ plot. Data with high $\frac{T_{\perp h}}{T_{\parallel h}}$ values are unstable. This stresses the importance of the halo anisotropy to the development of the instability.

In our analysis, as mentioned before, for the cases where the simultaneous whistler waves and electron temperatures values are available the value of $\frac{T_{\perp h}}{T_{\parallel h}}$ was always found to be greater than 1. This is again reiterating the importance of $\frac{T_{\perp h}}{T_{\parallel h}}$ value in the whistler generation.

However, we also have to mention that we have not always observed whistler waves when the value of $\frac{T_{\perp h}}{T_{\parallel h}} > 1$. This can be due to many reasons, one of them may be that the halo anisotropy alone cannot act as a source for the generation of large amplitude whistler waves. Similarly, we can understand that only heat flux alone is not able to produce whistler waves (Tong et al., 2019b; Tong et al., 2019a), as even if there are a large number of points above the whistler heat flux instability threshold value, it does not guarantee the generation of a whistler. Finally, we can understand that the heat flux by itself is not able to generate whistler waves. There has to be good interplay between heat flux and anisotropies.

Even though $\frac{T_{\perp h}}{T_{\parallel h}} > 1$ does not mean directly the presence of whistler waves, when the whistler waves are present then one has $\frac{T_{\perp h}}{T_{\parallel h}} > 1$. Therefore, from the statistical point of view higher the value of $\langle \frac{T_{\perp h}}{T_{\parallel h}} \rangle$ in an interval and higher number of points with $\frac{T_{\perp h}}{T_{\parallel h}} > 1$ in an interval, higher will be the probability of observing the whistler waves. We tried to look into this using the available electron temperature values throughout the *HELIOS* mission.

We show the variation of $\langle \frac{T_{\perp h}}{T_{\parallel h}} \rangle$ and $\%\frac{T_{\perp h}}{T_{\parallel h}} > 1$ through out the inner heliosphere in the Figure 5.24 and 5.25 respectively. Where, $\langle \frac{T_{\perp h}}{T_{\parallel h}} \rangle$ is the average of $\frac{T_{\perp h}}{T_{\parallel h}}$ and $\%\frac{T_{\perp h}}{T_{\parallel h}} > 1$ is the percentage of $\frac{T_{\perp h}}{T_{\parallel h}}$ values greater than 1 in the respective distance bins. We observe two important points:

- The value of $\langle \frac{T_{\perp h}}{T_{\parallel h}} \rangle$ and the $\% \frac{T_{\perp h}}{T_{\parallel h}} > 1$ is higher in the slow solar wind throughout the inner heliosphere compared to the fast solar wind.
- As we move away from the Sun the value of $\langle \frac{T_{\perp h}}{T_{\parallel h}} \rangle$ and the $\% \frac{T_{\perp h}}{T_{\parallel h}} > 1$ increases both in the slow and fast solar wind.

These observations from the Figure 5.24 and 5.25 gives us a valuable insight. First, the conditions for the whistler generation are better met in the slow wind compared to the fast solar wind. Second, the conditions for whistler generation are improving as we move farther from the Sun. This answers the two important questions raised before. Why do we observe whistler waves dominantly in the slow solar wind? The reason is that conditions for the whistler generation are better met in the case of slow wind. Why does the percentage of whistler waves increase as we move farther from the Sun both in the slow and fast wind? The reason is that the conditions for whistler generation are improving as we move farther from the Sun.

We add an additional Figure 5.26, which shows the $\% \frac{T_{\perp h}}{T_{\parallel h}} > 1$ for different velocity ranges, further confirming the reason for the decrease in percentage of whistler waves with the wind velocity we observed in Figure 5.13. This Figure 5.26 also shows how the whistler generation conditions are improving with distance for different wind velocities.

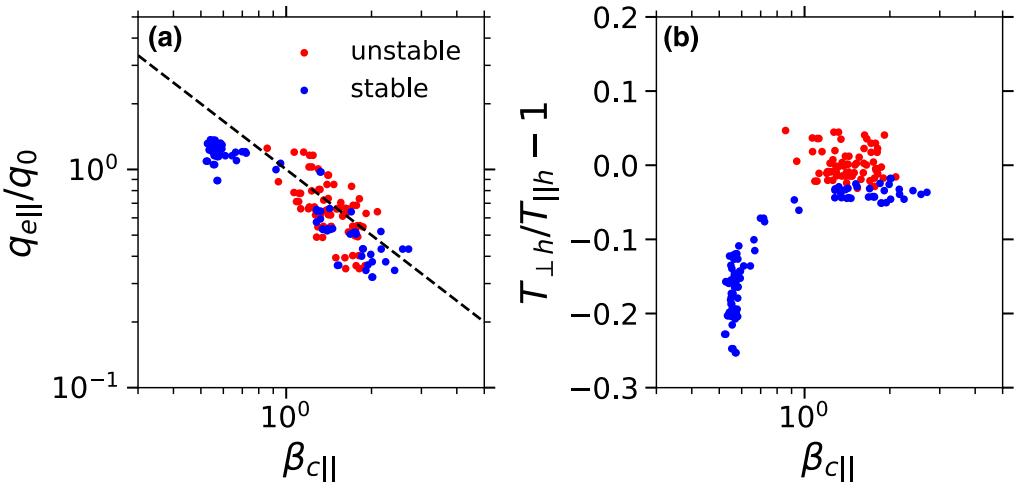

FIGURE 5.23: Normalized heat flux values for the unstable and stable points around the heat flux instability threshold and the values of $\frac{T_{\perp h}}{T_{\parallel h}} - 1$ for the stable and unstable points as function of $\beta_{c\parallel}$, in solar wind at 1AU taken from the studies of Tong et al. (2019b)

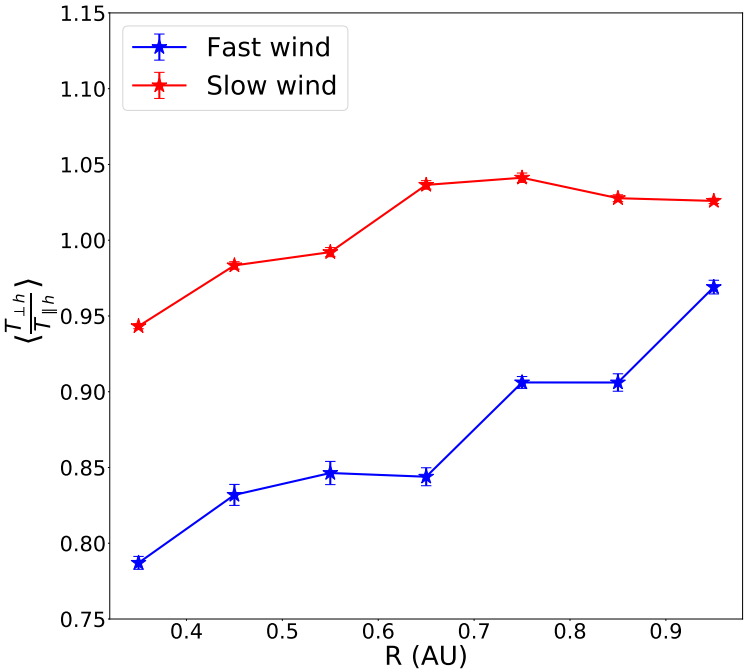

FIGURE 5.24: Mean $\frac{T_{\perp h}}{T_{\parallel h}}$ ratio as a function of distance from the Sun, the error bars here show the standard error ($\frac{\sigma}{\sqrt{n}}$)

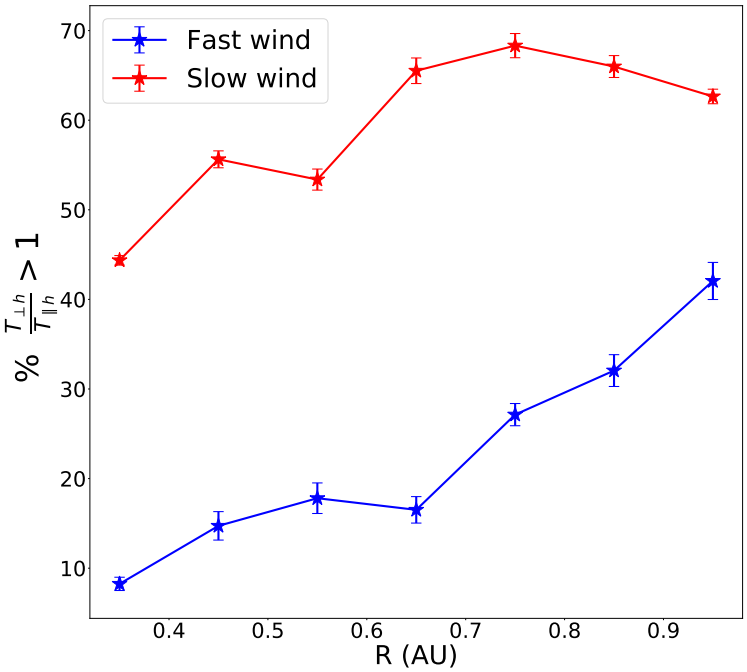

FIGURE 5.25: % of $\frac{T_{\perp h}}{T_{\parallel h}} > 1$ as a function of distance from the Sun, the error bars represents $\frac{\sqrt{n}}{n}$ value.

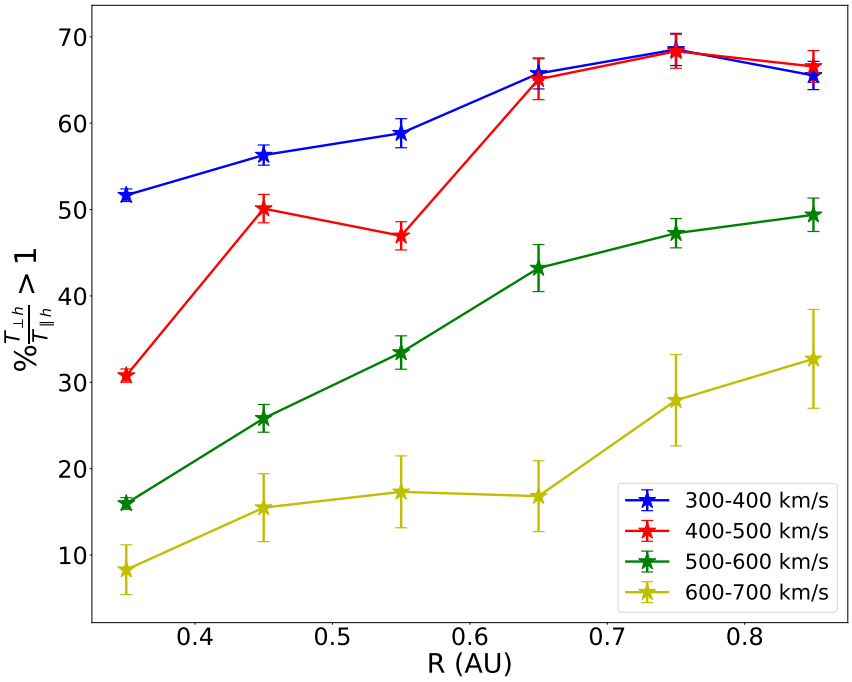

FIGURE 5.26: % of $\frac{T_{\perp h}}{T_{\parallel h}} > 1$ as a function of radial distance for different velocity ranges.

Reasons for the observed halo anisotropy trends

Now after connecting the dots for the observed whistler behaviors and answering them, there are some other questions raised during the discussion.

What can be the reason for the high $\frac{T_{\perp h}}{T_{\parallel h}}$ values in the slow wind compared to the fast wind and also importantly what can be the reason for the increase in halo anisotropy value as we move farther from the Sun? We should be looking into the mechanisms which are able to modify the electron distribution of halo electrons. There might be many possible mechanisms which could answer the observed behavior, we will suggest a possible one.

We conjecture that the increase we observe in the $\frac{T_{\perp h}}{T_{\parallel h}}$ value and also the presence of whistler waves are closely related to the broadening (scattering) of the Strahl part. The basis for this idea is related to the observed properties of Strahl part of the electron distribution in the slow and fast wind, and how this Strahl part is evolving as we move away from the Sun.

The important observations related to the Strahl electron distributions in the inner heliosphere and their evolution away from the Sun are:

- In the slow wind, the Strahl part is significantly broader than in the fast wind in the inner heliosphere. Closer to the Sun, eg at 0.3 AU in the slow wind (high β_{ec}) Strahl is scattered (broader), while in fast wind (low β_{ec}) case Strahl part is not scattered (narrow) (Berčič et al., 2019).

- Studies by Maksimovic et al. (2005) and Štverák et al. (2009) have shown that relative density of halo and Strahl are varying oppositely in the inner heliosphere, while halo relative density is increasing the Strahl relative density is decreasing. They suggest that Strahl electrons are scattered and becoming halo ones.

- The study by Berčič et al. (2019) shows that as we move away from the Sun (0.3 to 1 AU) the width of the Strahl part is increasing both in the fast and slow wind. Studies by Hammond et al. (1996) and Graham et al. (2017) provide similar results as we move away from Sun (1 to 5.5 AU).

The above mentioned points guide us in interpreting the observed $\frac{T_{\perp h}}{T_{\parallel h}}$ values in the slow and fast wind and in turn the observed whistler waves.

The Strahl part is scattered more in the case of the slow wind than in the case of the fast wind, therefore there are a higher number of high energy Strahl particles that are becoming part of the halo in the case of the slow wind than in the fast wind.

Although, the slow wind Strahl part is broader than the fast wind Strahl at all the radial distances from the Sun, as we move farther from the Sun the Strahl part is relatively becoming broader both in the case of the slow and fast wind due to the pitch angle widening. Therefore, relatively higher number of particles are becoming a part of halo with the distance both in the case of slow and fast and we observe the increase in the $\frac{T_{\perp h}}{T_{\parallel h}}$ values.

Therefore, we propose that observed changes in $\frac{T_{\perp h}}{T_{\parallel h}}$ might be related to the Strahl scattering.

A feedback mechanism

One of the important questions is how is the Strahl part getting scattered and how is the energy transferred so that we have an increase in $\frac{T_{\perp h}}{T_{\parallel h}}$. The answer can be whistler waves itself. Studies by Kajdič et al. (2016) at 1 AU have shown that whistler waves are able to scatter the Strahl. These whistler waves can interact with Strahl electrons through electron cyclotron resonance. In the following, we have checked the energy ranges in which the whistler waves are able to interact resonantly.

Using the conditions for electron cyclotron resonance

$$\omega - \mathrm{k}_{\parallel}\mathrm{v}_{\parallel} = \omega_{ce}\,. \tag{5.11}$$

As we have discussed in chapter 2, the Strahl is a field aligned component, so the electrons of the Strahl part in most of the cases are field aligned, therefore when we look for the resonance of whistler waves with the Strahl electrons traveling at $v_{\parallel}$, we should be looking at the θ_{kB}, but not the θ_{kv}

$$\omega - \mathrm{kv}\cos(\theta_{kB}) = \omega_{ce}\,. \tag{5.12}$$

Condition for resonance is only satisfied when whistler waves travel opposite to the electrons as ω_{ce} is always greater than the frequency of the observed whistler waves, so for resonance to happen $\theta_{kB} > 90°$. We consider anti-parallel whistler waves $\cos(\theta_{kB}) \approx -1$. Observations of equal proportions of parallel and anti-parallel whistler waves, i.e. with in an angle of 20 °with $\mathbf{B}$ and $-\mathbf{B}$ of are shown in the studies of Stansby et al. (2016).

$$\omega + \mathrm{kv} = \omega_{ce}, \tag{5.13}$$

$$\frac{\mathrm{kv}}{\omega} = \frac{(\omega_{ce} - \omega)}{\omega} \tag{5.14}$$

$$v = (\frac{\omega_{ce}}{\omega} - 1)v_{\phi}, \tag{5.15}$$

$$E = \frac{1}{2} m_e v^2, \tag{5.16}$$

Equation 5.15 gives us the velocity of the electrons which can be resonant with the whistler waves. Using equation 5.16 we calculate the energies of electrons which can interact resonantly with the whistler waves and the distribution of energy of the resonant electrons is shown in Figure 5.27, as expected most of the resonant electron energies are in the range of Strahl. Therefore, from our rough calculations, we can understand that our observed whistler waves will be able to scatter the Strahl. Now the 2nd part of the question, how is the energy getting transferred?

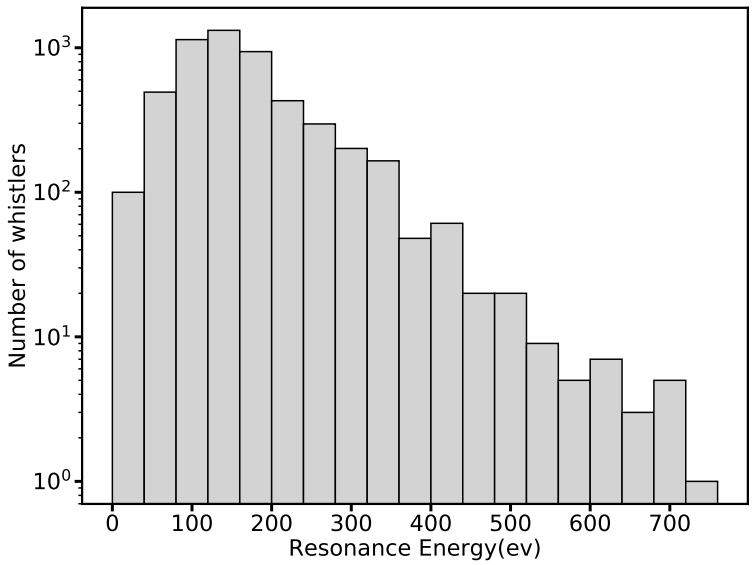

FIGURE 5.27: Resonant energy of the electrons interacting with the whistler waves (assuming the whistler waves are anti-parallel to the mean magnetic field).

Studies by Veltri and Zimbardo (1993) have shown that when resonantly interacting whistler waves scatter the electrons, energy is transferred from parallel to perpendicular direction, which increases the temperature in perpendicular direction. Therefore we can understand that whistler waves are able to scatter the Strahl and this scattered Strahl whose perpendicular energy is increased is becoming a part of the halo causing the $\frac{T_{\perp h}}{T_{\parallel h}}$ value to raise.

This is like a feedback mechanism,

- Whistler waves scatter the Strahl population.
- Scattered Strahl increases the value of $\frac{T_{\perp h}}{T_{\parallel h}}$.
- Increases in the $\frac{T_{\perp h}}{T_{\parallel h}}$ value favors the creation of the whistler waves and on.

However, the $\frac{T_{\perp h}}{T_{\parallel h}}$ values cannot keep on increasing without a limit as they are bounded by whistler temperature anisotropy instability thresholds as shown for a slow wind case in the Figure 5.28. This is the reason why we believe that there is saturation of $\frac{T_{\perp h}}{T_{\parallel h}}$ values farther from the Sun as shown in the Figures 5.24 and 5.25.

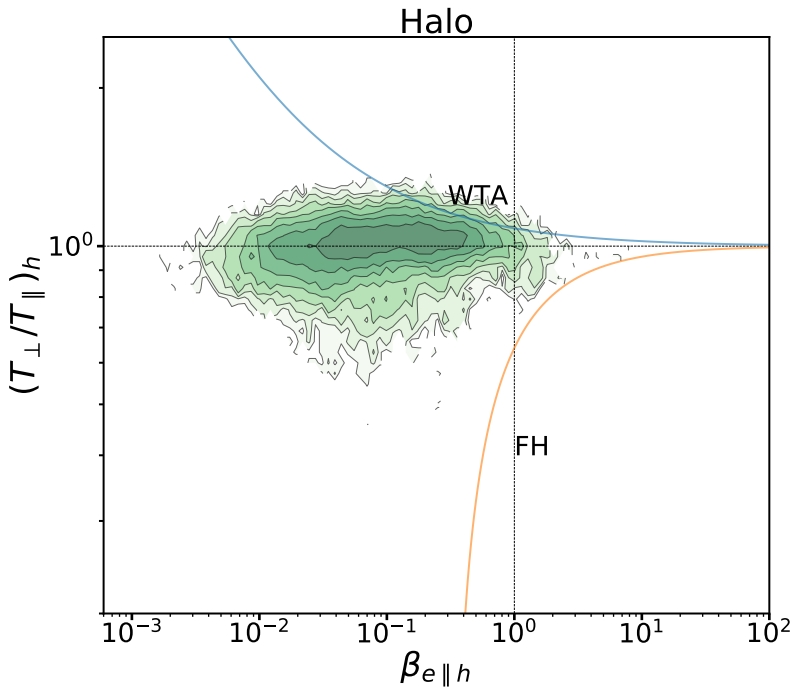

FIGURE 5.28: Counts histogram of the Halo electron anisotropy versus $\beta_{h\parallel}$ for all the observed slow wind shown as contours. The maximum growth rate curves for WTA ($\frac{\gamma}{\omega_e} = 10^{-3}$, $\kappa = 8$) and FH ($\frac{\gamma}{\omega_e} = 10^{-3}$, $\kappa = 8$) are taken from Lazar et al. (2018)

This constraining of $\frac{T_{\perp h}}{T_{\parallel h}}$ values below the instability thresholds gives us the signs that it is highly probable that WTA instability is acting and taking part in the whistler generation. This can also be seen in Figure 5.29 for the case when the whistlers are observed, the majority of the whistlers are closer to the threshold of whistler instability. However, this Figure has to be taken with caution as to increase the number of data points we have considered temperature values which are as far as 600 sec from the whistlers observed.

Eventhough our explanation appears to be a reasonable one, there are some issues related to it. The most important one is that whistler waves are not always anti-parallel to the mean magnetic field, they are dominantly observed propagating parallel too. Therefore the probability of whistler waves scattering the Strahl part decreases.

Another case is when the whistler waves are oblique. Recently, Vasko et al. (2019) using simulations has shown that highly oblique whistler waves drive the pitch-angle scattering of Strahl electrons and in turn isotropize the halo and also suppress the heat flux.

There are other possible sources as well to scatter the Strahl such as the Langmuir waves and others, see Kajdič et al. (2016) for a detailed description of the other possible candidates.

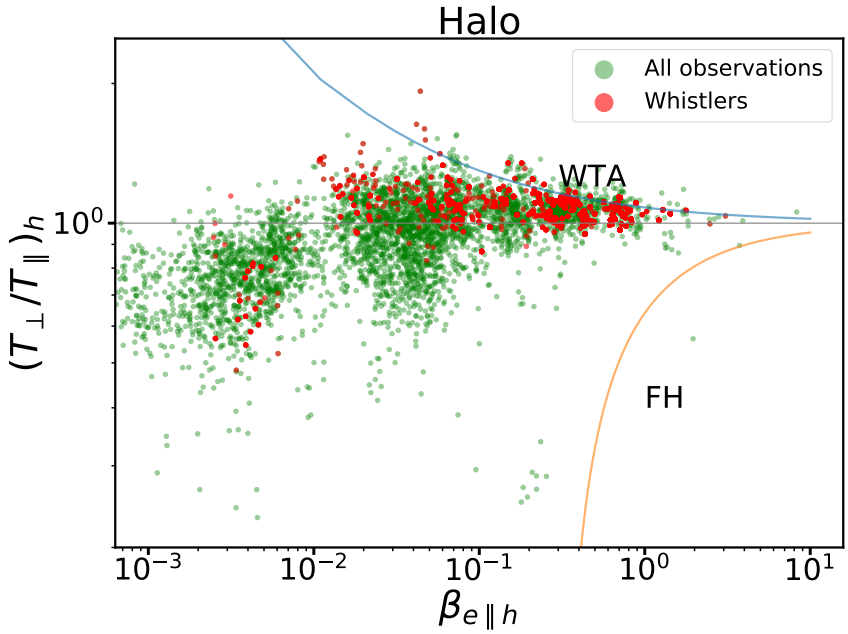

FIGURE 5.29: Halo electron anisotropy scatter plot as a function of $\beta_{h\parallel}$ during the presence of whistlers. The maximum growth rate curves for WTA ($\frac{\gamma}{\omega_e} = 10^{-3}$, $\kappa = 8$) and FH ($\frac{\gamma}{\omega_e} = 10^{-3}$, $\kappa = 8$) are taken from Lazar et al. (2018)

5.6 Conclusion

We have shown the presence of large amplitude whistler waves using the magnetic field PSD values in the range of $\sim 7 - 147$ Hz in the inner heliosphere, from 0.3 to 1 AU

Whistler waves are predominantly observed in the slow solar wind. The probability of whistler wave occurrence decreases as the velocity of the wind increases. Fast wind whistler waves are not observed closer to the Sun, but start to appear as we move farther from the Sun. The probability of whistler wave occurrence increases as we move farther from the Sun.

Our whistler observations might be able to explain the higher heat flux dissipation in the slow wind compared to the fast wind. Our observations could also possibly explain the presence of broader Strahl in the slow wind compared to the fast wind and their broadening with radial distance. The dominant presence of whistlers in the slow wind could also explain the higher $\frac{T_{\perp h}}{T_{\parallel h}}$ in the slow wind compared to the fast wind.

The amplitude of the observed whistler waves in the inner heliosphere is shown and the normalized amplitudes (with respect to $\langle B \rangle$) were found to be less than 0.01 for all the cases. For the whistler waves where the simultaneous electron measurements were available we found that $\frac{T_{\perp h}}{T_{\parallel h}} > 1$.

The $\frac{T_{\perp h}}{T_{\parallel h}}$ parameter, which is related to the development of the whistler instabilities is used as an indicator to study the observed whistler behaviors. We found a clear correlation between the $\frac{T_{\perp h}}{T_{\parallel h}}$ values and velocity and also the radial distance.

The value of $\langle \frac{T_{\perp h}}{T_{\parallel h}} \rangle$ and $\%\frac{T_{\perp h}}{T_{\parallel h}} > 1$ is higher in slow solar wind compared to the fast wind. The value of $\langle \frac{T_{\perp h}}{T_{\parallel h}} \rangle$ and $\%\frac{T_{\perp h}}{T_{\parallel h}} > 1$ increases as we move from 0.3 to 1 AU. There are plausible reasons behind the observed whistler behaviors. The Strahl is expected to be broader (scattered) typically in the slow wind and we have observed more number of whistler waves as compared to the case where the Strahl is expected to be narrow like in fast wind. The probability of whistler occurrence and the broadening of the Strahl are correlated. As Strahl broadening is increasing with the radial distance we observe an increase in the whistler presence.

We propose a possible mechanism that is causing the $\frac{T_{\perp h}}{T_{\parallel h}}$ values to vary in connection to the Strahl. We call this a feedback mechanism that we expect to explain the reasons behind all the observed whistler wave trends and parameters connected to them. The idea of this mechanism is still empirical and hypothetical. We would like to perform a simulation study in the future to validate our idea.

We showed that $\frac{T_{\perp h}}{T_{\parallel h}}$ values are bounded by the WTA instability threshold, which might be the reason that we did not observe a constant raise in $\frac{T_{\perp h}}{T_{\parallel h}}$ value after a certain point. This also points in a direction that WTA instability is generated.

A systematic study has to be done in the future, to identify which type of instability is acting in the whistler wave generation and what are the constraints on each of the instability and how they are evolving in the inner heliosphere. This can be done with the ongoing mission *Parker Solar Probe* (PSP) and the future one *Solar Orbiter* (SO), which have the capability to provide magnetic field waveform data of high resolution and high-resolution particle data.

From our study, we speculate that PSP and SO will observe a relatively low presence of whistler waves than what we have observed at 0.3 AU as we go closer to the Sun in the slow wind. For the fast wind case, whistler waves might not be observed,

even if they are observed it would be sparse. We also speculate the saturation of whistler wave occurrence above 5 AU both in the slow and fast solar wind.

5.7 Résumé en français: Ondes de type siffleur dans le vent solaire

Les ondes de type siffleur (whistler wave) sont couramment observées dans le milieu spatial et on fait l'objet de nombreuses études. Ces ondes interagissent avec les particles et peuvent donc avoir un impact considérable sur leur transport et plus généralement sur la thermodynamique du milieu.

L'observation de ces ondes requiert des mesures du champ magnétique (voire électrique) dans de fréquences comprises typiquement entre 1-100 Hz dans le vent solaire à 1 UA. Or cette plage de fréquences n'est pas systématiquement couverte par les satellites. Etonnamment, alors que la plupart des études sur les whistlers ont été effectuées dans le proche environnement terrestre, on ne sait quasiment rien de leur existence et de leurs caractéristiques à l'intérieur de l'héliosphère. A notre connaissance, notre étude est la première à fournir une description complète des whistlers entre 0.3 et 1 UA. Pour cela nous nous servons des mesures effectuées par le search-coil de *HELIOS* 1. Malheureusement cet instrument ne mesure que 1, voire 2 composantes du champ magnétique. Notre identification des whistlers repose donc uniquement sur la présence d'un excès de puissance spectrale dans la plage de fréquences où ces ondes sont attendues, entre f_{LH} et f_{ce}.

Dans cette étude nous décrivons les principales caractéristiques de ces ondes et montrons qu'elles sont nettement plus fréquentes dans le vent solaire lent. Leur taux d'apparition croît avec la distance du Soleil pour atteindre quelques pourcent dans le voisinage de la Terre.

Les mesures de la densité et vitesse électronique effectuées par *HELIOS* 1 nous permettent de déterminer quelles sont les conditions ls plus propices pour générer ces ondes. Nous trouvons que la condition $\frac{T_{\perp h}}{T_{\parallel h}} > 1$ soit être vérifiée pour observer des whistlers. Ceci suggère que l'instabilité d'anisotropie de température joue un rôle. La présence d'autres instabilités, telle que celle du flux de chaleur ne peut pas être exclue, comme le montre la récente étude de Tong et al. (2019b). Nous trouvons aussi que la présence de whistlers s'accompagne d'un étalement de la population d'électrons énergétiques dite Strahl.

Le mécanisme que nous proposons pour expliquer l'omniprésence de whistlers dans l'héliosphère interne fait appel à une rétroaction: l'instabilité d'anisotropie de température favorise le développement de whistlers, qui favorisent à leur tour l'étalement de la population Strahl par résonance cyclotronique électronique. Cette dernière favorise l'anisotropie de la température et offre donc des conditions favorables pour entretenir l'instabilité.

Chapter 6

Conclusion

6.1 Questions answered

The common thread of this thesis is the role of turbulence in the solar wind, with a particular focus on magnetic field fluctuations in the inner heliosphere.

Our initial starting point was a study of the radial evolution of the transition between f^{-1} and inertial ranges in turbulence. Most observational studies do so by working in the spectral domain. We wanted to constrain these results by working in the temporal domain by means of the Autocorrelation Function (ACF). This, however, made us realise that the ACF could not be meaningfully applied to solar wind turbulence data because of the non-stationarity of the latter. That study prompted what appears in Chapter 4 of this thesis. At the same time, we were uncovering old search-coil data from the *HELIOS* mission, which had barely been exploited so far. We discovered that whistler waves are seen all regions in the inner heliosphere and so decided to study why this was so. That study lead to Chapter 5. While working on whistler waves, we also investigated the spectral signature of turbulence at kinetic scales, which then lead to what is in Chapter 3. All these studies are based on in-situ measurements from the *HELIOS* (1974-1985) and *WIND* (1994-) missions.

The problem of determining whether the solar wind is stationary or not has received little attention so far. This is surprising as this has far-reaching consequences on our ability to study it with classical data analysis tools. In Chapter 4, we show how the ACF is strongly affected by non-stationarity, especially when the spectral index of the power spectral density (PSD) is located between -1 and -2, which is generally the case in the solar wind. We conclude that both the slow and the fast solar wind are non-stationary over a wide range of time scales (seconds to days). Therefore, the ACF should not be used for determining characteristic scales because it has a high variance and does not converge toward its true value, even for long records. A better alternative is multiscale (a.k.a wavelet) analysis.

Until recently, it was believed that the non-Alfvénic slow solar wind did not have a regime in which the power spectral density (PSD) would scale as $E_b \propto f^{-1}$ as it does in the fast wind. It was assumed that the slow wind would be released from the solar corona in a fully evolved turbulent state with the non-linear cascade already initiated at all scales. This may be one of the reasons why the solar wind community has never actively looked for a f^{-1} range in the slow wind.

Using long intervals of magnetic field data of non-Alfvénic slow winds from *WIND* at 1 AU we now find evidence for such a f^{-1} range for the first time and independently of the recent study by Bruno, R. et al. (2019). This helps in identifying the scales at which the non-linear energy cascade is initiated in the slow wind and in understanding the difference between the evolution of turbulence in slow and fast solar winds.

In most of the time intervals we considered the spectral break between fast and non-Alfvénic slow wind differs by 1 decade in frequency. In fast winds at 1 AU the spectral break occurs around 10^{-3} Hz and in non-Alfvénic slow winds at 1 AU around 10^{-4} Hz. Estimates of the non-linear time at the spectral break do not show any significant correlation with the expansion time. However, and surprisingly, the ratio $\frac{T_{nl}}{T_A}$ between the non-linear time and Alfvén time saturates to nearly the same value ($\sim 2-3$) for frequencies below the spectral break, regardless of the type of solar wind, and for winds observed between 0.3 and 1 AU. This suggests that the number of Alfvénic collisions needed for the turbulence cascade to be initiated is the same in the slow and fast wind. This is a surprising result, as the pure slow wind is non-Alfvénic. This also suggests that the evolution of low frequency turbulence is similar in slow and fast solar winds. We find that the $\frac{T_{nl}}{T_A}$ ratio actually depends on $\frac{\langle B \rangle}{\delta B}$ only and so it is the relative fluctuation level that may govern the non-linear time. These results are discussed in Chapter 3.

After considering frequencies shortward of the inertial range, we switched to higher frequencies in the kinetic range by using magnetic field spectra from the *HELIOS* 1 mission. This high-frequency range had never been thoroughly investigated in the inner heliosphere. First we find that an exponential model $E_b = Af^{-8/3}exp(-f/f_d)$ is capable of describing the shape of the PSD similar to what had been observed before by Alexandrova et al. (2012) at 1 AU. What is new, however, is the ability of this model to describe the spectrum with a set of local parameters such as electron Larmor frequency and amplitude of the magnetic field fluctuations from 0.3 to 1 AU. This points to the existence of some universality in the evolution of solar wind turbulence.

The kinetic range occasionally shows the presence of narrowband wave packets. We identify these as whistler waves even though the absence of polarisation measurements does not allow us to conclude in an unambiguous way. These whistler waves are primarily observed in the slow solar wind and are more sparse in the fast wind. Their rate of occurrence increases as we move away from the Sun. Simultaneous particle measurements show that such waves are more likely to occur when the temperature anisotropy $T_{\perp h}/T_{\parallel h}$ exceeds 1.

Based on the $T_{\perp h}/T_{\parallel h}$ values and width of the Strahl, we propose that the increase in $T_{\perp h}/T_{\parallel h}$ value might be related to the width of the Strahl electron population: a broader Strahl leads to a higher temperature anisotropy as more Strahl electrons become part of the halo population. Knowing that whistler waves are one of the important causes of Strahl broadening we propose a hypothetical feedback mechanism of whistler generation in which these waves scatter the Strahl, the scattered Strahl enhances the anisotropy, which in turn facilitates the generation of new waves.

From our analysis we predict that the percentage of whistlers should decrease as we move closer to the Sun in the slow wind; the probability of observing whistlers in the fast wind near the Sun should be very low. These results are detailed in Chapter 5.

6.2 Unanswered questions and future projects

The problems that have been addressed in this thesis inevitably raise new questions.

From our work we have understood that the initiation of non-linear energy cascade in the turbulent solar wind is dependent on the $\frac{T_{nl}}{T_A} \propto \frac{\langle B \rangle}{\delta B}$ ratio irrespective of the type of solar wind and of the distance from the Sun. However, in Alfvénic slow

winds at 0.3 AU this value was found to be higher than usually observed. The reason for this is unclear. Clearly, a more detailed statistical study is needed to determine what additional factors influence the initiation of non-linear cascade.

After understanding that the number of Alfvénic collisions required for the initiation of turbulence cascade is the same in the slow and fast wind, we would like to study why Alfvénic collisions are playing an important role in the non-Alfvénic slow wind turbulence cascade. Importantly, we would like to know what are the large scale structures that are making the f^{-1} region in the slow and the fast wind? What are the physical phenomena actually responsible for the creation of f^{-1}? Is there a difference in what these regions are made up of in different types of winds? The long observations of *WIND* and the long solar wind records of the OMNI database offer considerable potential for answering these questions.

We have shown how the frequency of the spectral break between the f^{-1} and inertial range is evolving radially in the fast wind. We would like to know how the spectral break frequency is radially evolving in the slow wind and how does it compare to previous fast wind studies ? This study will help us understand the difference between the radial evolution of turbulence in slow and fast wind. *HELIOS* is not able to provide the required data for our analysis. Using the data from *PARKER SOLAR PROBE* (PSP) and the upcoming mission *SOLAR ORBITER* (SO) we may be able to solve this problem. However, we have also understood from our turbulence analysis that giving a general picture for these evolutions is not that straightforward. We have to consider large number of parameters such as cross-helicity, compressibility, Alfvén velocity etc of the interval to be able to generalize the behavior and importantly lack of observations does not help our cause.

Another important question that came up while working on f^{-1} range was, what kind of spectral behavior should occur at even lower frequencies, where most of the energy injected in the solar wind. Until now we are not able to follow the solar wind erupting from the same region of the Sun for a very long time, we need a co-rotating satellites to do that. Using long intervals of data from the co-rotating satellites such as SO we might look into very low-frequencies and understand the physics there.

While working with the slow wind intervals in the inner heliosphere and at 1 AU, we came across an interesting phenomenon: we observed the presence of special density enhancements (Gosling et al., 1977) in the slow wind (no change in the velocity or the magnetic field values), which do not relate to structures such as magnetic clouds, current sheet crossing etc. These density enhancements seem to be inherently present in the slow wind and studying them might give us an understanding of the composition of the slow wind. There is not enough discussion about them in the literature. Therefore, we would like to explore in detail their presence, importantly their radial evolution and find the reasons for such sudden enhancements.

For the case of whistlers, first, we would like to validate our results and predictions made using the *HELIOS* data. Using the PSP and SO data we would like to validate our result that the occurrence probability of whistlers is highly dependent on the halo electron temperature anisotropy in the inner heliosphere. We would also like to validate our prediction of the decrease in the proportion of whistlers as we got closer to the Sun. Using the mission such as *ULYSSES* we would like to validate the saturation of the proportion of whistlers as we go beyond 1 AU. Importantly using the heat-flux measurements from PSP, SO and *ULYSSES* we would also like to investigate how the proportion of whistlers changes could be related to the anomalous radial scalings we observe in the energy content of the solar wind. The other

important future project for me is to coordinate with the simulation group working with the particles in the kinetic scale regime and to work on the proposed self-sustaining feedback mechanism for the whistler wave generation. It would be a big achievement for us if we could show that the whistler waves are generated with the proposed feedback mechanism. If the proposed mechanism is successful, we would like to use the simulation results and compare the results with the observations.

6.3 Résumé en français: Conclusion

Le fil conducteur de cette thèse est le rôle de la turbulence dans le vent solaire, avec un accent particulier sur les fluctuations du champ magnétique dans l'héliosphère interne.

Notre point de départ initial était une étude de l'évolution radiale de la transition entre le régime en f^{-1} et le régime inertiel dans la turbulence. La majorité des études caractérisent cette transition dans le domaine spectral. Nous voulions contraindre ces résultats en travaillant dans le domaine temporel au moyen de la fonction d'autocorrélation (ACF). Cela a toutefois révélé que l'ACF ne pouvait pas être appliquée aux données de turbulence du vent solaire en raison de la non-stationnarité de cette dernière. Cette étude a donné lieu au Chapitre 4 de cette thèse. En même temps, nous découvrions d'anciennes mesures du champ magnétique de la mission *HELIOS*, qui avaient été à peine exploitées jusqu'alors. Nous avons découvert que les ondes de type whistler étaient omniprésentes dans l'héliosphère intérieure et nous avons donc décidé d'étudier pourquoi il en était ainsi. Cette étude a donné lieu au Chapitre 5. Tout en travaillant sur les ondes de sifflement, nous avons également étudié la signature spectrale de la turbulence aux échelles cinétiques, ce qui a conduit au Chapitre 3. Toutes ces études sont basées sur des mesures in situ des missions *HELIOS* (1974-1985) et *WIND* (1994-).

La question de la stationnarité du vent solaire n'a jusqu'ici guère retenu l'attention. Or une non-stationnarité du vent pourrait avoir conséquences sérieuses sur notre capacité à caractériser le vent avec les outils classiques d'analyse de données.

Dans le Chapitre 4, nous confirmons que l'ACF est fortement affecté par la non-stationnarité, en particulier lorsque l'indice spectral de la densité spectrale de puissance (PSD) est se situe entre -1 et -2, ce qui est généralement le cas dans le vent solaire. Nous en concluons que les vents solaires lent et rapide sont tous deux non stationnaires sur une large gamme d'échelles de temps (de quelques secondes à quelques jours). Par conséquent, le recours à l'ACF est à proscrire pour déterminer des échelles caractéristiques. Une meilleure alternative serait l'analyse multi-échelle (par ondelettes).

On croyait jusque récemment que le vent solaire lent de type non-Alfvénique n'offrait pas de régime dans lequel la densité spectrale de puissance (DSP) puisse varier comme $E_b \propto f^{-1}$ comme c'est le cas dans le vent rapide. Cela pourrait être dû à la génération du vent lent dans un état turbulent évolué, contrairement au vent rapide dans lequel la cascade non-linéaire n'est pas encore entièrement amorcée. Ceci explique sans doute pourquoi la communauté n'a jamais cherché activement un régime en f^{-1} dans le vent lent.

Grâce aux longs intervalles de données de champ magnétique dans des vents lents non-Alfveniques fournis par le satellite *WIND* à 1 UA, nous montrons pour la première fois et indépendamment de l'étude récente de Bruno, R. et al. (2019) que le régime en f^{-1} existe bel et bien. Cela nous aide à mieux identifier l'échelle à laquelle la cascade non-linéaire démarre.

Nos estimations du temps non-linéaire ne montrent pas de corrélation significative avec le temps d'expansion du plasma. En revanche, le rapport $\frac{T_{nl}}{T_A}$ entre le temps non linéaire et le temps d'Alfvén sature à peu près à la même valeur ($\sim 2-3$), indépendamment du type de vent solaire, et quelle que soit la distance du Soleil comprise entre 0.3 et 1 UA. Cela suggère que l'évolution de la turbulence à basse fréquence serait comparable dans les vents solaires lents et rapides. Nous trouvons que le rapport dépend essentiellement de $\frac{\langle B \rangle}{\delta B}$. Ce serait donc le niveau de fluctuation relatif qui régirait le temps non linéaire. Ces points sont abordés dans le Chapitre 3.

Nous sommes ensuite passés aux fréquences les plus élevées, dans le régime cinétique. Les spectres de champ magnétique à haute fréquence sont issus de la mission *HELIOS* 1. Ces hautes fréquences n'avaient jamais fait l'objet d'études approfondies dans l'héliosphère interne. Tout d'abord, nous trouvons qu'un modèle exponentiel $E_b = Af^{-8/3}exp(-f/f_d)$ est capable de décrire la forme de la PSD de manière comparable à ce que Alexandrova et al. (2012) avait fait à 1 UA. Or, ce qui est nouveau, est la capacité de ce modèle à décrire le spectre avec le même ensemble de paramètres locaux depuis 0.3 à 1 UA. Cela suggère l'existence d'une universalité dans l'évolution de la turbulence du vent solaire.

La régime cinétique révèle occasionnellement la présence de paquets d'ondes à faible largeur de bande. Nous les identifions comme des ondes de type whistler, même si l'absence de mesures de polarisation ne nous permet pas de conclure de manière univoque. Ces ondes sont principalement observées dans le vent solaire lent. Elles sont plus rares dans le vent rapide. Leur fréquence augmente à mesure que nous nous éloignons du Soleil. Des mesures simultanées des électrons montrent que ces ondes sont plus susceptibles de se produire lorsque l'anisotropie de température $T_{\perp h}/T_{\parallel h}$ dépasse 1, indépendamment des conditions du vent solaire.

Sur cette base, nous suggérons que l'augmentation de la valeur $T_{\perp h}/T_{\parallel h}$ serait liée à la largeur de la population d'électrons de type Strahl. Nous proposons un mécanisme rétroactif de la génération des ondes de type whistler dans lequel ces ondes dispersent le Strahl, le Strahl dispersé augmente l'anisotropie, ce qui facilite enfin la génération de nouvelles ondes.

D'après notre analyse, le pourcentage de siffleurs devrait diminuer à mesure que nous nous rapprochons du Soleil dans le vent lent; la probabilité d'observer des whistlers dans le vent rapide à proximité du Soleil devrait être très faible. Ces résultats sont détaillés dans le Chapitre 5.

References

Abry, P., P. Goncalves, and P. Flandrin (1995). "Wavelets, spectrum analysis and 1/f processes". In: *Wavelets in statistics*. Ed. by A. Antoniadis and G. Oppenheim. Vol. 103. Lecture Notes in Statistics. Berlin: Springer Verlag, pp. 15–29.

Acuña, M. H. (Nov. 2002). "Space-based magnetometers". In: *Review of Scientific Instruments* 73, pp. 3717–3736. DOI: 10.1063/1.1510570.

Alexandrova, O. et al. (2009). "Universality of Solar-Wind Turbulent Spectrum from MHD to Electron Scales". In: *Physical Review Letters* 103.16, 165003, p. 165003. DOI: 10.1103/PhysRevLett.103.165003. arXiv: 0906.3236 [physics.plasm-ph].

Alexandrova, O. et al. (Dec. 2012). "Solar Wind Turbulent Spectrum at Plasma Kinetic Scales". In: *The Astrophysical Journal* 760, 121, p. 121. DOI: 10.1088/0004-637X/760/2/121. arXiv: 1212.0412 [astro-ph.SR].

Alexandrova, O. et al. (Oct. 2013). "Solar Wind Turbulence and the Role of Ion Instabilities". In: *Space Science Reviews* 178, pp. 101–139. DOI: 10.1007/s11214-013-0004-8. arXiv: 1306.5336 [astro-ph.SR].

Alexandrova, O. et al. (2019). "Kinetic scales turbulence in space plasmas observed in the near-Earth and near-Sun solar wind". In: *Nature Communications:Submitted*.

Artemyev, A. et al. (Apr. 2016). "Oblique Whistler-Mode Waves in the Earth's Inner Magnetosphere: Energy Distribution, Origins, and Role in Radiation Belt Dynamics". In: *Space Science Reviews* 200.1-4, pp. 261–355. DOI: 10.1007/s11214-016-0252-5.

Balogh, A. et al. (Dec. 2014). "Introduction to the Solar Activity Cycle: Overview of Causes and Consequences". In: 186, pp. 1–15. DOI: 10.1007/s11214-014-0125-8.

Bartlett, M. S. (1946). "On the Theoretical Specification and Sampling Properties of Autocorrelated Time-Series". In: *Supplement to the Journal of the Royal Statistical Society* 8.1, pp. 27–41. ISSN: 14666162.

Bavassano, B. et al. (May 1982). "Radial evolution of power spectra of interplanetary Alfvenic turbulence". In: 87, pp. 3617–3622. DOI: 10.1029/JA087iA05p03617.

Beinroth, H. J. and F. M. Neubauer (Sept. 1981). "Properties of whistler mode waves between 0.3 and 1.0 AU from HELIOS observations". In: *Journal of Geophysical Research* 86, pp. 7755–7760. DOI: 10.1029/JA086iA09p07755.

Bellan, P. M. (Jan. 2006). *Fundamentals of Plasma Physics*. Cambridge,UK: Cambridge University Press.

Bendat, J. S. and A. G. Piersol (2000). *Random Data Analysis and Measurement Procedures*. New York: Wiley, London.

Beran, Jan (1994). *Statistics for long-memory processes*. New York: Chapman and Hall.

Beran, Jan et al. (2016). *Long-Memory Processes: Probabilistic Properties and Statistical Methods*. New York: Springer.

Berčič, L. et al. (2019). "Scattering of strahl electrons in the solar wind between 0.3 and 1 au: Helios observations". In: 486.3, pp. 3404–3414. DOI: 10.1093/mnras/stz1007. arXiv: 1904.08272 [physics.space-ph].

Boldyrev, S. and J. C. Perez (Oct. 2012). "Spectrum of Kinetic-Alfvén Turbulence". In: *The Astrophysical Journal Letters* 758, L44, p. L44. DOI: 10.1088/2041-8205/758/2/L44. arXiv: 1204.5809 [astro-ph.SR].

Borgnat, P. and P. Flandrin (Jan. 2009). "Stationarization via surrogates". In: *Journal of Statistical Mechanics: Theory and Experiment* 1.P01001, pp. 1–14. DOI: 10.1088/1742-5468/2009/01/P01001.

Borovsky, J. E. (Aug. 2008). "Flux tube texture of the solar wind: Strands of the magnetic carpet at 1 AU?" In: *Journal of Geophysical Research (Space Physics)* 113, A08110, p. 8110. DOI: 10.1029/2007JA012684.

Borovsky, Joseph E. et al. (1997). "The Earth's plasma sheet as a laboratory for flow turbulence in high-[beta] MHD". In: *Journal of Plasma Physics* 57.1, pp. 1–34. DOI: 10.1017/S0022377896005259.

Bothmer, V. and R. Schwenn (Jan. 1998). "The structure and origin of magnetic clouds in the solar wind". In: *Annales Geophysicae* 16, pp. 1–24. DOI: 10.1007/s00585-997-0001-x.

Bourouaine, S. et al. (Apr. 2012). "On Spectral Breaks in the Power Spectra of Magnetic Fluctuations in Fast Solar Wind between 0.3 and 0.9 AU". In: 749, 102, p. 102. DOI: 10.1088/0004-637X/749/2/102.

Bourouaine, Sofiane and Jean C. Perez (2018). "On the Limitations of Taylor's Hypothesis in Parker Solar Probe's Measurements near the Alfvén Critical Point". In: *The Astrophysical Journal Letters* 858.2, p. L20. URL: http://stacks.iop.org/2041-8205/858/i=2/a=L20.

Breech, B. et al. (Sept. 2009). "Electron and proton heating by solar wind turbulence". In: *Journal of Geophysical Research (Space Physics)* 114, A09103, A09103. DOI: 10.1029/2009JA014354. arXiv: 0907.4074 [astro-ph.SR].

Breneman, A. et al. (Aug. 2010). "Observations of large-amplitude, narrowband whistlers at stream interaction regions". In: *Journal of Geophysical Research (Space Physics)* 115, A08104, A08104. DOI: 10.1029/2009JA014920.

Bruno, R. and V. Carbone (Sept. 2013a). "The Solar Wind as a Turbulence Laboratory". In: *Living Reviews in Solar Physics* 2, p. 4. DOI: 10.12942/lrsp-2013-2.

— (May 2013b). "The Solar Wind as a Turbulence Laboratory". In: *Living Reviews in Solar Physics* 10, 2, p. 2. DOI: 10.12942/lrsp-2013-2.

Bruno, R. and L. Trenchi (June 2014). "Radial Dependence of the Frequency Break between Fluid and Kinetic Scales in the Solar Wind Fluctuations". In: *The Astrophysical Journal Letters* 787, L24, p. L24. DOI: 10.1088/2041-8205/787/2/L24. arXiv: 1404.2191 [astro-ph.SR].

Bruno, Roberto (2019). "Intermittency in Solar Wind Turbulence From Fluid to Kinetic Scales". In: *Earth and Space Science* 6.5, pp. 656–672. DOI: 10.1029/2018EA000535. URL: https://agupubs.onlinelibrary.wiley.com/doi/abs/10.1029/2018EA000535.

Bruno, Roberto and Vincenzo Carbone (2016). *Turbulence in the solar wind*. Vol. 928. Lecture notes in physics. Switzerland: Springer International Publishing. DOI: 10.1007/978-3-319-43440-7.

Bruno, R. et al. (2019). "The low-frequency break observed in the slow solar wind magnetic spectra". In: *A&A* 627, A96. DOI: 10.1051/0004-6361/201935841. URL: https://doi.org/10.1051/0004-6361/201935841.

Chen, C. H. K. et al. (July 2012). "Density Fluctuation Spectrum of Solar Wind Turbulence between Ion and Electron Scales". In: *Physical Review Letters* 109.3, 035001, p. 035001. DOI: 10.1103/PhysRevLett.109.035001. arXiv: 1205.5063 [physics.space-ph].

Chew, G. F., M. L. Goldberger, and F. E. Low (July 1956). "The Boltzmann Equation and the One-Fluid Hydromagnetic Equations in the Absence of Particle Collisions". In: *Proceedings of the Royal Society of London Series A* 236, pp. 112–118. DOI: 10.1098/rspa.1956.0116.

Clauset, A., C. Rohilla Shalizi, and M. E. J. Newman (June 2009). "Power-law distributions in empirical data". In: *SIAM Review* 51, pp. 661–703. DOI: 10.1137/070710111.

Coleman Jr., P. J. (Aug. 1968). "Turbulence, Viscosity, and Dissipation in the Solar-Wind Plasma". In: 153, p. 371. DOI: 10.1086/149674.

Cornilleau-Wehrlin, N. et al. (Feb. 2003). "First results obtained by the Cluster STAFF experiment". In: *Annales Geophysicae* 21, pp. 437–456.

Cranmer, S. R. et al. (Apr. 2015). "The role of turbulence in coronal heating and solar wind expansion". In: *Philosophical Transactions of the Royal Society of London Series A* 373, pp. 20140148–20140148. DOI: 10.1098/rsta.2014.0148. arXiv: 1412.2307 [astro-ph.SR].

Dehmel, G. et al. (1975). "Das Induktionsspulen-Magnetometer-Experiment (E4)". In: *Raumfahrtforschung* 19.5, pp. 241–243.

Dehmel, G. et al. (Oct. 1975). "The Induction Coil Magnetometer Experiment /E 4/". In: *Raumfahrtforschung* 19, pp. 241–244.

Denskat, K. U., H. J. Beinroth, and F. M. Neubauer (1983). "Interplanetary magnetic field power spectra with frequencies from 2.4 X 10 to the -5th HZ to 470 HZ from HELIOS-observations during solar minimum conditions". In: *Journal of Geophysics Zeitschrift Geophysik* 54, pp. 60–67.

Denskat, K. U. and F. M. Neubauer (Apr. 1982). "Statistical properties of low-frequency magnetic field fluctuations in the solar wind from 0.29 to 1.0 AU during solar minimum conditions - HELIOS 1 and HELIOS 2". In: 87, pp. 2215–2223. DOI: 10.1029/JA087iA04p02215.

Dudok de Wit, T. et al. (Oct. 2013). "Methods for Characterising Microphysical Processes in Plasmas". In: 178, pp. 665–693. DOI: 10.1007/s11214-013-9974-9. arXiv: 1306.5303 [physics.plasm-ph].

Feldman, W. C. et al. (Nov. 1975). "Solar wind electrons". In: *Journal of Geophysical Research* 80, pp. 4181–4196. DOI: 10.1029/JA080i031p04181.

Frisch, U. (1995). *Turbulence, the legacy of A. N. Kolmogorov*. Cambridge: Cambridge University Press.

Galtier, S., A. Pouquet, and A. Mangeney (Sept. 2005). "On spectral scaling laws for incompressible anisotropic magnetohydrodynamic turbulence". In: *Physics of Plasmas* 12.9, 092310, p. 092310. DOI: 10.1063/1.2052507. eprint: physics/0504207.

Gary, S. P. (Sept. 1993). *Theory of Space Plasma Microinstabilities*. Cambridge,UK: Cambridge University Press.

Gary, S. P. and W. C. Feldman (Mar. 1977). "Solar wind heat flux regulation by the whistler instability". In: *Journal of Geophysical Research* 82, pp. 1087–1094. DOI: 10.1029/JA082i007p01087.

Gary, S. P., R. M. Skoug, and W. Daughton (June 1999). "Electron heat flux constraints in the solar wind". In: *Physics of Plasmas* 6, pp. 2607–2612. DOI: 10.1063/1.873532.

Gary, S. P. et al. (Dec. 1994). "The whistler heat flux instability: Threshold conditions in the solar wind". In: *Journal of Geophysical Research* 99, p. 23. DOI: 10.1029/94JA02067.

Goldstein, M. L., D. A. Roberts, and C. A. Fitch (June 1994). "Properties of the fluctuating magnetic helicity in the inertial and dissipation ranges of solar wind turbulence". In: *Journal of Geophysical Research* 99, pp. 11519–11538. DOI: 10.1029/94JA00789.

Goldstein, M. L., D. A. Roberts, and W. H. Matthaeus (1995). "Magnetohydrodynamic Turbulence In The Solar Wind". In: *Annual Review Astronomy Astrophysics* 33, pp. 283–326. DOI: 10.1146/annurev.aa.33.090195.001435.

Goldstein, M. L. et al. (Apr. 2015). "Kinetic scale turbulence and dissipation in the solar wind: key observational results and future outlook". In: *Philosophical Transactions of the Royal Society of London Series A* 373, pp. 20140147–20140147. DOI: 10.1098/rsta.2014.0147.

Gosling, J. T. (Nov. 2012). "Magnetic Reconnection in the Solar Wind". In: 172, pp. 187–200. DOI: 10.1007/s11214-011-9747-2.

Gosling, J. T. et al. (Nov. 1977). "Noncompressive density enhancements in the solar wind". In: *Journal of Geophysical Research* 82, pp. 5005–5010. DOI: 10.1029/JA082i032p05005.

Gosling, J. T. et al. (Jan. 2005). "Direct evidence for magnetic reconnection in the solar wind near 1 AU". In: *Journal of Geophysical Research (Space Physics)* 110, A01107, A01107. DOI: 10.1029/2004JA010809.

Graham, G. A. et al. (Apr. 2017). "The evolution of solar wind strahl with heliospheric distance". In: *Journal of Geophysical Research (Space Physics)* 122, pp. 3858–3874. DOI: 10.1002/2016JA023656.

Hammond, C. M. et al. (Dec. 1996). "Variation of electron-strahl width in the high-speed solar wind: ULYSSES observations." In: *Astronomy and Astrophysics* 316, pp. 350–354.

Hapgood, M. A. (May 1992). "Space physics coordinate transformations - A user guide". In: *Planetary and Space Science* 40, pp. 711–717. DOI: 10.1016/0032-0633(92)90012-D.

Hathaway, D. H. (Sept. 2015). "The Solar Cycle". In: *Living Reviews in Solar Physics* 12, 4, p. 4. DOI: 10.1007/lrsp-2015-4. arXiv: 1502.07020 [astro-ph.SR].

Hooge, F. N. and P. A. Bobbert (Feb. 1997). "On the correlation function of 1/f noise". In: *Physica B Condensed Matter* 239, pp. 223–230. DOI: 10.1016/S0921-4526(97)00332-3.

Hooge, F. N., T. G. M. Kleinpenning, and L. K. J. Vandamme (May 1981). "Experimental studies on 1/f noise". In: *Reports on Progress in Physics* 44, pp. 479–532. DOI: 10.1088/0034-4885/44/5/001.

Horbury, T. S., M. A. Forman, and S. Oughton (Dec. 2005). "Spacecraft observations of solar wind turbulence: an overview". In: *Plasma Physics and Controlled Fusion* 47, B703–B717. DOI: 10.1088/0741-3335/47/12B/S52.

Hospodarsky, G. B. (Dec. 2016). "Spaced-based search coil magnetometers". In: *Journal of Geophysical Research (Space Physics)* 121, p. 12. DOI: 10.1002/2016JA022565.

Howes, G. G. et al. (Nov. 2006). "Astrophysical Gyrokinetics: Basic Equations and Linear Theory". In: *The Astrophysical Journal* 651, pp. 590–614. DOI: 10.1086/506172. eprint: astro-ph/0511812.

Isaacs, J. J., J. A. Tessein, and W. H. Matthaeus (Feb. 2015a). "Systematic averaging interval effects on solar wind statistics". In: *Journal of Geophysical Research (Space Physics)* 120, pp. 868–879. DOI: 10.1002/2014JA020661.

— (Feb. 2015b). "Systematic averaging interval effects on solar wind statistics". In: *Journal of Geophysical Research (Space Physics)* 120, pp. 868–879. DOI: 10.1002/2014JA020661.

Kajdič, P. et al. (Dec. 2016). "Suprathermal Electron Strahl Widths in the Presence of Narrow-band Whistler Waves in the Solar Wind". In: *The Astrophysical Journal* 833, 172, p. 172. DOI: 10.3847/1538-4357/833/2/172. arXiv: 1701.04819 [physics.space-ph].

Kasdin, N. J. (1995). "Discrete simulation of colored noise and stochastic processes and 1/f alpha; power law noise generation". In: *Proceedings of the IEEE* 83.5, pp. 802–827. ISSN: 0018-9219. DOI: 10.1109/5.381848.

Keshner, M. S. (1982). "1/f Noise". In: *Proceedings of the IEEE* 70, pp. 212–218.

King, J. H. and N. E. Papitashvili (Feb. 2005). "Solar wind spatial scales in and comparisons of hourly Wind and ACE plasma and magnetic field data". In: *Journal of Geophysical Research (Space Physics)* 110, A02104, A02104. DOI: 10.1029/2004JA010649.

Kiyani, Khurom H., Kareem T. Osman, and Sandra C. Chapman (Apr. 2015). "Dissipation and heating in solar wind turbulence: from the macro to the micro and back again". In: *Philosophical Transactions of the Royal Society of London A: Mathematical, Physical and Engineering Sciences* 373.2041. DOI: 10.1098/rsta.2014.0155. URL: http://rsta.royalsocietypublishing.org/content/373/2041/20140155.abstract.

Klein, K. G., G. G. Howes, and J. M. TenBarge (Aug. 2014). "The Violation of the Taylor Hypothesis in Measurements of Solar Wind Turbulence". In: 790, L20, p. L20. DOI: 10.1088/2041-8205/790/2/L20. arXiv: 1406.5470 [physics.space-ph].

Klein, L. W. et al. (1992). "Evolution of spatial and temporal correlations in the solar wind - Observations and interpretation". In: *Solar Wind Seven Colloquium*. Ed. by E. Marsch and R. Schwenn, pp. 197–200.

Krishna Jagarlamudi, V. et al. (Jan. 2019). "Inherentness of Non-stationarity in Solar Wind". In: *The Astrophysical Journal* 871, 68, p. 68. DOI: 10.3847/1538-4357/aaef2e.

Kruparova, O. et al. (Aug. 2013). "Automated interplanetary shock detection and its application to Wind observations". In: *Journal of Geophysical Research (Space Physics)* 118, pp. 4793–4803. DOI: 10.1002/jgra.50468.

Lacombe, C. et al. (Nov. 2014). "Whistler Mode Waves and the Electron Heat Flux in the Solar Wind: Cluster Observations". In: *The Astrophysical Journal* 796, 5, p. 5. DOI: 10.1088/0004-637X/796/1/5.

Lazar, M. et al. (Feb. 2018). "Temperature anisotropy instabilities stimulated by the interplay of the core and halo electrons in space plasmas". In: *Physics of Plasmas* 25.2, 022902, p. 022902. DOI: 10.1063/1.5016261.

Leamon, R. J. et al. (Mar. 1998). "Observational constraints on the dynamics of the interplanetary magnetic field dissipation range". In: *SpaJournal of Geophysical Researchce Science Reviews* 103, p. 4775. DOI: 10.1029/97JA03394.

Lepping, R. P. et al. (Feb. 1995). "The Wind Magnetic Field Investigation". In: *Space Science Reviews* 71, pp. 207–229. DOI: 10.1007/BF00751330.

Lilensten, J. and J. Bornarel (Dec. 2005). *Space Weather, Environment and Societies*. Springer Verlag, Berlin.

Lilensten, J. et al. (Nov. 2014). "What characterizes planetary space weather?" In: *The Astronomy and Astrophysics Review* 22.79, 79, pp. 1–39. DOI: 10.1007/s00159-014-0079-6.

Lin, R. P. et al. (1995). "A three-dimensional plasma and energetic particle investigation for the wind spacecraft". In: *Space Science Reviews* 71.1, pp. 125–153. ISSN: 1572-9672. DOI: 10.1007/BF00751328. URL: https://doi.org/10.1007/BF00751328.

Lion, S., O. Alexandrova, and A. Zaslavsky (June 2016). "Coherent Events and Spectral Shape at Ion Kinetic Scales in the Fast Solar Wind Turbulence". In: *The Astrophysical Journal* 824, 47, p. 47. DOI: 10.3847/0004-637X/824/1/47. arXiv: 1602.07213 [astro-ph.SR].

Lumley, John L (1970). *Stochastic tools in turbulence*. Academic Press.

Maksimovic, M. et al. (2005). "Radial evolution of the electron distribution functions in the fast solar wind between 0.3 and 1.5 AU". In: *Journal of Geophysical Research: Space Physics* 110.A9. DOI: 10.1029/2005JA011119.

Maksimovic, M. et al. (Sept. 2005). "Radial evolution of the electron distribution functions in the fast solar wind between 0.3 and 1.5 AU". In: *Journal of Geophysical Research (Space Physics)* 110, A09104, A09104. DOI: 10.1029/2005JA011119.

Maksimovic, M. et al. (2019). " Predictions of the plasma parameters for the Parker Solar Probe using the extrapolations from the Helios observations". In: *In Preparation*.

Mallat, S. (2008). *A Wavelet Tour of Signal Processing: the Sparse Way*. 3rd. London: Academic Press. ISBN: 0123743702.

Marquette, Melissa L. et al. (2018). "Autocorrelation Study of Solar Wind Plasma and IMF Properties as Measured by the MAVEN Spacecraft". In: *Journal of Geophysical Research: Space Physics* 123.4, pp. 2493–2512. DOI: 10.1002/2018JA025209. eprint: https://agupubs.onlinelibrary.wiley.com/doi/pdf/10.1002/2018JA025209. URL: https://agupubs.onlinelibrary.wiley.com/doi/abs/10.1002/2018JA025209.

Marsch, E. et al. (Jan. 1982). "Solar wind protons - Three-dimensional velocity distributions and derived plasma parameters measured between 0.3 and 1 AU". In: *SpaJournal of Geophysical Researchce Science Reviews* 87, pp. 52–72. DOI: 10.1029/JA087iA01p00052.

Marsch, E. et al. (Apr. 1983). "On the equation of state of solar wind ions derived from HELIOS measurements". In: 88, pp. 2982–2992. DOI: 10.1029/JA088iA04p02982.

Marsch, Eckart (2010). "Helios: Evolution of Distribution Functions 0.3–1 AU". In: *Space Science Reviews* 172.1-4, 23–39. DOI: 10.1007/s11214-010-9734-z.

Matteini, L. et al. (2018). "On the 1/f Spectrum in the Solar Wind and Its Connection with Magnetic Compressibility". In: 869.2, L32, p. L32. DOI: 10.3847/2041-8213/aaf573. arXiv: 1812.05716 [physics.space-ph].

Matthaeus, W. H. and M. L. Goldstein (Dec. 1982). "Stationarity of magnetohydrodynamic fluctuations in the solar wind". In: *Journal of Geophysical Research* 87, pp. 10347–10354. DOI: 10.1029/JA087iA12p10347.

— (July 1986). "Low-frequency 1/f noise in the interplanetary magnetic field". In: *Physical Review Letters* 57, pp. 495–498. DOI: 10.1103/PhysRevLett.57.495.

Matthaeus, W. H., C. W. Smith, and S. Oughton (Apr. 1998). "Dynamical age of solar wind turbulence in the outer heliosphere". In: *Journal of Geophysical Research (Space Physics)* 103, p. 6495. DOI: 10.1029/97JA03729.

Matthaeus, W. H. et al. (Dec. 2005). "Spatial Correlation of Solar-Wind Turbulence from Two-Point Measurements". In: *Physical Review Letters* 95.23, 231101, p. 231101. DOI: 10.1103/PhysRevLett.95.231101.

Matthaeus, W. H. et al. (Aug. 2014). "Nonlinear and Linear Timescales near Kinetic Scales in Solar Wind Turbulence". In: *The Astrophysical Journal* 790, 155, p. 155. DOI: 10.1088/0004-637X/790/2/155. arXiv: 1404.6569 [physics.space-ph].

Matthaeus, W. H. et al. (Apr. 2015). "Intermittency, nonlinear dynamics and dissipation in the solar wind and astrophysical plasmas". In: *Philosophical Transactions of the Royal Society of London A: Mathematical, Physical and Engineering Sciences* 373.2041. DOI: 10.1098/rsta.2014.0154. URL: http://rsta.royalsocietypublishing.org/content/373/2041/20140154.abstract.

McComas, D. J. et al. (Sept. 2008). "Weaker solar wind from the polar coronal holes and the whole Sun". In: *Geophysical Research Letters* 35, L18103, p. L18103. DOI: 10.1029/2008GL034896.

Meyer-Vernet, N. (Sept. 2012). *Basics of the Solar Wind*. Cambridge Atmospheric and Space Science Series. Cambridge Univeristy Press.

Miles, D. M. et al. (Oct. 2018). "A hybrid fluxgate and search coil magnetometer concept using a racetrack core". In: *Geoscientific Instrumentation, Methods and Data Systems* 7, pp. 265–276. DOI: 10.5194/gi-7-265-2018.

Munteanu, C. et al. (Apr. 2016). "Effect of data gaps: comparison of different spectral analysis methods". In: *Annales Geophysicae* 34, pp. 437–449. DOI: 10.5194/angeo-34-437-2016.

Musmann, G., F. M. Neubauer, and E. Lammers (1977). "Radial variation of the interplanetary magnetic field between 0.3 AU and 1.0 AU". In: *Journal of Geophysics Zeitschrift Geophysik* 42, pp. 591–598.

Musmann, G. et al. (Oct. 1975). "The Foerstersonden magnetic field experiment /E 2/". In: *Raumfahrtforschung* 19, pp. 232–237.

Narita, Y. (May 2017). "Review article: Wave analysis methods for space plasma experiment". In: *Nonlinear Processes in Geophysics* 24, pp. 203–214. DOI: 10.5194/npg-24-203-2017.

Ness, N. F. (Nov. 1970). "Magnetometers for Space Research". In: *Space Science Reviews* 11, pp. 459–554. DOI: 10.1007/BF00183028.

Neubauer, F. M., G. Musmann, and G. Dehmel (Aug. 1977). "Fast magnetic fluctuations in the solar wind - HELIOS I". In: *SpaJournal of Geophysical Researchce Science Reviews* 82, pp. 3201–3212. DOI: 10.1029/JA082i022p03201.

Neubauer, F. M. et al. (1977). "Initial results from the Helios-1 search-coil magnetometer experiment". In: *Journal of Geophysics Zeitschrift Geophysik* 42, pp. 599–614.

Nicol, R. M., S. C. Chapman, and R. O. Dendy (Oct. 2009). "Quantifying the Anisotropy and Solar Cycle Dependence of 1/f" Solar Wind Fluctuations Observed by Advanced Composition Explorer". In: *The Astrophysical Journal* 703, pp. 2138–2151.

Ogilvie, K. W. et al. (Feb. 1995). "SWE, A Comprehensive Plasma Instrument for the Wind Spacecraft". In: *Space Science Reviews* 71, pp. 55–77. DOI: 10.1007/BF00751326.

Papoulis, Athanasios and S. Unnikrishna Pillai (2002). *Probability, Random Variables and Stochastic Processes*. 4th. McGraw-Hill Europe.

Parker, E. N. (Nov. 1958). "Dynamics of the Interplanetary Gas and Magnetic Fields." In: *The Astrophysical Journal* 128, p. 664. DOI: 10.1086/146579.

Perri, S. and A. Balogh (May 2010). "Stationarity in Solar Wind Flows". In: *The Astrophysical Journal* 714, pp. 937–943. DOI: 10.1088/0004-637X/714/1/937.

Perrone, D. et al. (Mar. 2019). "Radial evolution of the solar wind in pure high-speed streams: HELIOS revised observations". In: *Monthly Notices of the Royal Astronomical Society* 483, pp. 3730–3737. DOI: 10.1093/mnras/sty3348. arXiv: 1810.04014 [physics.space-ph].

Phan, T. D. et al. (Jan. 2006). "A magnetic reconnection X-line extending more than 390 Earth radii in the solar wind". In: 439, pp. 175–178. DOI: 10.1038/nature04393.

Pilipp, W. G. et al. (Feb. 1987). "Characteristics of electron velocity distribution functions in the solar wind derived from the HELIOS plasma experiment". In: *SpaJournal of Geophysical Researchce Science Reviews* 92, pp. 1075–1092. DOI: 10.1029/JA092iA02p01075.

Pilipp, W. G. et al. (May 1990). "Large-scale variations of thermal electron parameters in the solar wind between 0.3 and 1 AU". In: 95, pp. 6305–6329. DOI: 10.1029/JA095iA05p06305.

Podesta, J. J., A. B. Galvin, and C. J. Farrugia (Sept. 2008). "Correlation length of large-scale solar wind velocity fluctuations measured tangent to the Earth's orbit:

First results from Stereo". In: *Journal of Geophysical Research (Space Physics)* 113, A09104, A09104. DOI: 10.1029/2007JA012865.

Podesta, J. J. and D. A. Roberts (Sept. 2005). "Statistical Stationarity of Solar Wind Time Series". In: *Solar Wind 11/SOHO 16, Connecting Sun and Heliosphere*. Ed. by B. Fleck, T. H. Zurbuchen, and H. Lacoste. Vol. 592. ESA Special Publication, p. 531.

Porsche, H. (Nov. 1981). "HELIOS mission: Mission objectives, mission verification, selected results". In: *Solar System and its Exploration*. Ed. by W. R. Burke. Vol. 164. ESA Special Publication.

Prangé, R. et al. (Nov. 2004). "An interplanetary shock traced by planetary auroral storms from the Sun to Saturn". In: *Nature* 432, pp. 78–81. DOI: 10.1038/nature02986.

Press, W. H. et al. (2002). *Numerical Recipes: the Art of Scientific Computing*. 3rd. Cambridge: Cambridge University Press.

Priestley, M. B. (1988). *Non-linear and Non-stationary Time Series*. London: Academic Press.

Priestley, M. B. and T. Subba Rao (1969). "A Test for Non-Stationarity of Time-Series". In: *Journal of the Royal Statistical Society. Series B (Methodological)* 31.1, pp. 140–149. ISSN: 00359246.

Richardson, J. D. and K. I. Paularena (Jan. 2001). "Plasma and magnetic field correlations in the solar wind". In: *Journal of Geophysical Research* 106, pp. 239–252. DOI: 10.1029/2000JA000071.

Roberts, O. W., X. Li, and B. Li (May 2013). "Kinetic Plasma Turbulence in the Fast Solar Wind Measured by Cluster". In: *The Astrophysical Journal* 769, 58, p. 58. DOI: 10.1088/0004-637X/769/1/58. arXiv: 1303.5129 [astro-ph.SR].

Roberts, O. W. et al. (Dec. 2017). "Variability of the Magnetic Field Power Spectrum in the Solar Wind at Electron Scales". In: *The Astrophysical Journal* 850, 120, p. 120. DOI: 10.3847/1538-4357/aa93e5. arXiv: 1710.05089 [physics.plasm-ph].

Ruiz, M. E. et al. (Oct. 2014). "Characterization of the Turbulent Magnetic Integral Length in the Solar Wind: From 0.3 to 5 Astronomical Units". In: *Solar Physics* 289, pp. 3917–3933. DOI: 10.1007/s11207-014-0531-9. eprint: 1404.2826 (physics.space-ph).

Russell, C. T. (2001). "Solar wind and interplanetary magnetic field: A tutorial". In: *Washington DC American Geophysical Union Geophysical Monograph Series* 125, pp. 73–89. DOI: 10.1029/GM125p0073.

Russell, Christopher T. (1972). "Comments on the Measurement of Power Spectra of the Interplanetary Magnetic Field". In: *Solar Wind. Edited by Charles P. Sonett, Paul J. Coleman, and John M. Wilcox. Washington, Scientific and Technical Information Office, National Aeronautics and Space Administration., p.365*. Ed. by Charles P. Sonett, Paul Jerome Coleman, and John Marsh Wilcox. Vol. 308, p. 365.

Sahraoui, F. et al. (June 2009). "Evidence of a Cascade and Dissipation of Solar-Wind Turbulence at the Electron Gyroscale". In: *Physical Review Letters* 102.23, 231102, p. 231102. DOI: 10.1103/PhysRevLett.102.231102.

Sahraoui, F. et al. (Sept. 2010). "Three Dimensional Anisotropic k Spectra of Turbulence at Subproton Scales in the Solar Wind". In: *Physical Review Letters* 105.13, 131101, p. 131101. DOI: 10.1103/PhysRevLett.105.131101.

Sahraoui, F. et al. (Nov. 2013). "Scaling of the Electron Dissipation Range of Solar Wind Turbulence". In: *The Astrophysical Journal* 777, 15, p. 15. DOI: 10.1088/0004-637X/777/1/15. arXiv: 1303.7394 [astro-ph.SR].

Sakurai, T. (Feb. 2017). "Heating mechanisms of the solar corona". In: *Proceeding of the Japan Academy, Series B* 93, pp. 87–97. DOI: 10.2183/pjab.93.006.

Schekochihin, A. A. et al. (May 2009). "Astrophysical Gyrokinetics: Kinetic and Fluid Turbulent Cascades in Magnetized Weakly Collisional Plasmas". In: *The Astrophysical Journal Supplement* 182, pp. 310–377. DOI: 10.1088/0067-0049/182/1/310. arXiv: 0704.0044.

Schreiner, A. and J. Saur (Feb. 2017). "A Model for Dissipation of Solar Wind Magnetic Turbulence by Kinetic Alfvén Waves at Electron Scales: Comparison with Observations". In: *The Astrophysical Journal* 835, 133, p. 133. DOI: 10.3847/1538-4357/835/2/133. arXiv: 1701.00680 [astro-ph.SR].

Schwenn, R., H. Rosenbauer, and H. Miggenrieder (Oct. 1975). "The plasma experiment on board Helios /E 1/". In: *Raumfahrtforschung* 19, pp. 226–232.

Smith, C. W., B. J. Vasquez, and K. Hamilton (Sept. 2006). "Interplanetary magnetic fluctuation anisotropy in the inertial range". In: *Journal of Geophysical Research (Space Physics)* 111, A09111, A09111. DOI: 10.1029/2006JA011651.

Smith, C. W., B. J. Vasquez, and J. V. Hollweg (Jan. 2012). "Observational Constraints on the Role of Cyclotron Damping and Kinetic Alfvén Waves in the Solar Wind". In: *The Astrophysical Journal* 745, 8, p. 8. DOI: 10.1088/0004-637X/745/1/8.

Smith, C. W. et al. (July 2006). "Dependence of the Dissipation Range Spectrum of Interplanetary Magnetic Fluctuationson the Rate of Energy Cascade". In: *The Astrophysical Journal Letters* 645, pp. L85–L88. DOI: 10.1086/506151.

Spohn, T, Doris Breuer, and T V Johnson (2014). *Encyclopedia of the solar system*. 3rd ed. Amsterdam: Elsevier.

Stansby, D. et al. (Sept. 2016). "Experimental Determination of Whistler Wave Dispersion Relation in the Solar Wind". In: *The Astrophysical Journal Letters* 829, L16, p. L16. DOI: 10.3847/2041-8205/829/1/L16. arXiv: 1609.03039 [physics.space-ph].

Stansby, D. et al. (Nov. 2018). "A New Inner Heliosphere Proton Parameter Dataset from the Helios Mission". In: *Solar Physics* 293, 155, p. 155. DOI: 10.1007/s11207-018-1377-3. arXiv: 1807.04376 [astro-ph.SR].

Stenzel, R. L. (July 1999). "Whistler waves in space and laboratory plasmas". In: *SpaJournal of Geophysical Researchce Science Reviews* 104, pp. 14379–14396. DOI: 10.1029/1998JA900120.

Stverák, Å. t., P. M. Trávníček, and P. Hellinger (Oct. 2015). "Electron energetics in the expanding solar wind via Helios observations". In: *Journal of Geophysical Research (Space Physics)* 120, pp. 8177–8193. DOI: 10.1002/2015JA021368.

Taylor, G. I. (Feb. 1938). "The Spectrum of Turbulence". In: *Proceedings of the Royal Society of London Series A* 164, pp. 476–490. DOI: 10.1098/rspa.1938.0032.

Theiler, J. et al. (Sept. 1992). "Testing for nonlinearity in time series: the method of surrogate data". In: *Physica D* 58, pp. 77–94. DOI: 10.1016/0167-2789(92)90102-S.

Tong, Y. et al. (June 2019a). "Statistical Study of Whistler Waves in the Solar Wind at 1 au". In: *The Astrophysical Journal* 878, 41, p. 41. DOI: 10.3847/1538-4357/ab1f05. arXiv: 1905.08958 [physics.space-ph].

Tong, Y. et al. (Jan. 2019b). "Whistler Wave Generation by Halo Electrons in the Solar Wind". In: *The Astrophysical Journal Letters* 870, L6, p. L6. DOI: 10.3847/2041-8213/aaf734.

Treumann, R. A., W. Baumjohann, and Y. Narita (2019). "On the applicability of Taylor's hypothesis in streaming magnetohydrodynamic turbulence". In: *Earth, Planets and Space* 71.1, p. 41. DOI: 10.1186/s40623-019-1021-y.

Tu, C.-Y. and E. Marsch (July 1995a). "MHD structures, waves and turbulence in the solar wind: Observations and theories". In: *Space Science Reviews* 73, pp. 1–210. DOI: 10.1007/BF00748891.

Tu, C.-Y. and E. Marsch (July 1995b). "MHD structures, waves and turbulence in the solar wind: Observations and theories". In: *Space Science Reviews* 73, pp. 1–210. DOI: 10.1007/BF00748891.

— (Apr. 1997). "Two-Fluid Model for Heating of the Solar Corona and Acceleration of the Solar Wind by High-Frequency Alfven Waves". In: *Solar Physics* 171, pp. 363–391. DOI: 10.1023/A:1004968327196.

Štverák, Š. et al. (May 2009). "Radial evolution of nonthermal electron populations in the low-latitude solar wind: Helios, Cluster, and Ulysses Observations". In: *Journal of Geophysical Research (Space Physics)* 114, A05104, A05104. DOI: 10.1029/2008JA013883.

Vasko, I. Y. et al. (Feb. 2019). "Whistler Fan Instability Driven by Strahl Electrons in the Solar Wind". In: *The Astrophysical Journal Letters* 871, L29, p. L29. DOI: 10.3847/2041-8213/ab01bd.

Velli, M. et al. (Apr. 2015). "Models of coronal heating, turbulence and fast reconnection". In: *Philosophical Transactions of the Royal Society of London Series A* 373, pp. 20140262–20140262. DOI: 10.1098/rsta.2014.0262.

Veltri, P. and G. Zimbardo (Aug. 1993). "Electron-whistler interaction at the Earth's bow shock: 2. Electron pitch angle diffusion". In: *SpaJournal of Geophysical Researchce Science Reviews* 98, pp. 13335–13346. DOI: 10.1029/93JA01144.

Verscharen, D., K. G. Klein, and B. A. Maruca (Feb. 2019). "The multi-scale nature of the solar wind". In: *arXiv e-prints*. arXiv: 1902.03448 [physics.space-ph].

Vocks, C. (Nov. 2012). "Kinetic Models for Whistler Wave Scattering of Electrons in the Solar Corona and Wind". In: 172, pp. 303–314. DOI: 10.1007/s11214-011-9749-0.

Vocks, C. and G. Mann (Aug. 2003). "Generation of Suprathermal Electrons by Resonant Wave-Particle Interaction in the Solar Corona and Wind". In: 593, pp. 1134–1145. DOI: 10.1086/376682.

Vocks, C. et al. (July 2005). "Electron Halo and Strahl Formation in the Solar Wind by Resonant Interaction with Whistler Waves". In: 627, pp. 540–549. DOI: 10.1086/430119.

Weygand, J. M. et al. (July 2013). "Magnetic correlation functions in the slow and fast solar wind in the Eulerian reference frame". In: *Journal of Geophysical Research (Space Physics)* 118, pp. 3995–4004. DOI: 10.1002/jgra.50398.

Wicks, R. T., M. J. Owens, and T. S. Horbury (Mar. 2010). "The Variation of Solar Wind Correlation Lengths Over Three Solar Cycles". In: *Solar Physics* 262, pp. 191–198. DOI: 10.1007/s11207-010-9509-4. eprint: 1002.2319 (physics.space-ph).

Wicks, R. T. et al. (Sept. 2010). "Power and spectral index anisotropy of the entire inertial range of turbulence in the fast solar wind". In: *Monthly Notices of the Royal Astronomical Society* 407, pp. L31–L35. DOI: 10.1111/j.1745-3933.2010.00898.x. arXiv: 1002.2096 [physics.space-ph].

Wicks, R. T. et al. (Jan. 2013). "Alignment and Scaling of Large-Scale Fluctuations in the Solar Wind". In: *Physical Review Letters* 110.2, 025003, p. 025003. DOI: 10.1103/PhysRevLett.110.025003. eprint: 1209.5362 (physics.space-ph).

Wilson, L. B. et al. (Jan. 2013). "Electromagnetic waves and electron anisotropies downstream of supercritical interplanetary shocks". In: *Journal of Geophysical Research (Space Physics)* 118, pp. 5–16. DOI: 10.1029/2012JA018167. arXiv: 1207.6429 [physics.space-ph].

Woodham, L. D. et al. (Mar. 2018). "The Role of Proton Cyclotron Resonance as a Dissipation Mechanism in Solar Wind Turbulence: A Statistical Study at Ion-kinetic

Scales". In: 856, 49, p. 49. DOI: 10.3847/1538-4357/aab03d. arXiv: 1801.07344 [physics.space-ph].

Zhang, Y., H. Matsumoto, and H. Kojima (Sept. 1998). "Bursts of whistler mode waves in the upstream of the bow shock: Geotail observations". In: *SpaJournal of Geophysical Researchce Science Reviews* 103, pp. 20529–20540. DOI: 10.1029/98JA01371.

Zhou, Y., W. H. Matthaeus, and P. Dmitruk (Dec. 2004). "Colloquium: Magnetohydrodynamic turbulence and time scales in astrophysical and space plasmas". In: *Reviews of Modern Physics* 76, pp. 1015–1035. DOI: 10.1103/RevModPhys.76.1015.

Zweibel, E. G. and M. Yamada (Sept. 2009). "Magnetic Reconnection in Astrophysical and Laboratory Plasmas". In: 47, pp. 291–332. DOI: 10.1146/annurev-astro-082708-101726.

Vamsee Krishna Jagarlamudi

Turbulence du vent solaire de 0.3 à 1 UA : Observations de HELIOS et de WIND

Résumé :

Un des enjeux majeurs dans l'étude du vent solaire est la compréhension de l'évolution de la turbulence entre échelles spatiales mais aussi radialement, lorsqu'on s'éloigne du Soleil. Nous abordons ces questions en nous servant des observations de champ magnétique effectuées par les missions *WIND* et *HELIOS*. D'abord, à partir de longues séries temporelles de *WIND* nous identifions l'initiation de la cascade non linéaire dans le vent solaire lent. De la quasi-invariance du rapport entre le temps non linéaire et le temps d'Alfvén, nous déduisons que l'évolution comparable de la turbulence observée dans les vents lents et rapides peut s'expliquer par la constance du rapport $\frac{\langle B \rangle}{\delta B}$.
Ensuite, nous montrons comment une seule expression paramétrique permet décrire la densité spectrale de puissance aux échelles cinétiques à en tout lieu de l'héliosphère interne (entre 0,3 et 1 UA). Nous révélons également la présence dans l'héliosphère interne d'ondes de sifflement quasi-monochromatiques et montrons comment le vent lent offre les conditions nécessaires pour la présence préférentielle de ces ondes via le mécanisme d'anisotropie du halo.
Enfin, nous montrons comment la non-stationnarité est inhérente à la turbulence du vent solaire dans le régime inertiel. Ceci remet en question l'utilisation fréquente de la fonction d'autocorrélation comme outil pour estimer les échelles caractéristiques.

Mots clés : Vent solaire, Plasma, Héliosphère intérieure, Turbulences, Stationnarité, Ondes de sifflement, Analyse de données

Solar wind turbulence studies from 0.3 to 1 AU : HELIOS and WIND observations

Abstract

One of the key issues in solar wind studies is the understanding of the evolution of turbulence, both across spatial scales, and radially, when moving away from the Sun. We use magnetic field observations from the *WIND* and *HELIOS* missions to address this issue.
First, using long records from *WIND* we identify the initiation of the non-linear turbulent cascade in the slow solar wind. From the quasi-invariance of the ratio between non-linear time and Alfvén time we conclude that the similar evolution of turbulence in fast and slow winds is primarily governed by the constant $\frac{\langle B \rangle}{\delta B}$ ratio.
Second, we show how one single parametric expression can describe the power spectral density at kinetic scales at all positions in the inner heliosphere (between 0.3 and 1 AU). We also reveal the presence of narrow-band whistler waves in the inner heliosphere and using the halo anisotropy values show how the slow wind provides the proper conditions for the prevalence of whistlers.
Finally, we reveal how non-stationarity is inherent to solar wind turbulence in the inertial range, which questions the use of autocorrelation functions to estimate characteristic scales.

Keywords : Solar wind, Plasma, Inner-Heliosphere, Turbulence, Stationarity, Whistler waves, Data Analysis

Laboratoire de Physique et de Chimie de l'Environnement et de l'Espace (LPC2E),
3A, Avenue de la Recherche Scientifique,
45071, Orléans, Cedex 02